UAB
Universitat Autònoma de Barcelona

A proof-of-concept in Blu-ray based nanoplasmonic platform for label-free detection of complement activation (sC5b-9) in Myasthenia Gravis

Maria Jose Ugarte Orozco

ADVERTIMENT. L'accés als continguts d'aquesta tesi queda condicionat a l'acceptació de les condicions d'ús establertes per la següent llicència Creative Commons: https://creativecommons.org/licenses/?lang=ca

ADVERTENCIA. El acceso a los contenidos de esta tesis queda condicionado a la aceptación de las condiciones de uso establecidas por la siguiente licencia Creative Commons: https://creativecommons.org/licenses/?lang=es

WARNING. The access to the contents of this doctoral thesis it is limited to the acceptance of the use conditions set by the following Creative Commons license: https://creativecommons.org/licenses/?lang=en

Universitat Autònoma de Barcelona

PhD program in Biotechnology

Diseño de Nanobiosensors y Aplicaciones

A proof-of-concept in Blu-ray based nanoplasmonic platform for label-free detection of complement activation (sC5b-9) in Myasthenia Gravis

Doctoral Thesis

By

Maria Jose Ugarte Orozco

Director Dr. Javier Ramón Azcón

Tutor Dr. Arben Merkoçi Hyka

2026

Universitat Autónoma de Catalunya

Ugarte, 2026

ACKNOWLEDGMENTS

Acercándose el final de esta etapa y después de todos estos años de trabajo y esfuerzo, quiero expresar mi más sincero agradecimiento a todas las personas que me acompañaron y apoyaron en este camino.

Quiero agradecer a mi director de tesis, el Dr. Javier Ramón Azcón, por darme la oportunidad de formar parte de su grupo de investigación, por su orientación y apoyo constante, y por confiar en mi crecimiento en este campo.

I would also like to thank all the supervisors, postdocs, and colleagues in the lab for their support, patience, and guidance. Without your help and collaboration, completing this Thesis would have been a much harder task. I would like to give thanks and my deepest gratitude to Dr. Mehdi Torabi Goodarzi for his knowledge, encouragement, and mentorship. His professional advice and insights truly helped me in many ways. I have learned so much from everyone in the lab, and for that, I will always be grateful. To my PhD buddies, thank you for making the lab a great and welcoming place to be.

Gracias también al Dr. Eduard Gallardo del Hospital de Sant Pau (Barcelona, España) por su colaboración, el apoyo brindado y por compartir con nosotros muestras clínicas fundamentales para este trabajo.

Quiero dar un agradecimiento especial a nuestra asombrosa Lab Manager, Natalia, que pronto se convirtió en una compañera invaluable, apoyo, confidente y sobre todo una gran amiga. Gracias por alegrar los días de laboratorio, por escucharme, hacerme reír y acompañarme en tantos momentos, aquí, en Galicia, y próximamente en New Jersey o en México.

Sobre todo, quiero agradecer a Armando por estar a mi lado en esta etapa tan importante, por ser un pilar en mi vida, brindarme apoyo, consejos y calma. Gracias por escucharme siempre, por esos momentos de “terapia” dentro y fuera del laboratorio, y por recordarme que nada es tan grave como a veces lo imagino. Gracias también por compartir conmigo tus conocimientos, tu tiempo y tu paciencia infinita, por acompañarme en mis días buenos y malos, y por hacer que cada reto se sintiera un poco más ligero a tu lado. Me emociona poder ver todo lo que lograrás.

También quiero agradecer a mis amigos de toda la vida: Valeria, quien me apoyo durante la escritura de esta tesis, Karla, Dee, Mau, Mon, Perla y a todos los demás que, a la distancia, siempre estuvieron presentes con consejos, apoyo y comprensión. Sus palabras y porras me devolvieron la motivación en muchos momentos. Gracias también por visitarme y traer siempre un pedacito de casa con ustedes.

Por supuesto, no olvido a mis amistades en Barcelona: Karla, Carla y Juanpi. Las salidas, el apoyo incondicional, las tardes de cerveza y vermut y esa pequeña familia que construimos lejos del hogar son invaluables.

A mi familia, gracias a mis hermanos por su confianza, apoyo y consejos, por acompañarme en los momentos difíciles y celebrar conmigo cada logro, grande o pequeño. A Caneli, mi perrita, que siempre extraño y que, con su cariño incondicional, fue un recordatorio constante de alegría y compañía incluso en la distancia.

Y, sobre todo, a mis padres, cuyo amor incondicional, esfuerzo y presencia han sido la base de todo lo que soy. Gracias por impulsarme a alcanzar mis metas, por su paciencia infinita y por enseñarme con su ejemplo el valor del trabajo, la perseverancia y la humildad. Ustedes me dieron la fuerza para continuar en los momentos más duros y la confianza para soñar más alto de lo que jamás imaginé. Todo lo que he logrado se los debo a ustedes, y les estaré eternamente agradecida. Esta tesis es también suya.

Este trabajo es parte de la actuación TED2021-130467B-C21, financiado por MCIN/AEI/10.13039/ 501100011033 y por la Unión Europea "NextGenerationEU"/PRTR.



ABSTRACT

Myasthenia Gravis (MG) is a rare but debilitating autoimmune neuromuscular disorder that disrupts nerve-muscle communication, leading to muscle weakness, fatigue, and in severe cases, respiratory compromise. The pathogenic hallmark of MG is the presence of autoantibodies (Abs) in the neuromuscular junction (NMJ). Particularly, acetylcholine receptor-positive MG (AChR+ MG), where autoantibodies bind to the acetylcholine receptor (AChR) at the NMJ. This binding not only blocks receptor function but also initiates the classical complement cascade, triggering the formation of the membrane attack complex (MAC, C5b-9), causing structural damage, receptor depletion, and progressive synaptic dysfunction.

In recent years, complement-targeted therapies have emerged in MG management, such as Eculizumab and Ravulizumab, which target complement component C5 and inhibit the uncontrolled activation of the complement cascade. However, treatment response remains highly variable, and a proportion of patients experience limited efficacy, relapses, or treatment-related adverse effects. Current diagnostic tools do not provide direct insight into complement activation status, thereby limiting identifying patients that could benefit from it. Consequently, there is a pressing and unmet clinical need for reliable, real-time biomarkers of complement activity that can guide therapeutic stratification, optimize treatment selection, and advance precision medicine in MG.

This doctoral research addresses this gap through the development of a novel label-free plasmonic biosensor specifically designed to detect soluble C5b-9 (sC5b-9), in patient serum. The biosensor uses grating-coupled localized surface plasmon resonance (GC-LSPR) technology, from nanostructured polycarbonate (PC) substrates derived from commercial Blu-ray discs (BDs) and coated with thin gold layers. This cost-effective nanofabrication strategy provides an accessible and scalable platform for plasmonic sensing. The surface was biofunctionalized by a cys-Protein G-IgG antibody strategy, enabling oriented antibody immobilization, enhancing both sensitivity and surface stability. This approach overcomes common limitations associated with random antibody attachment, such as steric hindrance, decreased activity, and reduced reproducibility.

Analytical characterization demonstrated a limit of detection (LOD) of 0.015 ng/mL for sC5b-9, which is superior to the LOD reported for conventional ELISA assays.

The biosensor exhibited excellent reproducibility, stability, and specificity, and its performance was validated in serum samples from AChR+ MG patients at Hospital de Sant Pau (Barcelona, Spain). Importantly, the biosensor was able to differentiate between patients with AChR+ MG and MuSK, highlighting its potential clinical utility as a diagnostic tool.

Overall, this thesis contributes to the field of biomedical diagnostics by integrating advances in nanoplasmonic, surface chemistry, and biomarker detection to address a pressing clinical need. The development of this GC-LSPR biosensor demonstrates how innovative, cost-efficient, and extremely sensitive biosensing platforms can transition from proof-of-concept to clinically relevant applications. By providing a rapid and accurate means of assessing complement activation, the work presented here not only advances the understanding and management of MG but also exemplifies the potential of plasmonic biosensors to transform diagnostics and support the implementation of precision medicine in autoimmune disease management.

TABLE OF CONTENTS

Acknowledgments ..... **iii**

Abstract ..... **vi**

List Of abbreviations ..... **xiii**

Chapter 1 | Introduction **1**

1.1 Myasthenia Gravis (MG) and Complement Activation 1

1.1.1 Epidemiology and Clinical Features 1

1.1.2 Symptomatology 2

1.1.3 Immunopathogenesis of MG 3

1.1.4 Role of Complement System in MG 6

1.1.5 Structural and Functional NMJ Damage in MG 7

1.2 Detection and disease monitoring 9

1.2.1 Serology and antibody detection 9

1.2.2 Neurophysiology: RNS and SFEMG 11

1.2.3 Bedside tests 12

1.2.4 Need for Complement-Based Diagnostics 12

1.2.5 Emerging analytical platforms 12

1.2.6 Current Diagnostic Tools and Limitations 12

1.3 Overview of Biosensors 14

1.3.1 Key Components and Optical Biosensors 15

1.3.2 Analytical Parameters for Optical Biosensors 18

1.3.3 Applications in Biotechnology and Medicine 21

1.4 Plasmonic Biosensors and its Advantages 21

1.4.1 SPR, LSPR and SERS 21

1.4.2 Surface Plasmon Resonance (SPR) biosensor 24

1.4.3 Localized Surface Plasmon Resonance (LSPR) biosensor 28

1.4.4 Biorecognition layer 28

1.4.5 Cys-Protein G-Fc 32

1.4.6 Plasmonics in Blu-ray discs 32

1.4.7 Nanogratings based on Blu-ray discs 34

1.4.8 Integration with Microfluidics 35

Chapter 2 | Motivation and Objectives **37**

2.1 Motivation 37

2.2 Objectives 37
2.3 Specific Objectives 38
Chapter 3 | Materials and Methods 40
3.1 Development and characterization of nanoplasmonic chip 40
3.1.1 Introduction 40
3.2 Fabrication process of the chip 41
3.2.1 Chemical reagents and materials 41
3.2.2 Chip substrate generation 41
3.2.3 Protective layer removal 42
3.2.4 Gold thermal deposition 43
3.2.5 Scanning electron microscopy analysis 43
3.2.6 Microfluidic system 43
3.2.7 Optical Lid 46
3.2.8 Chip assembly 47
3.2.9 Sensing platform setup 48
3.2.10 Data Analysis 52
3.2.11 Bulk calibration 53
3.3 Sensor surface Biofunctionalization 54
3.3.1 Introduction 54
3.3.2 Biofunctionalization strategy 54
3.3.3 Materials and Methods for immobilization 55
3.3.4 Optimization (model IgG) 55
3.3.5 Standard biofunctionalization workflow 56
3.3.6 Time stability test 57
3.3.7 Matrix effect of serum and affinity validation 58
3.3.8 BRE affinity in complex matrix 58
3.4 Calibration and validation of the biosensor 59
3.4.1 Introduction 59
3.4.2 Materials and biological compounds 59
3.4.3 Calibration curve sC5b-9 in complex matrices 60
3.4.4 Clinical Validation with Real Samples 61
3.4.5 Data Analysis and Curve Fitting 61
3.4.6 ELISA of sC5b-9 62

Chapter 4 | Results and Discussion 64
4.1 Introduction 64
4.2 Design iterations 64
4.3 Protective layer removal optimization 66
4.4 Batch-to-batch reproducibility evaluation 76
4.5 Microfluidic system 78
4.6 Sensing platform setup 81
4.7 Bulk calibration 83
4.8 Noise analysis and limit of detection 85
4.9 Characterization of the sensor surface biofunctionalization 87
4.9.1 Biofunctionalization strategy 88
4.9.2 Anti-fouling technique 89
4.9.3 Time stability 92
4.9.4 Matrix effect in serum 93
4.9.5 Affinity validation of the BRE in a complex matrix 96
4.9.6 Calibration of the biosensor 97
4.10 Evaluation of biosensor for real patients MG+ serum samples 103
4.10.1 Serum samples 103
4.10.2 Data Analysis and Curve Fitting 104
4.11 Comparative study of ELISA and GC-LSPR biosensors 106
4.12 Comparative analysis 110
4.13 Clinical Relevance of Biosensor Performance Compared to ELISA 112
4.14 Limitations and future directions 112
Chapter 5 | Conclusions 115
Annex 118
List of publications 125
List of Tables 126
List of Figures 129
Bibliography 135

List Of abbreviations

Ab	Antibody
AChR	Acetylcholine receptor
BD	Blu-ray disk
BSA	Bovine serum albumin
CAD	Computer aided design
CD	Compact disk
DNA	Deoxyribonucleic acid
DVD	Digital versatile disk
EDC/NHS	N-ethyl-N-(3-(dimethylamino)propyl)carbodiimide / N-hydroxysuccinimide
EG	Ethylene glycol
ELISA	Enzyme-linked immunosorbent assay
FOM	Figure of merit
GC-LSPR	Grating-coupled localized surface plasmon resonance
IgG	Immunoglobulin G
IL	Interleukin
LOD	Limit of detection
LOQ	Limit of quantification
LSPR	Localized surface plasmon resonance
MAb	Monoclonal antibody
MES	2-Morpholinoethanesulfonic acid

MG	Myasthenia Gravis
MuSK	Muscle-specific kinase
NIR	Near infrared
NMJ	Neuromuscular junction
ODT	Octadecane thiol
OEG	Oligoethylene glycol
OoC	Organ-on-Chip
PAb	Polyclonal antibody
PBS	Phosphate buffer saline
PC	Polycarbonate
PEG	Polyethylene glycol
PIT	Photochemical immobilization technique
PLL	Poly(L-lysine)
PMMA	Poly(methyl methacrylate)
POC	Point-of-care
RI	Refractive index
RIU	Refractive index unit
RNS	Repetitive nerve stimulation
SAB	Sodium acetate buffer
SAM	Self-assembled monolayer
sC5b-9	Soluble terminal complement complex (C5b-9)

SFEMG	Single-fiber electromyography
SP	Surface plasmon
SPP	Surface plasmon polariton
SPR	Surface plasmon resonance
TIR	Total internal reflection
UV	Ultraviolet

CHAPTER 1 | INTRODUCTION

1.1 MYASTHENIA GRAVIS (MG) AND COMPLEMENT ACTIVATION

1.1.1 Epidemiology and Clinical Features

Myasthenia Gravis (MG) is a rare chronic autoimmune disease caused by pathogenic autoantibodies that target the postsynaptic antigens of the neuromuscular junction (NMJ), leading to skeletal muscle weakness and fatigue. MG is a heterogeneous disease that can present in at any age, and it occurs more frequently in women than in men (ratio 3:1).

Global epidemiological studies have shown that MG prevalence and incidence vary considerably worldwide. In 2024, Sciancalepore et al. performed a systematic review of 94 studies where they reported prevalence estimates worldwide ranging from 20 to 475 cases per million, incidence rates from 2.3 to 61.3 cases per million person-years, and a mean mortality of 1.4 cases per million person-years [1]. The following **Table 1** summarizes multi-study estimates and recent national findings to illustrate ranges and notable patterns.

Table 1. *Summary different systematic reviews statistics for estimated MG prevalence and incidence.*

Region or study	Prevalence (cases/100k)	Incidence (cases/100k-year)	Key notes	Reference
Systematic Review (94 studies, up to 2022)	17.33	1.57	AChR+ MG was the clinical subtype more frequent	[1]
Systematic review (64 studies, up to 2019), Spain	32.89	2.8	56,000-123,000 patients in Europe	[2]
Spain (2023)	10	1.5-2.1	Predominance of females in the early-onset forms	[3]
Germany (2023)	22.2	2.1	First study on MG prevalence and incidence in Germany	[4]

Portugal (2013)	11.17	0.63	Prevalence higher in males >65	[5]
United States (2021)	37	3.1	Higher estimates than older reports	[6]

In Spain, a 2023 review indicated prevalence values exceeding 100 cases per million person-years and incidence rates from 15 to 21 cases per million person-years [3]. Another comprehensive review by Bubuioc et al. (2021) confirmed the wide epidemiological variability, with global incidence rates ranging from 0.15 to 61.33 per million person-years and a Spanish incidence of 32.89 per million person-years [2].

Overall, the prevalence of MG has nearly doubled in the last two decades, a trend attributed to improved diagnostic techniques, more effective treatments, and increased patient longevity. The mortality rate of MG has dramatically declined from the early 20th century after the availability of acetylcholine esterase inhibitors, immunosuppressants, intravenous immunoglobulin, and advanced respiratory care [7].

1.1.2 Symptomatology

Symptoms can range from mild, localized weakness to severe, generalized muscle involvement, and often fluctuate in intensity throughout the day. The most common presenting symptoms are ocular. The clinical presentation is influenced by the specific autoantibodies involved and other patient factors [7].

Fatigable muscle weaknesses. The hallmark of MG is muscle weakness that worsens with activity and improves with rest. This weakness can affect the ocular, bulbar, limb, trunk, and respiratory muscles.

Ocular symptoms. Most patients initially present with ptosis (drooping eyelids) and diplopia (double vision). About 80% of those with ocular symptoms progress to generalized MG.

Respiratory involvement. Difficulty swallowing, speaking, and, in severe cases, problems with breathing can occur, especially during exacerbations or myasthenic crisis.

Fatigue. Beyond muscle fatigability, many patients experience central fatigue, a persistent sense of physical and mental exhaustion, which is highly prevalent and negatively impacts quality of life.

1.1.2.1 MGFA Clinical Classification

This classification is designed to identify the subgroups of patients with MG using the Myasthenia Gravis Foundation of America (MGFA) clinical classes (I-V) [8].

> *Class I*: Any ocular muscle weakness; may have eye closure, but other muscle strength is normal.

Class II: Mild weakness affecting muscles other than ocular; may also have ocular weakness. May affect limbs, axial muscles, respiratory, oropharyngeal or a combination of muscles of any severity.

Class III: Moderate weakness affecting other muscles other than the ocular.

Class IV: Severe weakness affecting muscles other than the ocular in varying severity.

Class V: Defined as intubation, with or without mechanical ventilation.

In general, these classifications use subjective assessments and lack quantification. Phenotypic descriptors: ocular vs generalized, early-onset (EOMG) vs late-onset (LOMG), thymoma-associated MG (TAMG), and serological subtype (AChR, MuSK, LRP4, seronegative), complement MGFA classification and help clinicians to inform prognosis and therapeutic strategy [9].

1.1.2.2 Myasthenic Crisis

The concept of Myasthenic crisis focuses on the clinical implication that can represent a serious, life-threatening, rapid worsening of MG like acute respiratory failure due to NMJ transmission failure or bulbar dysfunction that will require ICU-level monitoring, ventilatory support, and rapid antibody (Ab) removal, followed by optimization of immunotherapy [10].

1.1.2.3 Medications and factors that exacerbate MG

Many drugs have been proven to worsen or have an adverse effect on MG; these drugs include aminoglycosides, fluoroquinolones, class Ia antiarrhythmics, macrolides, magnesium salts, β-blockers, and non-depolarizing neuromuscular blockers. Drugs that impair neuromuscular transmission can block the nerve action potential or impair the release of Ach. Some of these drugs can cause MG-like symptoms, exacerbate or unmask MG. Medication review is integral for disease control and planning [11].

1.1.3 Immunopathogenesis of MG

1.1.3.1 Overview and cellular orchestration

Although MG is mediated by autoantibodies, different subtypes of T cells and their cytokines also play important roles in pathogenesis. The production of pathogenic autoantibodies clearly implicates B-cells and CD4+ T cells interaction. Upon antigen encounter, B-cells get activated, forming germinal centers and differentiating into plasma cells that produce autoantibodies [12].

The molecular immunopathology of MG is due to the presence of circulating autoantibodies specifically targeting the acetylcholine receptor (AChR), muscle-specific kinase (MuSK), or low-density lipoprotein receptor-related protein 4 (LRP4) (**Figure 1**). Patient-derived AChR, MuSK, and LRP4 autoantibodies in MG are demonstrably pathogenic [13]. Approximately 80-90% of patients have antibodies directed to the

AChRs, the remaining 10-20% have muscle-specific receptor tyrosine kinase (MuSK) or lipoprotein-related protein 4 (LRP4) or are seronegative [14].

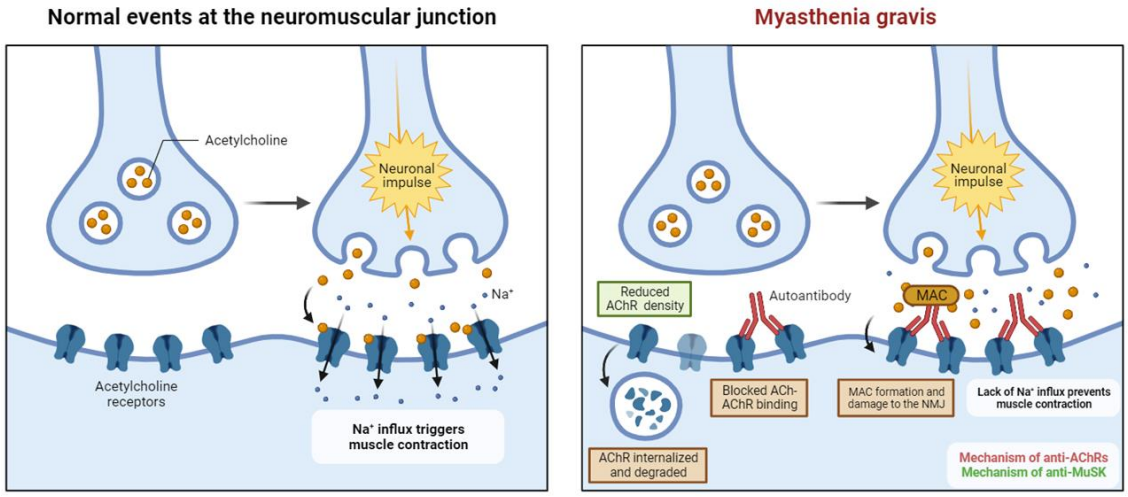


Figure 1. *Schematic overview of normal neural neuromuscular junction (NMJ) and immunopathogenesis of myasthenia gravis (MG).*

1.1.3.2 AChR autoantibodies

In the most generic form of AChR+ MG pathogenesis involves the depletion of postsynaptic membrane AChRs, compromising neuromuscular transmission [15,16]. MG autoantibodies are predominantly IgG1 and IgG3 subclasses that disrupt transmission through three primary mechanisms: (i) blocking of the AChR channel function, (ii) Cross-linking of AChRs leads to their internalization into muscle cells via endocytosis, followed by degradation of the receptors., and (iii) complement activation leading to the degradation of the neuromuscular junction through the production of membrane attack complex (MAC) [17]. IgG2 and IgG4 subclasses are also identified, but in fewer cases. The detection of serum AChR antibodies has been an invaluable tool in the diagnosis of MG.

1.1.3.3 MuSK Autoantibodies

MuSK, a receptor tyrosine kinase, is essential for agrin-LRP4-MuSK signaling that plays a key role in clustering AChR at the NMJ to promote efficient neuromuscular transmission [18]. In contrast to AChR+ MG, MuSK autoantibodies are predominantly IgG4, a subclass that undergoes Fab-arm exchange (a process whereby antibodies can dissociate to produce two identical half molecules each formed of a heavy chain and a light chain) and is functionally monovalent; these antibodies do not typically activate complement (due to their poor affinity for C1q and Fc receptors) or induce complement antigen internalization and instead act by disrupting LRP4-MuSK binding and downstream signaling, thereby impairing AChR clustering [13]. IgG1-3 MuSK antibodies can be present and may exert additional effects, but their overall contribution appears secondary to IgG4 in most patients [15].

1.1.3.4 LRP4 Autoantibodies

LRP4 is a transmembrane protein, containing several low-density lipoprotein domains, expressed in skeletal muscles and in motor neurons in the brain that bind agrin and activate MuSK. These antibodies are predominantly IgG1, and studies suggest that they are pathogenic, impairing agrin-dependent LRP4-MuSK interaction and AChR clustering. However, their contribution to complement-activation is still unclear [15].

1.1.3.5 Seronegative

Patients with a convincing clinical and electrophysiological phenotype of MG, but no detectable AChR or MuSK antibodies on conventional assays (RIPA/ELISA) are described as seronegative (SNMG). Clinical features vary across cohorts and ethnicities, reflecting methodological differences and true regional heterogeneity. Two non-exclusive explanations account for seronegativity: (i) pathogenic antibodies below the detection threshold of solution-phase assays, and/or (ii) antibodies to additional NMJ targets (including LRP4) later revealed by more sensitive platforms.

Clustered AChR cell-based assays (CBAs) identify AChR antibodies in a substantial fraction of patients previously negative by RIPA/ELISA, establishing that low-affinity, junction-restricted AChR antibodies are missed by conventional methods [17,19]. The discovery of LRP4 antibodies in double-seronegative MG further illustrates assay and antigen-dependence of serum; LRP4 antibodies are detected in a minority subset and are functionally pathogenic in experimental systems [20,21].

Clinically, evidence gaps persist: SNMG patients are under-represented in trials and optimal treatment paradigms remain less certain than for seropositive MG. Wider implementation of sensitive CBAs (AChR, MuSK, LRP4) and standardized reporting should reduce misclassification, enable mechanism-aligned therapy, and improve inclusion in studies [22,23].

1.1.3.6 Early-onset MG and late-onset MG

For MG, the onset age is divided into early-onset (EOMG; <50 years) and late-onset (LOMG; >50 years) groups with distinct epidemiology, sex ratios, thymic pathology, and genetic architecture. EOMG shows a female predominance and frequent thymic follicular hyperplasia, whereas LOMG skews male and less often exhibits hyperplasia. Ocular onsets are common; a sizeable proportion progresses to generalized disease, commonly within the first 2 years, though progression rates vary with population and treatment [17,24].

1.1.3.7 Thymoma-associated MG

Thymoma represents a distinct clinicopathological subset. Approximately 10-20% of patients with MG present a thymoma, and around 20-50% of thymoma patients develop MG, reflecting the unique immunologic environment of these tumors. Thymoma-associated MG (TAMG) is most often AChR+ MG and lacks a strong sex bias. Chest

CT/MRI is therefore recommended in generalized MG to evaluate thymoma, and thymectomy is mandatory when thymoma is present [9,19].

Combined with the diversity of underlying autoantibodies, it highlights the complexity of MG pathogenesis and highlights the importance of accurate biomarker-driven diagnostics for guiding treatment strategies.

1.1.4 Role of Complement System in MG

1.1.4.1 Complement activation at the NMJ (AChR+ MG)

The complement system is the most complex of the immunological pathways in human biology. Composed of approximately 50 proteins and four activation pathways (classical, lectin, alternative, and extrinsic) [25]. Complement activation studies in MG show complement fixating autoantibodies and complement factors in the NMJ [26]. Native complements control the complement cascade to prevent damage to autologous cells. The complement cascade can be activated via classical, lectin or alternative pathway but in AChR+ MG the classical pathway is initiated by C1q binding on the Fc domain of anti-AChR Ab, triggering a proteolytic cascade that results in cleavage of C3 and C5 into their respective activation products (C3a, C3b, C5a, and C5b), the latter complex binds with C6, C7, C8 and multiple C9 molecules lead to the formation of the C5b-9 product (**Figure 2**) [16,26,27].

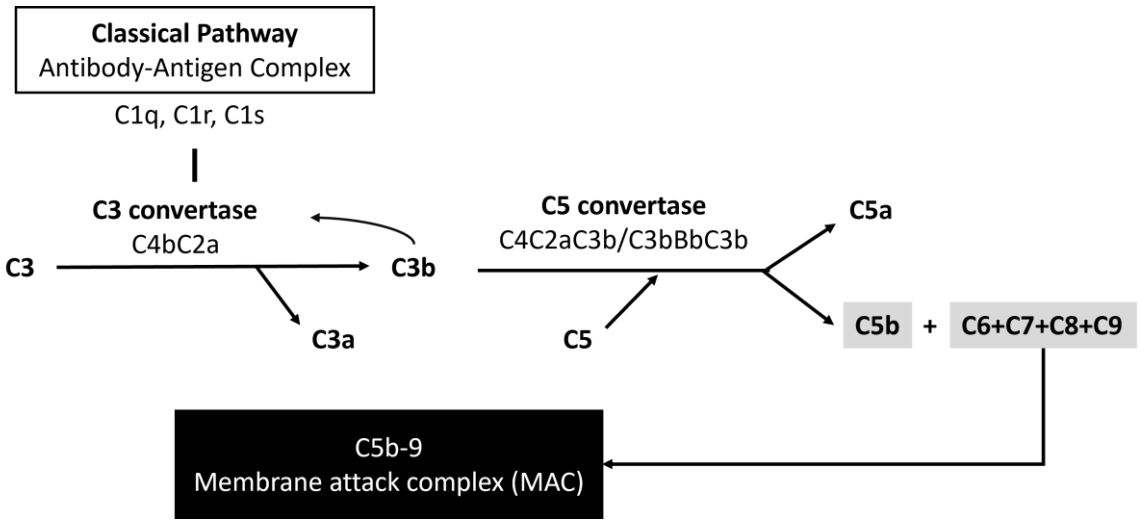


Figure 2*.Schematic representation of the complement cascade.*

1.1.4.2 Soluble vs membrane attack complex and regulation

C5b-9 may be inserted into lipid bilayers as the membrane attack complex (MAC) or remain soluble in plasma as soluble C5b-9 (sC5b-9). The MAC is a terminal effector of the innate immune system that assembles into a large β-barrel pore capable of perforating phospholipid membranes and thereby compromising cellular integrity and homeostasis [25]. Functionally, pore formation disrupts ionic gradients, triggers calcium influx, and

can culminate in cell lysis depending on the density of insertion and the target cell type [25].

The complement cascade can be activated via classical, lectin or alternative pathway but in AChR+ MG the classical pathway is initiated by C1q binding on the Fc domain of anti-AChR antibodies. This triggers a proteolytic cascade that cleaves C5 into C5a and C5b; the latter complex then binds with C6, C7, C8 and multiple C9 molecules lead to the formation of the C5b-9 product. This complex can either be inserted in the cell membrane as MAC, leading to physical degradation of the NMJ, or remain in the plasma as the soluble complement complex (sC5b-9) [26,28]. The relationship between circulating C9 concentration and sC5b-9 reflects the kinetics and regulation of terminal complement pathway activation. C9 is required for the polymerization and stabilization of the sC5b-9 complex, and its availability directly influences the extent of terminal complex formation. During active complement activation, increased generation of sC5b-9 is frequently associated with consumption of C9, resulting in decreased circulating C9 levels.

However, this relationship is not strictly proportional, as adequate C9 availability permits continued assembly of sC5b-9, whereas C9 depletion under sustained activation may become rate-limiting and restrict further sC5b-9 formation despite ongoing upstream complement activation. Thus, the interplay between C9 concentration and sC5b-9 levels reflects a dynamic equilibrium between complement consumption, component availability, and terminal pathway activity [29]. Because sC5b-9 accumulates during terminal pathway activation, its concentration in biological fluids serves as a dynamic biomarker of complement activation and has utility for disease monitoring and pharmacodynamic assessment [28].

In AChR+ MG, classical pathway initiation (via C1q binding to IgG1/IgG3 Fc) predominates; alternative pathway amplification may further enhance local C5b-9 generation at the neuromuscular junction. In MuSK-MG, where autoantibodies are predominantly IgG4, complement activation is typically absent, and pathology reflects signal-disruption rather than terminal pathway injury (see Section 1.1.2). For LRP4-MG, the extent of complement involvement appears variable across cohorts and experimental systems, suggesting heterogeneity in effector mechanisms within this subgroup.

1.1.5 Structural and Functional NMJ Damage in MG.

The NMJ is where the impulse transmission between nerve terminals and muscle fibers occurs. For this process, the release of presynaptic Ach is required and its subsequent binding to a AChR [7]. Complement-mediated attack at the NMJ in AChR+ MG causes both structural and functional impairment of synaptic transmission. Autoantibodies, predominantly IgG1 and IgG3, target the AChRs on the postsynaptic membrane and fix C1q, MAC causes focal membrane perforation and loss, simplification of junctional folds, and a marked reduction in AChR density. The effectiveness of NMJ transmission is also determined by the amount of ACh released by the nerve terminal, the density of AChR in the postsynaptic membrane, and the density of voltage-gated sodium channels at the

endplate. These structural injuries producing fatigable weakness are clinically characteristic of MG [7,24].

1.1.5.1 Structural endplate changes

Postsynaptic architecture is a principal target, and the most severe disruption is concentrated at AChR-rich crests of the folds.

AChR loss and fragmentation. Loss of AChR density and fragmentation of receptor clusters at the MG endplates are consistent findings in AChR+ MG [21].

Simplification of folds. The reduction of postsynaptic junctional folds and loss of the highly folded sarcolemma architecture results in diminished density of the voltage-gated sodium channels that trigger an action potential in the myofiber, which ultimately leads to a loss in contraction [7,21,30].

Endplate membrane damage. Complement and antibody-associated injury produces focal membrane loss, subsynaptic organelle damage, and in severe or prolonged disease an endplate myopathy with structural depletion that may only partially recover [30,31].

1.1.5.2 Functional transmission defects

MG disrupts the cascade of events for reliable muscle contraction. In addition, structural receptor loss and fold simplification produce predictable physiological consequences:

Reduced postsynaptic response. Loss of functional AChR lowers miniature endplate potential amplitude and it may follow below threshold during sustained or repetitive stimulation, producing failure of transmission and fatigability.

AChR functional blockade and turnover. Autoantibodies may directly block agonist binding and accelerate AChR internalization and degradation, further reducing functional receptor number and responsiveness [31].

Presynaptic compensation. Compensatory mechanisms can be triggered across disease subtypes [32]. In AChR+ MG, homeostatic plasticity increases vesicle release to partially offset postsynaptic loss, but this reserve is limited due to rapid vesicle depletion [30].

1.1.5.3 Progression and reversibility

Deficits often begin as functional (e.g., antibody-mediated blockade, increased turnover), then progress to fixed structural loss with sustained MAC activity [32]. The time course of recovery reflects this hierarchy:

Rapid functional improvements commonly follow plasmapheresis, IVIg or other therapies that remove or neutralize pathologic antibodies.

Structural repair unfolds more slowly (weeks-months) and may remain incomplete after severe or repetitive injury. Clinical efficacy of C5 inhibitors (e.g., eculizumab, ravulizumab; also, peptidic agents like zilucoplan) underscores the centrality of MAC to

progression and supports complement-activity biomarkers (e.g., sC5b-9) to monitor disease activity and therapeutic response [27].

1.2 DETECTION AND DISEASE MONITORING

MG remains diagnostically and therapeutically complex in the field of neuromuscular disorders. Clinical confirmation typically integrates serology, neurophysiology, bedside tests, and imaging [10]. Serological assays include radioimmunoprecipitation assays (RIPA), enzyme-linked immunosorbent assay (ELISA), and cell-based assays (CBA) [33]. Neurophysiological tests quantify transmission failure, such as repetitive nerve stimulation (RNS) and single fiber electromyography (SFEMG), with SFEMG offering the highest sensitivity but is limited by time, expertise, and is not suitable for frequent monitoring. Bedside tests (e.g., ice-pack test) and chest imaging complement the diagnosis but do not directly evaluate the immune mechanism [10].

Current tools often confirm the presence of MG or quantify transmission failure without identifying which pathogenic mechanisms predominate the disease in a patient (e.g., complement-mediated MAC vs. antigenic modulation vs. receptor blocking). Antibody titers show an inconsistent correlation with disease severity over time, further limiting their use as monitoring biomarkers. The sC5b-9 is widely used as a circulating marker of terminal pathway activation in complement-mediated diseases [34].

1.2.1 Serology and antibody detection

The confirmation of MG through antibody testing for AChR or muscle-specific receptor tyrosine kinase (MuSK) antibodies is a crucial step in diagnosis [27]. Currently, when MG is suspected anti-AChR is first measured and then anti-MuSK, and in the event of an assay yielding negative results in a patient suspected of MG, additional testing with higher precision is performed (**Figure 3**).

RIPA.

While still considered the gold standard for detection of anti-AChR antibodies, relies on radioactive isotopes (tagged with **I–α-bungarotoxin**), which requires the specialized labs, raising safety concerns and limiting their use in routine clinical laboratories due to stringent handling and disposal regulations [33]. Also, RIPA cannot detect complement activation and disease activity directly. Practical drawbacks include the use of radioactive isotopes, raising safety concerns, and limited scalability in routine clinical laboratories due to stringent handling and disposal regulations [33].

ELISA.

ELISA, while safer and more accessible, has demonstrated lower clinical sensitivity and inconsistent results in MG diagnostics, particularly for anti-AChR antibodies and struggles with quantifying low antibody titers [35], which are often clinically significant.

Cell-based Assay (CBA).

Improve sensitivity by using live or fixed cells expressing the native conformation of AChR or MuSK and can reclassify a fraction of SNMG as AChR+ MG; however, they are labor-intensive, non-standardized across laboratories, and subject to observer bias, which restricts their scalability and reproducibility in clinical practice [23].

All the mentioned methods rely on stable antigen-antibody interactions and maybe fail on fast dissociating and low affinity antibodies which can exist in seronegative MG cases. Pre-analytical and clinical factors (sample timing, immunotherapy exposure), assay cut-offs, and lab-to-lab differences influence results. If clinical suspicion is high and RIPA/ELISA is negative, performing a CBA (AChR, MuSK, LRP4) is highly recommended; atypical phenotypes or discordant results should prompt another review and electrophysiology [33,36,37].

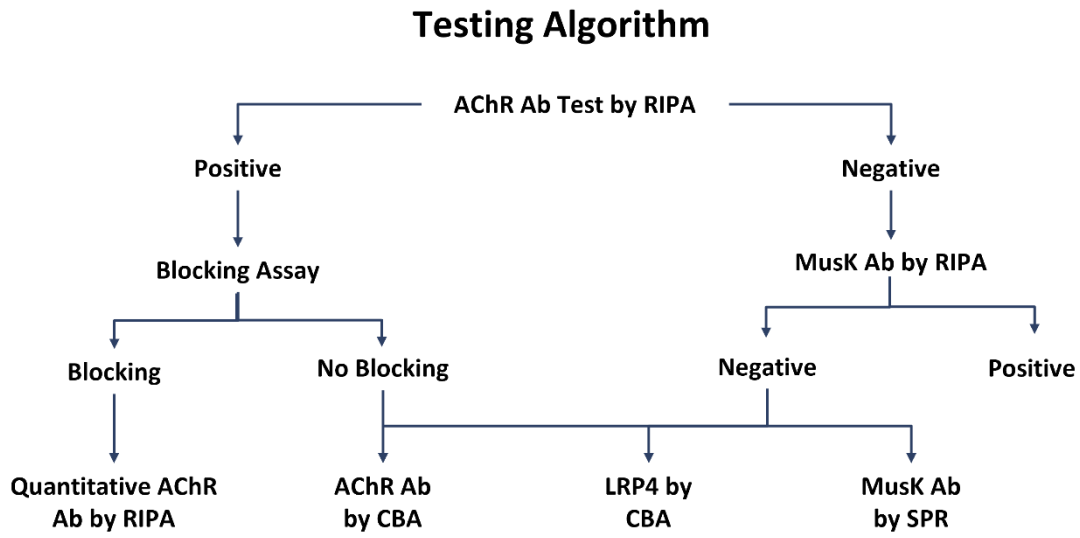


***Figure 3**. Testing algorithm for AChR antibody detection.*

According to reported values for required LOD and sensitivity in diagnosis of MG and evaluation of sC5b-9 level, Reference interval of 100-250 ng/mL using the ELISA technique is considered as normal level and elevated levels of sC5b-9 are associated to terminal complement pathway activation. Pathological levels can fall in 312-1000 ng/mL for Moderate complement activation and 760-1695 ng/mL for severe cases. Higher values of >4000 (up to >12,000) will be considered as fatal cases related to massive activation of the terminal complement pathway [38,39].

In this context, Surface Plasmon Resonance technology has emerged as a complimentary analysis approach which enables the optical, label-free, and real-time monitoring of biomolecular interactions. Also, it provides quantitative information on binding kinetics, including association and dissociation rates as well as equilibrium affinity.

This technology relies on the coherent oscillations of electrons (plasmons) at the interface between a metal and a dielectric layer under illumination of light with specific

angle of incidence and polarization. When biomolecules bind to a functionalized plasmonic surface, it causes the change in local refractive index, producing a measurable change in the resonance condition. This phenomenon allows determination biomolecule/receptor interaction but also quantitative kinetic parameters, including association and dissociation rates and equilibrium affinity constants. While currently SPR based technology is not a part of routine clinical diagnostics, its ability to provide a label-free, detailed kinetic and affinity data offers added value for research. It may contribute to improved diagnostic sensitivity and patient classification. Particularly, correlating antibody binding properties with pathogenic mechanisms, such as complement activation and formation of the Membrane Attack Complex, can enhance our understanding of disease heterogeneity.

Grating-Coupled SPR (GC-SPR) is one of the SPR configurations which instead of traditional prism-based configurations, a diffraction grating is used for coupling the light to surface plasmons. The grating enables efficient excitation of surface plasmons and offers advantages in terms of miniaturization, simplicity, cost, using polymeric substrates and compact optical setups. GC-SPR maintains the core capabilities of conventional SPR such as real-time, label-free detection, kinetic analysis, while improving versatility in sensor design, surface functionalization, and multiplexed monitoring of biomolecular interactions with nanomolar sensitivity without requiring amplification or extensive sample preparation [40,41].

1.2.1.1 Detection of soluble terminal complement complex (sC5b-9)

MAC-mediated postsynaptic injury is a central pathogenic mechanism in AChR+ MG where pathogenic IgG1/IgG3 subclasses efficiently activate the classical pathway. The main approaches to detect C5b-9 at the NMJ are tissue-based immunostaining (e.g., immunohistochemistry or immunofluorescence) on muscle biopsy and measurement in blood or serum. Tissue staining demonstrates focal MAC deposition at the postsynaptic membranes in AChR+ MG patients, while serum samples are measured by ELISA kits [24,25,42,43].

Detecting MAC or elevated sC5b-9 can support demonstration of complement-mediated pathology and inform therapeutic choices, but interpretation must account for timing, sampling, and treatment effects. It is important to note that complement activation (or sC5b-9 elevation) does not always correlate tightly with antibody titers or disease severity across cohorts, so biomarker data must be integrated with clinical and neurophysiology findings [24,43].

1.2.2 Neurophysiology: RNS and SFEMG

Electrophysiological studies that evaluate NMJ specifically include repetitive nerve stimulation (RNS) and single fiber electromyography (SFEMG). These specific tests can confirm the diagnosis of MG and pinpoint which element, or elements, of signal transmission is impaired as patients with symptoms, signs, and physical examination findings suggestive of a neuromuscular disorder are candidates for RNS and SFEMG testing [44,45].

Repetitive nerve stimulation (RNS). Electrodiagnostic technique that is specific for MG transmission failure, by repeated stimulating the target muscle at a slow (2 to 5 Hz) or fast (15 to 30 Hz) rate measures the resulting compound muscle action potential (CMAP) amplitudes. Although it is less sensitive than SFEMG and depends on muscle selection and disease distribution [44].

Single-fiber EMG (SFEMG). Utilizes a specialized electrode to selectively isolate and record the action potentials of a single muscle fiber, capable of detecting the difference or "jitters" in action potential. Therefore, it is the most sensitive neurophysiological test for MG diagnosis [44].

1.2.3 Bedside tests

As their name implies, these tests can be performed at the bedside. In neuromuscular examinations, the initial step in suspected MG cases, followed by laboratory diagnostic testing to confirm the clinical suspicion [45,46].

Ice-pack test. Is a simple, non-invasive diagnostic test that involves placing an ice cube across the eyelids for 2-5 min followed by the examiner's assessment for improvement in ptosis. It provides a rapid, low-cost diagnostic with sensitivity around 86-92% and specificity of approximately 79% in ocular phenotypes. False positives/negatives can occur, and it does not obviate further serological and neurophysiological testing [45].

1.2.4 Need for Complement-Based Diagnostics

Preclinical models and clinical studies have established the efficacy of complement inhibition in reducing disease severity, as shown by therapeutic agents such as Eculizumab and Zilucoplan, which target C5 cleavage and consequently prevent MAC formation [47]. However, not all patients benefit equally from these therapies, likely due to inter-individual variability in complement activation levels or the contribution of complement-independent mechanisms such as AChR antigenic modulation and direct receptor blockade [47]. To address this heterogeneity, recent research has focused on identifying biomarkers indicative of complement activity in AChR+ MG patients.

1.2.5 Emerging analytical platforms

Label-free plasmonic biosensing (SPR/GC-LSPR) offers real-time, label-free detection in complex biofluids with high analytical sensitivity, enabling rapid quantitation of relevant proteins/complexes and facilitating serial monitoring [40]. Clinical reviews highlight growing use of SPR-class technologies in diagnostics; remaining challenges include standardization and matrix effects.

1.2.6 Current Diagnostic Tools and Limitations

MG is multifaceted; diagnosis and monitoring still rely on clinical, serological, neuropsychological, and bedside tests. While antibody assessment and SFEMG are key to confirming the diagnosis, there are limitations in sensitivity, specificity, and

accessibility. New diagnostic tools are being developed but require extensive validation and broader implementation. **Table 2** summarizes and compares these diagnostic tools.

Table 2. *Comparison between MG diagnostic methods and some of their advantages and limitations.*

	RIPA	**ELISA**	**CBA**	**SPR**
Advantage	High specificity and sensitivity Estimation of accurate level of antibodies Commerciall y available	Complementar y for RIPA Estimation of accurate level of antibodies High throughput Affordable cost Non-radioactive	High specificity and sensitivity Non-radioactive More sensitivity Better mimicking of in-vivo models	High specificity and sensitivity Affordable cost Non-radioactive
Disadvantag e	Expensive Radioactive Isotopes	Less adapted for clinical usage moderate performance in comparison with RIPA	Needs specialized equipment High complexity Low throughput Not commercialize d	Non-commercial specific kits Higher technical complexity Lower throughput
Sensitivity	High	Moderate-High	Very High	Remarkabl y high
Limit of Detection	~0.02–0.05 nmol/L	~pM range	No fixed LOD (cell-based)	~pM–sub-pM (platform-dependent)

Developing a rapid quantitative assay that could bridge the gap to enable stratification of AChR+ MG patients who are most likely to benefit from complement blockage is highly desired. These considerations motivate the biosensing strategy developed in this thesis.

1.3 Overview of Biosensors

This section describes biosensors and key concepts in biosensing based on optical techniques such as Surface Plasmon Resonance (SPR) or Localized Surface Plasmon Resonance (LSPR) and its role in biotechnology, including drug discovery and targeting. According to the International Union of Pure and Applied Chemistry (IUPAC) a biosensor is "a device that uses precise biochemical reactions arbitrated by the immune system, isolated enzymes, or tissues for the detection of chemical compounds through optical, thermal, or electric signals using a biological receptor" (Ramesh, et al. 2022) [48].

A biological receptor can be antibodies, proteins, enzymes or whole cells and a transducer that converts the biological interaction into measurable signal, depending on the nature of this signal biosensors can be classified as electrochemical, mechanical, or optical (**Figure 4**).

Biosensors are frequently used for their capability to conduct quick testing with elevated sensitivity and specificity for a variety of biological receptor elements to detect a wide range of analytes [49].

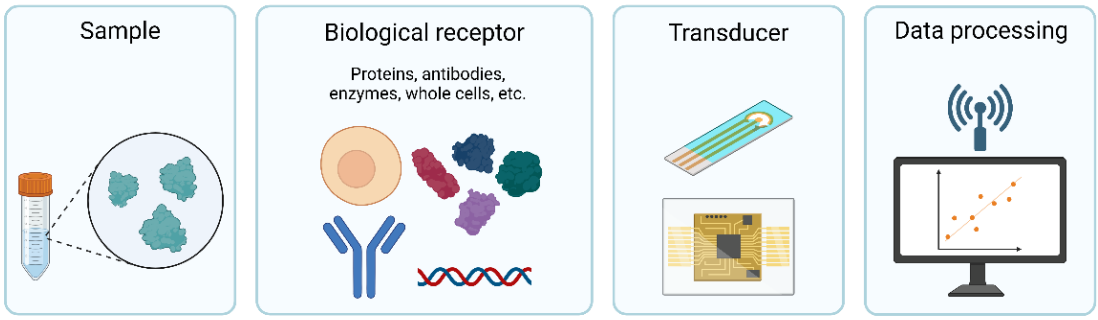


Figure 4.*Schematic representation of the basic components of a biosensor including the sample, the bioreceptor, the transducer, and the data processing for signal monitoring.*

Furthermore, they can be integrated into low cost, portable, and scalable POC platforms, increasing their potential as diagnostics tools. Biosensors are innovative analytical devices that bridge biological recognition with signal transduction to detect the presence or concentration of chemical and biological substances.

A widely recognized example is the glucose biosensor, routinely used by individuals with diabetes, to monitor their blood glucose levels. This device operates by detecting the interaction between glucose oxidase and glucose in a small blood sample, delivering results in under a minute.

Modern biosensors are applied across a wide spectrum of fields, including healthcare, environmental monitoring, industrial processing, food safety, and microbiology. Due to their high versatility, they serve critical functions such as detecting pollutants, identifying hazardous biological agents, and enabling early diagnosis of diseases [48].

1.3.1 Key Components and Optical Biosensors

The goal of a biosensor is generally to measure signal intensity and accuracy. From a structural perspective, all biosensors comprise essential components: an analyte, a bioreceptor, a transducer, electronic circuitry, and a display or readout interface. The design and integration of these components, especially the transducer and signal processors, often dictate the cost and performance of the biosensor.

1.3.1.1 Biorecognition Elements.

The biorecognition interface determines both the specificity and the analytical performance of a biosensor. It serves as the layer where the target is selectively captured, and the transducer monitors the molecular interaction. In practice, accuracy, reproducibility, and operational stability are as important on the selection of recognition elements as on the strategy used to immobilize it on the surface [49].

There is a wide range of biorecognition elements (BRE) available such as antibodies, enzymes, aptamers, nucleic acids (DNA/RNA probes), and synthetic binders like molecular imprinted polymers (MIPs) [50]. Selection of the BRE is driven by analyte class, affinity, matrix robustness (pH, ionic strength, temperature), batch-to-batch consistency, and availability. Antibodies and nucleic acids remain the most widely used for clinical targets; aptamers offer antibody-like affinities with chemical synthesis advantages but are not yet available for many biomarkers; MIPs can provide ruggedness and low cost for repeated use [51].

Biorecognition mechanisms are often grouped as catalytic vs affinity (**Figure 5**). Catalytic biosensors (typically enzyme-based) transform the analyte into a detectable product; they are mature and powerful, but the biocatalyst's activity/stability can be sensitive to environmental conditions (pH, temperature, denaturants) [52].

Affinity biosensors rely on non-covalent binding equilibria (e.g., antigen-antibody, complementary nucleic acids) measured as changes in mass, charge, refractive index (RI), or optical phase. In label-free plasmonic systems (SPR/LSPR), affinity binding is transduced in real time from refractive-index changes at the dielectric interface [53].

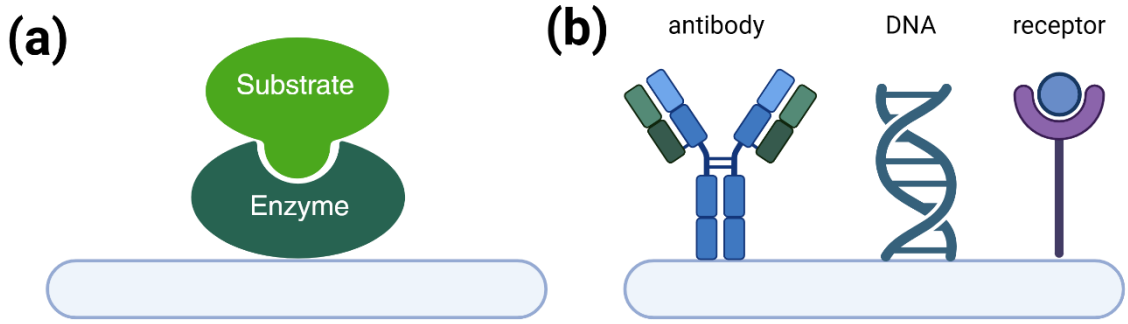


Figure 5*. Examples of biorecognition mechanisms. (a) catalytic biosensor (enzyme-based), (b) affinity biosensor (antibody, DNA, receptor).*

Together with the selection of the optimal biorecognition element, the surface biofunctionalization strategy is crucial to ensure maximum sensitivity, and reproducibility of the biosensor (See **Section 1.4.4**).

1.3.1.2 Transduction Mechanisms.

A biosensor couples a sensing element (the BRE) to a transduction element that converts the binding or reaction event into a measurable signal. Depending on the underlying physics, biosensor transducers are commonly classified as electrochemical, mechanical (mass-sensitive), or optical. Each class offers distinct advantages and practical constraints that shape analytical performance, integration, and point-of-care (POC) suitability [49], [50].

Electrochemical biosensors.

Measure the electrical changes (e.g., current, potential, or impedance) arising from analyte-receptor interactions at an electrode interface. Their strengths are high sensitivity, simple and low-cost instrumentation, and straightforward miniaturization capabilities. One of the most field-defining electrochemical biosensors is the oxygen/glucose quantification created in 1962 by Clark and Lyon [49]. However, electrochemical biosensors exhibit stability issues and are susceptible to interferences from the samples (e.g., proteins, peptides, microorganisms) [54].

Mechanical biosensors.

These biosensors rely on transducers that can detect biochemical interactions through the measurement of changes of mass on their surface. They can be classified in two families: (i) acoustic wave devices (e.g., quartz crystal microbalance, surface/acoustic wave resonators) that track resonance frequency shifts upon adsorption, and (ii) nanomechanical resonators (e.g., micro/nanocantilevers) that detect adsorption changes in resonance. These platforms provide label-free, direct mass readouts with excellent resolution, though performance can be sensitive to temperature conditions of the sample and often require tighter fluidic control than electrical/optical methods [55].

Optical biosensors.

The main principle for these transducers relies on the monitoring of the changes in light (e.g., intensity, phase, polarization, wavelength, or RI) caused by analyte-surface interaction. The most common optical sensors include fluorescence, absorption, luminescence, Raman spectroscopy, and RI-based techniques (i.e., SPR/LSPR) that are the most widely adopted for label-free, real-time analysis [40]. These sensors can be dived into label-based and label-free detection.

The label-based sensors require a reporter (e.g., chromophore, fluorophore, enzyme, or nanoparticle) to generate a colorimetric, fluorescent, or luminescent signal; while powerful, labels can alter binding affinity and add workflow complexity. Label-free transducers on the other hand monitor the interaction directly without the need for additional biomolecules, enabling real-time measurements with fewer steps, simplifying the process, and making it more cost-effective. Many of the most widely used label-free platforms exploit evanescent wave detection, including SPR/LSPR, waveguide, and interferometric sensors [40], [56].

Evanescent wave (EW) sensors use to their advantage the electromagnetic (EM) wave confinement in the dielectric or metal interface, resulting in localized or propagating electromagnetic modes. A fraction of the optical field penetrates only tens to a few hundred nanometers into the adjacent medium. This is known as the evanescent field, which serves as an extremely sensitive probe of local RI changes produced by analyte binding at the surface. This near-field confinement underlies the high surface sensitivity of SPR/LSPR biosensors and their real-time detection capabilities [57,58].

1.3.1.3 Sensitivity and Selectivity.

Sensitivity is related to the ability of the biosensor to detect changing concentrations of analytes with high intensity (e.g., slope of signal vs concentration), while selectivity is the ability to measure the target in the presence of potential interferents. For plasmonic (SPR/LSPR) sensors that measure the RI changes, common metrics include sensitivity (***S***) (e.g., $\Delta\lambda/\Delta n$ in nm/RIU), the full width at half maximum (FWHM), the figure of merit (FOM), and the limit of detection (LOD) [49,50,58].

Plasmonic sensors respond to RI changes withing the evanescent field and their sensitivity can be improved by: (i) nanostructure design, (ii) low-noise readout, and (iii) mass transport control. Selectivity is mostly influenced by the BRE and preserved at the biointerface.

Minimizing the false positives and nonspecific adsorption and maintaining affinity requires linker anchors (i.e., self-assembly monolayers), antifouling layers (i.e., PEG/OEG, zwitterionic materials, polymer brushes), and ligand immobilization (i.e., EDC/NHS, Protein A/G-Fc, streptavidin-biotin, His-tag) that keep the binding event within the near-field [59].

1.3.1.4 Point-of-Care (POC) Applications.

The latest POC biosensors aim to improve precision, accessibility, cost-effectiveness, and time consumption, as well as to achieve multiplexed analyte detection. They are designed for on-site patient care, enabling rapid and decentralized diagnostic testing, and are inexpensive enough [51].

Biosensors can generally be classified into electrochemical, mechanical, and optical types, depending on the physicochemical transformation that occurs upon analyte recognition from the bioreceptor [49].

Among these, optical biosensors have gained widespread attention due to their high sensitivity, rapid response time, real-time detection capabilities, and POC platforms. [60]. These sensors function by detecting alterations in the optical properties such as light intensity, wavelength, polarization, or phase, which come from the interaction between the optical field and the biorecognition elements on the sensor surface [61]. This principle enables detection methods, including adsorption, fluorescence, and refractive index-based techniques [60].

Particularly plasmonic biosensors offer several benefits such as high sensitivity and multiplexing capabilities. LSPR spectroscopy is gaining popularity due to its reasonable cost, high sensitivity, and label-free detection [62].

1.3.2 Analytical Parameters for Optical Biosensors

The performance of SPR and LSPR biosensors is determined not only by their capacity to detect variations in the RI at the interface, but by how reliably that change can be detected, quantified, and compared across instruments, assays, and matrices [58]. The variations can be monitored by interrogating the shift of the reflectivity dip in the spectrum. SPR sensors typically operate on either angle (θ) or wavelength (λ) interrogation, where the peak shift can be observed in response to RI changes. In LSPR, the shift is typically observed as a wavelength displacement (**Figure 6**).

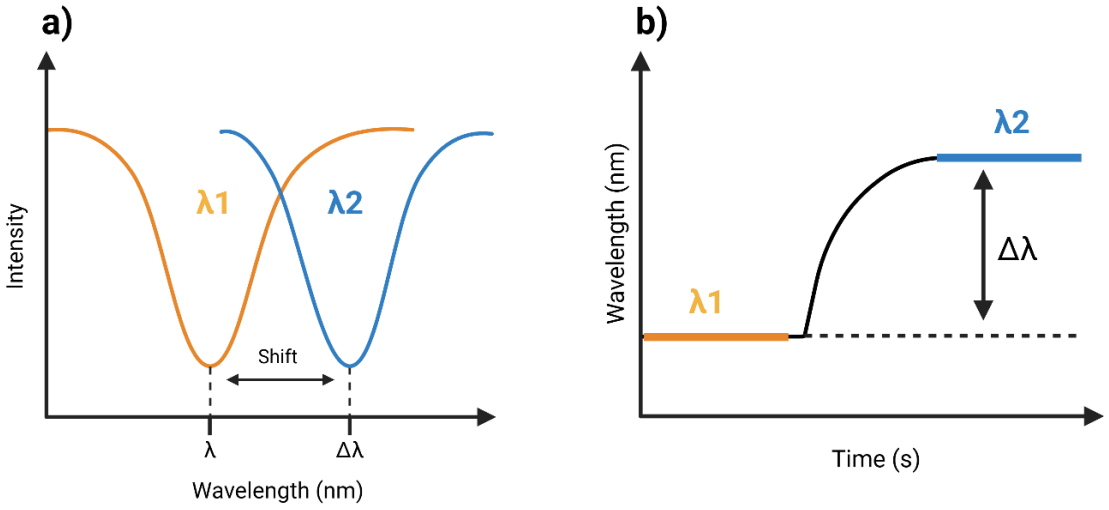


Figure 6. *Schematic representation of wavelength shift (Δλ, nm); (a) plasmon shift in surface plasmon resonance, (b) real-time sensogram of wavelength shift.*

Accordingly, this section consolidates the core metrics used throughout the manuscript and clarifies how they relate to study design and data interpretation in label-free plasmonic platforms.

Bulk sensitivity (S_B). The response to a uniform change in the refractive index near the interface. It reflects the physics of the optical mode and is useful for comparing sensing designs [58,61,63]. It can be calculated by this formula:

$$S_B = \frac{\Delta\lambda\ (nm)}{\Delta n\ (RIU)} \text{ or } S_\theta = \frac{\Delta\theta\ (deg)}{\Delta n\ (RIU)}$$

λ: resonance wavelength; n: refractive index; θ: angle

Surface sensitivity. The response to molecular adsorption within the sensor surface, ultimately reported as concentration units (e.g., analyte concentration ng/mL or molarity) obtained by calibration modeling. Surface sensitivity depends on decay length, biointerface design and mass transport, not just optical slope [63] (**Figure 7**).

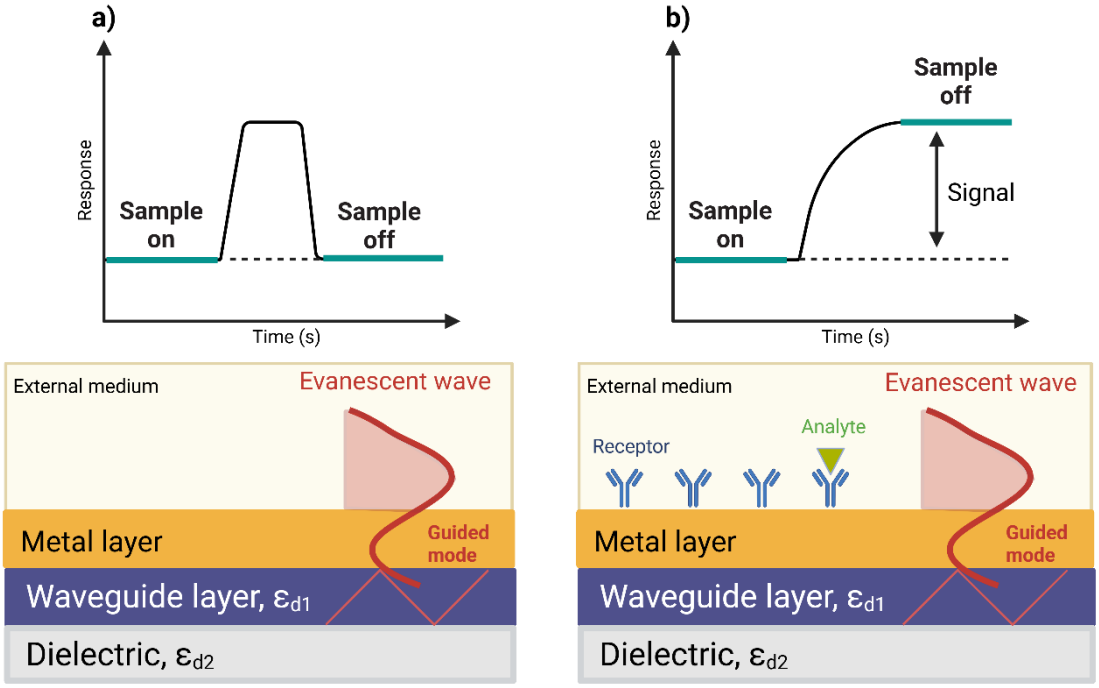


Figure 7. *Schematic representation of sensing principle for (a) bulk sensitivity and (b) surface sensitivity.*

Instrumental noise (σ_{blank}). The standard deviation of the measured output (i.e., wavelength, angle, or intensity) under blank or baseline conditions to account for spectrometer noise, intensity jitter, thermal drift, and other matrix-induced RI fluctuations [64,65].

Limit of detection (LOD) is considered the most reliable metric for comparing different transducer platforms. It can be derived through two approaches: either employing the bulk sensitivity *(S_B)*, or the surface sensitivity [61].

These parameters are critical, especially in clinical diagnostics and environmental monitoring, where detecting trace amounts of biomarkers or pollutants can be pivotal. In many advanced applications, biosensors are required to detect analytes in concentrations as low as nanograms per milliliter (ng/ml), emphasizing the importance of extremely sensitive and precise detection mechanisms.

These rigorous standards encourage further developments in biosensor materials, signal amplification methods, and the incorporation of nanotechnology to improve analytical efficiency and reliability [49].

There is extensive research in the field of GC-SPR biosensors, **Table 3** shows a comparison of sensitivity for some optical sensors.

Table 3. *Comparison of sensitivity in GC biosensors.*

Characteristics	**Grating period**	**Wavelength (nm)**	**Sensitivity**	**Ref.**
Au layer on BDs substrate	320 nm	525-750	425 nm/RIU	[66]
Al-Au bimetallic layer on gratings	350 nm	900	187.2º/RIU	[67]
Au layer on crossed relief gratings	550 nm	768-786	647.8 nm/RIU	[68]
Au layer on nanoimprinted nanograting	730 nm	990-1055	800 nm/RIU	[69]
BD-R based photolithography Ag layer	314 nm	700-715	319.96 nm/RIU	[70]
CD-R based photolithography Al layer	1470	850-910	1477.74 nm/RIU	[70]

1.3.3 Applications in Biotechnology and Medicine

Biosensors translate specific biological interactions into quantifiable signals and, when thoughtfully engineered, provide relevant measurements at clinical levels. In medicine, their value stems from the combination of label-free, real-time detection, small sample requirements, and miniaturization capabilities and eventually the creation of a point-of-care (POC) device.

Among optical platforms, plasmonic transducers (SPR/LSPR) have moved from research tools to credible clinical technologies due to improved surface chemistry, nanomaterial engineering, and microfluidic integration, enabling sensitive analysis in complex biofluids and multiplex formats.

In summary, the present work focuses on label-free LSPR detection of disease biomarkers, with an emphasis on complement activation products relevant to autoimmune neuromuscular disease. By combining near-field surface chemistries with oriented immunocapture and cost-effective nanostructured substrates, the platform aims to deliver the sensitivity, selectivity, and operational simplicity required for diagnostics [59].

1.4 PLASMONIC BIOSENSORS AND ITS ADVANTAGES

Plasmonic biosensing exploits the interaction of polarized light with a noble-metallic interface (typically Au or Ag) to excite collective electron oscillations that are extremely sensitive to refractive index (RI) and a dielectric medium (i.e., water or air). Because the resonance is dependent on the local dielectric environment, analyte binding within the evanescent field is converted into a measurable optical shift without need for labels, enabling real-time, kinetic, and quantitative assays with high surface sensitivity. Among optical sensors, plasmonic platforms such as propagating surface plasmon resonance (SPR), Localized SPR (LSPR), and surface-enhanced Raman scattering (SERS), offer complementary interaction volumes and readouts for a variety of applications [40].

1.4.1 SPR, LSPR and SERS

SPR arises when an EW propagates along a metal-dielectric interface and is characterized by the propagation constant and electromagnetic field distribution. When light interacts with the metal-dielectric surface under certain conditions (wavelength, polarization, angle of incidence, etc.), collective oscillations of free electrons are induced, known as surface plasmon polaritons (SPP), where fields decay exponentially away from the surface [71,72].

This evanescent field is the sensing probe: binding-induced RI changes and are read as shifts in angle, wavelength, phase, or intensity. In practice, SPPs are excited using total reflection in a prism (Kretschmann geometry), or via diffraction gratings, waveguides, and optical fibers; interrogation may be angular, spectral (wavelength), or intensity based, and SPR imaging (SPRi) uses the latter to visualize multiplexed arrays [73].

LSPR happens in metallic nanoparticles or nanostructured surfaces where plasmons are spatially confined. Compared with propagating SPR, LSPR offers tighter near-field

confinement (typically around 5-15 nm into the dielectric) and thus superior selectivity to nanoscale binding layers, excellent compatibility with compact optics, and tolerance to scattering media; by contrast, SPR depth is around 200-300 nm and typically achieves narrower resonances and higher figures of merit for bulk RI sensing.

Wavelength tunability in SPR is readily achieved by changing incidence angle, whereas LSPR tuning is accomplished via nanostructure size, shape, and parameters; the latter also modulate field enhancement and linewidth [58,74].

SERS leverages plasmonic near-fields to amplify Raman scattering. SERS thus complements refractometric SPR/LSPR: the former excels at chemical identification; the latter at label-free affinity quantity and kinetics. Hybrid devices and dual-mode gratings increasingly combine these capabilities on a single chip [58,72,75].

Overall, plasmonic transduction provides: (i) label-free, real-time monitoring of surface interactions, (ii) kinetic analysis (association/dissociation rates), (iii) compatibility with miniaturization and multiplexing, and (iv) robustness for complex matrices [40,59]. **Table 4** summarizes the comparison between sensing modalities.

Table 4*. Comparison of main plasmonic sensing modalities.*

Mode	Physical principle	Typical platform	Sensing volume	Strengths	Typical uses
SPR	Coupling of light to metallic surface (usually gold)	Prism (Kretschmann), waveguide, fiber	Hundreds of nm (evanescent tail)	High bulk RI sensitivity, well established instrumentation	Kinetics, affinity, clinical assays, label free quantitation
LSPR	Resonance of conduction electrons in nanogratings/nanostructures	Colloidal NPs, lithographic nanostructures, metasurfaces	Tens of nm (near-field)	Strong near-field, compact, tolerant to scattering, easy integration	Small volume assays, single particle sensing
SERS	Plasmonic field enhancement of Raman scattering	Nanogaps, nanoparticle aggregates	Sub nm to nm	Molecular specificity, potential single molecule detection	Chemical identification, ultrasensitive detection

1.4.1.1 Components and materials

Sensor performance depends on the metallic surface, nanostructure geometry, optical coupling, and bifunctionality strategies [75].

Metallic film and stability. The most employed metal film is gold (Au) due to its chemical stability, biocompatibility, and well-developed thiol-based self-assembled monolayer (SAM) chemistry for robust and oriented ligand immobilization. Silver (ag) affords sharper resonances but is prone to oxidation and sulfidation, complicating long-term use and biofunctionalization. For this reason, Au dominates in clinical systems [75].

Substrates and couplers. Prism-coupled SPR remains the benchmark for metrology and kinetic work, while grating-coupled (GC-SPR) and fiber-optic SPR (FO-SPR) eliminate the prism for compact, integrable devices. As expected from mode coupling, prism-based SPR often achieves the highest bulk sensitivity; GC formats trade some sensitivity for a smaller platform and can be engineered to recover exceptional performance [73].

Nanostructures. Nanoparticles, nanohole arrays, nanogratings, and metasurfaces tailor resonance energy, field localization, and spectral linewidth. LSPR performance is strongly influenced by geometry. These platforms enable multiplexing, single-particle sensing, and dual-mode operation with SERS when required [72].

Surface chemistry and biorecognition. Analytical performance in complex matrices is ultimately limited by the biointerface. Capture ligands must be presented within the responsive near field, in active orientation, and on backgrounds that suppress nonspecific adsorption over the full assay time.

On gold, immobilization can be performed directly as exemplified in **Figure 8a** (physisorption or chemisorption), indirectly via linkers as in **Figure 8b** (e.g., self-assembled monolayers, SAMs), within 3D matrices as in **Figure 8c** (e.g., polymer brushes, hydrogels) or through affinity handles **Figure 8d** (Protein A/G-Fc, streptavidin-biotin, His-tag) [73].

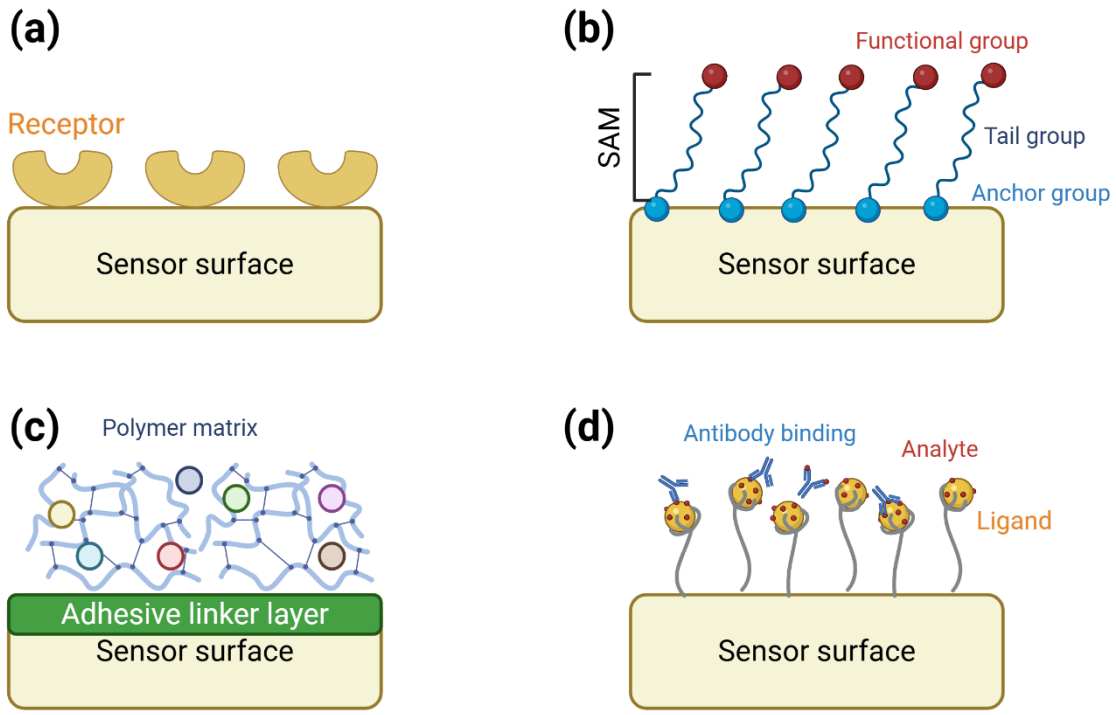


Figure 8. *Representation of the main types of biofunctionalization methods: (a) direct immobilization;(b) covalent binding to a self-assembled monolayer (SAM); (c) polymer matrix entrapment; (d) affinity immobilization through protein-antibody binding.*

Physical adsorption is experimentally simple, relying on electrostatic and hydrophobic interactions, but it often yields heterogeneous packing, partial denaturation, and poor reproducibility; limitations that are amplified in serum or plasma where competitive adsorption quickly reconfigures the surface [40].

Covalent chemisorption overcomes stability issues by coupling native side chains of the BRE to reactive groups, i.e., amine coupling (EDC/NHS) to carboxylates, maleimide-thiol addition to cysteines, aldehyde-amine, producing robust films suitable for regeneration. These methods provide a stable bioreceptor layer; however, it has issues with proper orientation and surface selectivity [48].

SAM based approach consists in the chemisorption on the gold surface of a single molecular layer, which is characterized by terminal reactive functional groups that can be tailored to selectively bind the desired bioreceptor. Commonly used molecules are alkanethiols, which can have different end functionalities (i.e., -COOH, -NH2, -OH, maleimides) [73]. This method allows the surface to cover uniformly, reducing non-specific adsorption [40].

Readout instrumentation. Bench-top SPR systems offer angle or wavelength interrogation with high precision, LSPR can be monitored via extinction/scattering with compact spectrometers or dark-field optics, and fiber-optic. Selection is dictated by the required limit of detection, kinetic fidelity, multiplexing, and design constraints [40,73].

1.4.2 Surface Plasmon Resonance (SPR) biosensor

SPR sensors are based on the EW sensing principle, which measures changes in the RI of the medium in the vicinity of the sensor surface. An EW is an electromagnetic field generated from propagating or resonating light wave at the interface of two media with different RI [63,76]. The propagation of light in EW sensors is due to total inter reflection (TIR) phenomenon, which is described by the Snell's Law:

$$n_1 \sin\theta_1 = n_2 \sin\theta_2$$

θ_1: angle of incidence; θ_2: angle of refraction; n_1 and n_2: RI of dielectric and metal, respectively.

With θ_2 becomes complex under TIR, it generates an evanescent field that can couple to a plasmon polariton (SPP). The propagation constant of a SPP at the metal-dielectric

interface is determined by the optical constants of the surrounding media, represented by the following formula:

$$\beta_{SPP} = \frac{w}{c}\sqrt{\frac{\epsilon M \epsilon D}{\epsilon M + \epsilon D}} = \frac{2\pi}{\lambda}\sqrt{\frac{\epsilon M \epsilon D}{\epsilon M + \epsilon D}}$$

ω: angular frequency; ***c***: speed of light in vacuum; λ: wavelength; ϵM and ϵD: permittivity of metal and dielectric.

Any perturbation in the local dielectric function near the surface (e.g., analyte binding) shifts β_{SPP} and consequently, the optical resonance. The SPP field decays exponentially away from the interface with asymmetric penetration into the metal and dielectric; only interactions within the penetration depth contribute measurably, consistent with the near-surface selectivity discussed earlier (**Section 1.4.1**) [77].

In propagating SPR, the sensing volume is set by the evanescent field of the SPP, whose penetration into the dielectric is strongly wavelength and material dependent. For SPP at the Au-dielectric interface, the penetration rate in the visible and near infrared regions (NIR) lies on the order of a few hundred nanometers (around 200-300 nm). Therefore, only biomolecular interactions happening within the evanescent field penetration depth can perturbate the SP and be detected [76]. Physically, adsorption of biomolecules increases the local refractive index (RI) at the functionalized surface, altering the effective permittivity experienced by the SPP, and therefore shifting the propagation constantly.

Because β_{SPP} exceeds the in-plane momentum of a freely incident photon, SPPs cannot be excited by direct illumination [77]. To achieve this, the light wave's vector that is parallel to the interface must match the propagation vector of the surface plasmons at the metal-dielectric interface:

$$k_x SPP = \frac{2\pi}{\lambda}\sqrt{\epsilon}\sin\theta = k_x light$$

In practice, this is implemented with prism couplers (Kretschmann or, less commonly, Otto), integrated waveguide sections, or surface gratings that supply the additional momentum needed for coupling (**Figure 9**).

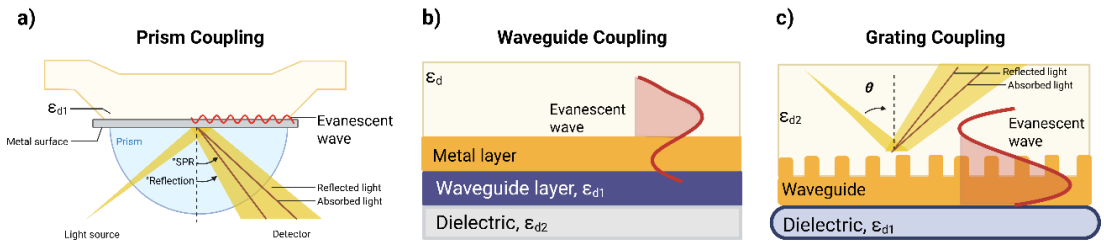


Figure 9. *Schematic representation of SPR coupling methods: (a) prism coupling; (b) grating coupling; (c) waveguide coupling.*

The prism-coupling method, also known as Kretschman configuration, is the most utilized technique in SPR sensing (**Figure 9a**). This method relies on attenuated total reflection (ATR), light passes through a high RI prism to reach the interface between the base of the prism and the thin plasmonic metal layer. At this interface, TIR occurs, generating EW that excites plasmonic resonance and propagates with a specific vector. The properties of the wave can be adjusted by controlling the angle of incidence, as well as the wavelength of light used to excite the surface plasmons [71,78]. A major drawback from this method is that prisms can be bulky, and miniaturization becomes difficult.

In waveguide coupling (**Figure 9b**), light is guided through an optical waveguide in the form of guided modes. When the guided light reaches the metal film layer, it evanescently penetrates through the metal, exciting SPP at the outer boundary [79,80]. This method offers advantages in terms of producing more compact systems and integration potential.

Another technique for exciting SPPs is by using grating couplers (GC-SPR/LSPR) (**Figure 9c**). Grating coupling is based on the diffraction of light, the light is directed onto a metal grating with a periodic structure that diffracts the incident beam into various diffraction orders, which can be either evanescent or propagating back into the dielectric [81]. Even though prism-based couplers offer higher sensing performance, grating coupling offer highly attractive features such as allowing for normal incidence excitation, which can simplify the optical setup and allows for more compact and miniaturized devices.

The main challenge is the design and production of the grating couplers. Different fabrication methods such as lithography-based (i.e., UV mask, electron beam, nanoimprint, etc.) approaches and DVD/CD/BD-based are the most common ones. In this regard, many straightforward methods have been developed, making this coupling easy and cost-effective.

The refractometric plasmonic sensing concept is based on the detection of the local RI changes that take place when a biomolecular reaction occurs that alters the plasmonic wavevector, by tracking the peak position during measurement, a sensogram can be obtained, providing a quantitative method and analyte binding kinetics [77,81].

In general, a plasmonic biosensor scheme typically consists of the following components: a broadband light source, a plasmonic transduce with the biomolecular recognition element immobilized on its surface, a detector, and a fluidic system (**Figure 10**).

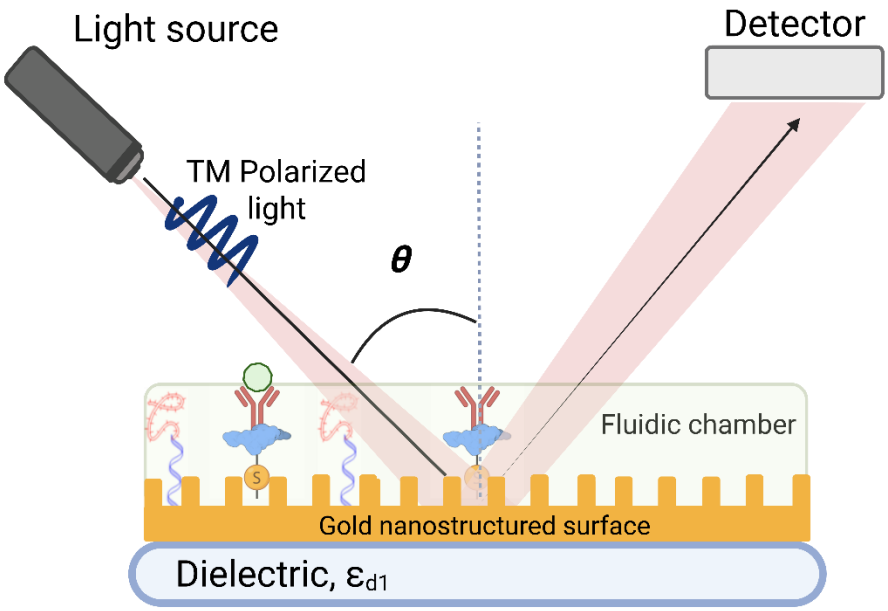


Figure 10. *Schematics representation of a GC-SPR biosensing configuration when TM polarized light is used.*

For SPR visualization and monitoring, the reflected light spectra are acquired. The plasmonic resonance is identified by a dip in the spectrum. This peak is identified by a specific angle or wavelength where the strongest interaction between light and surface plasmon occurs. The bandwidth of the SPR is relevant for determining the precision of a sensor and is often indicated by the full width at a half maximum (FWHM) value, (i.e., the width of the spectrum curve measured between points corresponding to half of the maximum amplitude). FWHM is influenced by factors like damping effects, metal film thickness, quality, and surface roughness [76].

By combining this parameter with sensitivity (S), a dimensionless parameter known as FOM is obtained, which can be used to quantify the overall performance of a sensor. FOM is expressed as:

$$FOM = \frac{S}{FWHM}$$

FOM correlates both the sensitivity and the FMWH and can be used to quantify the overall performance of a sensor. Finally, the LOD is the lowest RI change to be reliably distinguished from the baseline noise and can be expressed as:

$$LOD = 3.3\frac{\sigma}{S}$$

σ: standard deviation of the background noise;
S: sensitivity (the slope of the calibration curve)

This equation illustrates that as noise level increases, the LOD rises, reducing the system's sensitivity to low analyte concentrations [82].

1.4.3 Localized Surface Plasmon Resonance (LSPR) biosensor

When incident light drives the collective oscillation of free electrons confined in a metal nanoparticle or nanostructure; the oscillation reaches resonance for certain wavelengths, producing strong near-field enhancement and pronounced extinction peaks that depend on the size, shape, composition of the nanostructure (e.g., Au, Ag, bimetallic), and the dielectric environment, as well as interparticle coupling set by period and pitch. All these design parameters make LSPR highly tunable and because LSPR is directly excitable by light, unlike propagating SPPs that require momentum-matching schemes, it adds a lot of practical assay flexibility [83,84].

Within this framework, the choice of nanostructure and array design is determined with the biointerface (i.e., oriented immobilization, antifouling layers) to ensure that the nanoscale binding event remains within the responsive near field and that spectral narrowing strategies are effectively converted into lower limits of detection for clinically relevant biomarkers.

1.4.4 Biorecognition layer

The analytical performance of a plasmonic biosensor ultimately depends on how effectively the biorecognition layer translates target binding into a reproducible optical perturbation within the responsive near field. This requires a surface architecture that (i) presents receptors at high effective site density without steric crowding, (ii) orients binding sites toward analyte, and (iii) suppresses nonspecific adsorption across the full assay window and matrix conditions. Because the evanescent field decays within tens to a few hundred nanometers from the metal, receptors must be immobilized close to the surface while retaining native conformation and kinetics; in practice, the immobilization strategy must be chemically stable, regenerable (where needed), and batch-to-batch reproducible so that small refractive-index changes arising from binding events can be resolved against baseline drift and matrix noise.

Commonly used recognition elements include antibodies (proteins, peptides, small molecules), nucleic-acid probes (DNA/RNA), aptamers selected by SELEX, enzymes for catalytic formats, and increasingly, synthetic receptors such as molecularly imprinted polymers (MIPs); the choice is dictated by analyte class, expected concentration, sample matrix, and required regeneration chemistry [85].

The selection of the immunoassay format is fundamentally dictated by parameters such as target size, molecular weight, dynamic range, and matrix complexity. These core configurations are schematically detailed in **Figure 11**.

In a direct competitive immunoassay (**Figure 11a**), specific capture antibodies are immobilized directly onto the sensor surface, and the target analyte in the sample competes with an introduced competitor molecule for a limited number of active

antibody-binding sites. In an indirect competitive immunoassay (**Figure 11b**), the target analyte is pre-immobilized onto the substrate surface; free antibodies are then introduced, creating a competitive equilibrium.

For non-competitive layouts, the direct non-competitive format (**Figure 11c**) involves the straightforward, single-step binding of the target analyte to surface-tethered capture antibodies, generating a refractometric shift that is directly proportional to the bound mass. Finally, the indirect non-competitive format (**Figure 11d**), commonly known as a sandwich assay, utilizes an immobilized primary antibody to capture the target analyte, followed by the sequential introduction of a secondary antibody that targets a distinct, non-overlapping epitope on the same analyte. This secondary binding event significantly amplifies the local refractive index change within the evanescent field, making it an exceptionally powerful configuration for resolving ultra-low concentrations of biomarkers within highly complex clinical biofluids [41,86].

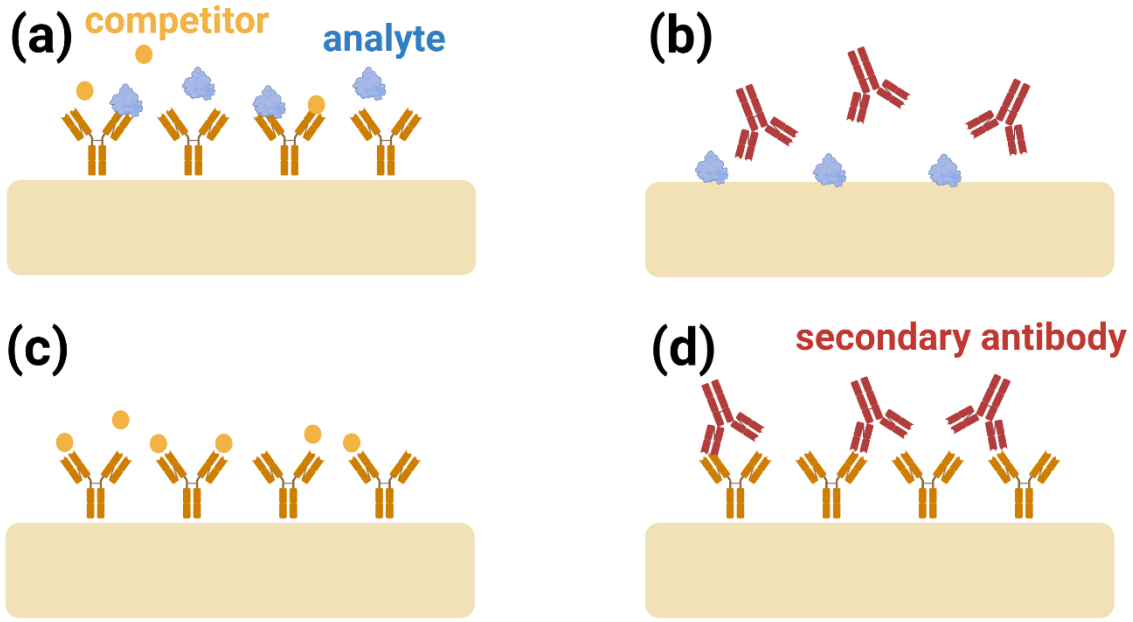


Figure 11. *Different immunoassay configurations: (a) direct competitive, (b) indirect competitive, (c) direct non-competitive, and (d) indirect non-competitive.*

For antibody-based layers, orientation is decisive. Full-length IgG molecules can adopt tail-on, head-on, side-on, or flat-on poses on a surface (**Figure 12**); tail-on (Fc-down) maximizes antigen access by exposing both Fabs. Protein A/G-Fc capture enforces this geometry and supports mild regeneration (acidic buffers) without stripping the capture layer; cysteine-engineered variants (e.g., cys-Protein G) form well-ordered monolayers on maleimide-terminated SAMs, improving mechanical robustness under flow.

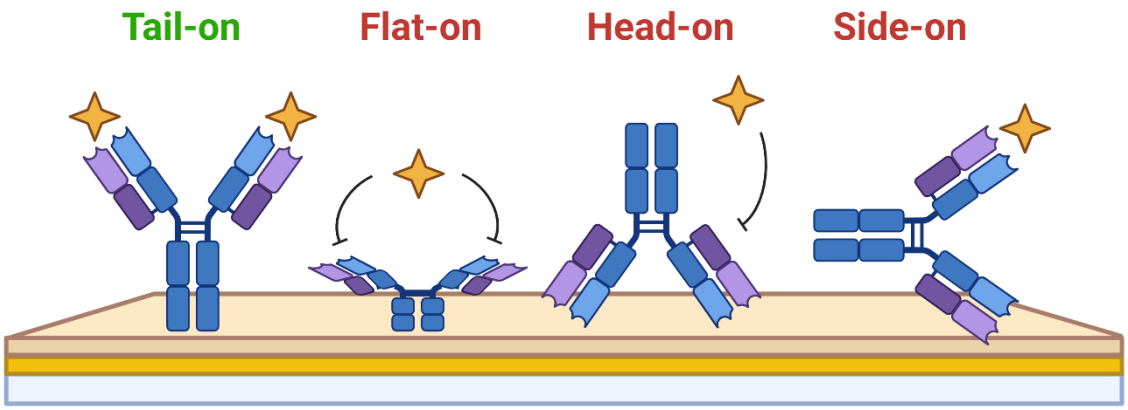


Figure 12. *Antibody different possible orientations on a surface. Tail-on, flat-on, head-on and side-on orientations.*

When permanent attachment is preferred, site-specific chemistries preserve the Fab architecture and minimize off-axis attachment (**Figure 13**). Antibody isotype and subclass (e.g., IgG1-IgG4) also matter operationally: glycosylation state, isoelectric point, and flexibility influence packing, regeneration windows, and long-term stability on the chosen surface [87,88]. Immunoassay format (direct vs sandwich; competitive vs non-competitive) is selected according to target size/valency, dynamic range, and matrix: small molecules (haptens) typically require competitive schemes, while proteins favor non-competitive (sandwich) formats to maximize sensitivity and specificity on the same nanoplasmonic transducer [46,86].

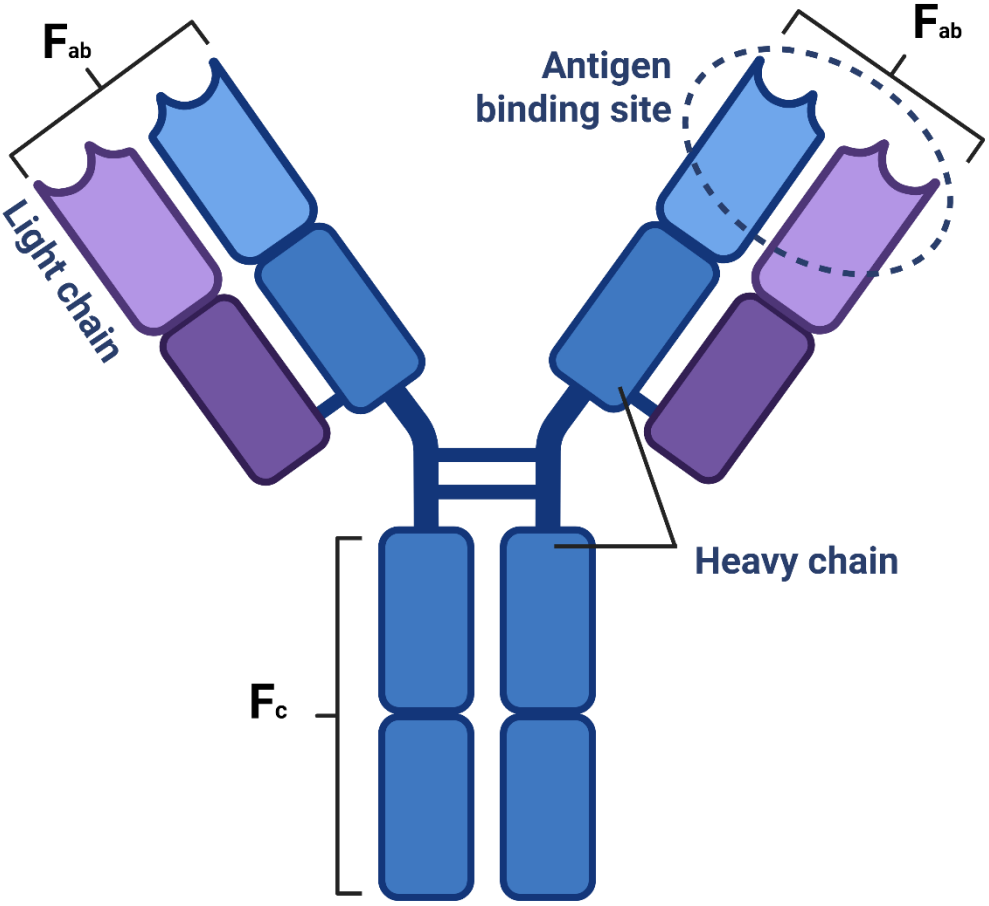


Figure 13. *Schematic representation of a basic structure of an antibody.*

Beyond antibodies, nucleic-acid probes (complementary DNA/RNA) and aptamers provide chemically defined receptors with tunable length and end-functionalization for precise vertical spacing and density control.

Aptamers can rival antibody affinities while offering high thermal/chemical stability and low batch variation; their secondary structure and ionic environment must be managed to preserve binding folds on the surface.

Enzymes enable catalytic amplification when direct affinity signal is insufficient, but their activity is sensitive to pH, temperature, and denaturants, necessitating protective linkers and gentle regeneration.

MIPs offer rugged, low-cost recognition in harsh matrices but require careful template removal and porosity control to avoid mass-transport limitations in the near field. Across all receptor classes, surface density is optimized to increase the number of accessible sites without inducing steric hindrance or multilayer growth; practical tuning uses mixed-ratio SAMs, short spacers interleaved with functional anchors, and flow-controlled loading to approach diffusion-limited capture rather than uncontrolled adsorption.

Finally, antifouling and quality control close the loop between chemistry and metrology. Low-fouling backbones (PEG, zwitterions, ultrathin polymer brushes) and reference

spots reduce false positives and allow differential subtraction of residual matrix signals [73]. Regeneration is matched to the recognition chemistry (e.g., low-pH or high-salt pulses; imidazole/EDTA) to restore baselines without eroding the capture layer. In combination, these design rules convert the inherent optical responsiveness of SPR/LSPR into low LOD/LOQ, high specificity, and reproducible kinetics in clinically relevant matrices, which is the central requirement for the biomarker assays developed in this work [50,89]

1.4.5 Cys-Protein G-Fc

For label-free plasmonic assays, the principal constraint on analytical performance is rarely the optics but the biointerface: randomly immobilized antibodies elevate nonspecific adsorption, and drift under regeneration, whereas thin, oriented Fc-capture layers preserve binding-site accessibility and convert near-surface binding into low-noise signals in complex matrices.

Protein G (and A/G) binds the heavy chain constant Fc region of IgG with high affinity, naturally orienting Fab domains toward analyte and increasing effective site density [90]. Protein G can be a cysteine-engineered variant (cys-Protein G), a single thiol enables site-specific anchoring to gold via direct Au-S coupling, producing a covalently tethered, monolayer-like Fc-capture film, maintaining activity through mild acidic cycles and keeping the recognition event within the responsive near-field of SPR/LSPR.

Compared with direct EDC/NHS grafting of whole IgG, Fc-capture reduces orientation heterogeneity and steric occlusion; compared with streptavidin-biotin, it avoids non-reversible complexes that complicate chip reuse, while remaining compatible with antifouling mixed SAMs needed for low baseline drift in serum [40,73].

1.4.6 Plasmonics in Blu-ray discs

Commercial optical discs provide prefabricated, wafer-scale diffraction gratings that can be repurposed as GC-SPR substrates at negligible cost. The spiral data tracks on Compact Discs (CDs), Digital Versatile Discs (DVDs), and Blu-ray discs (BDs) form nearly periodic relief patterns (“grooves”) with well-defined track pitch, approximately 1.6 μm (CD), 0.74 μm (DVD), and 0.32 μm (BD), and shallow groove depths (BDs = 25 nm) (**Figure 14**), parameters that dictate the accessible plasmon coupling conditions and resonant wavelengths when coated with a noble metal thin film [91].

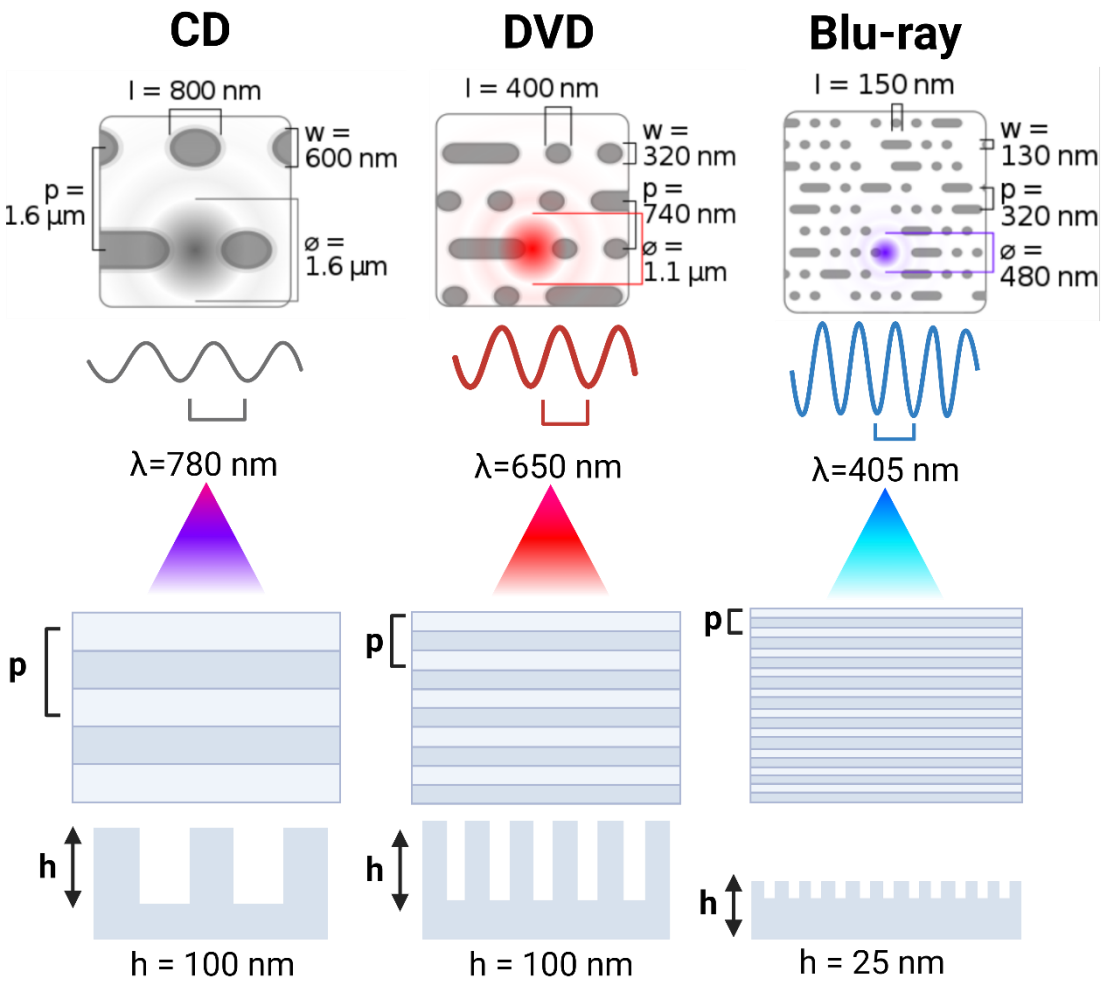


Figure 14. *Schematic representation of the structure of commercial optical discs, including the optical and physical parameters. Indicated dimensions are track pitch (p) and groove height (h).*

Because BDs use 405 nm lasers and a thinner cover layer in their intended data-storage role, their sub-wavelength pitch naturally supports plasmonic coupling in the visible to NIR range once metallized, enabling compact, low-cost optics relative to CD/DVD gratings. These geometric and optical specifications are standardized and consistently reported across educational and manufacturer sources, providing a robust basis for device design.

The GC-SPR follows the usual diffraction-based phase-matching relation, so that the BD pitch (λ =320 nm) places first-order coupling for gold films in the visible at modest incidence angles; tuning across the visible-NIR can then be accomplished by adjusting angle of incidence, polarization, metal film thickness (typically 40-70 nm for Au), or by selecting Ag for sharper, albeit less stable, resonances. The broader GC-SPR literature has repeatedly emphasized that, beyond pitch, groove depth and duty cycle critically affect resonance linewidths and figures of merit, and that large-area periodicity uniformity is essential for reproducible sensing.

From a materials perspective, optical discs are multilayer stacks built on polycarbonate (PC) (**Figure 15**). After removing the protective cover layer, the exposed, nanostructured PC can be directly metallized (e.g., e-beam evaporation or sputtering of Au/Ag) to create the plasmonic interface. Notably, several studies report that thin Au films can be deposited on PC without an adhesion underlayer (Cr/Ti), avoiding additional optical damping that would otherwise broaden resonances, although plasma pretreatments or ultrathin adhesion layers may still be used where mechanical robustness is prioritized. These practicalities make BD-derived substrates attractive for rapid prototyping of GC-SPR chips without clean-room lithography.

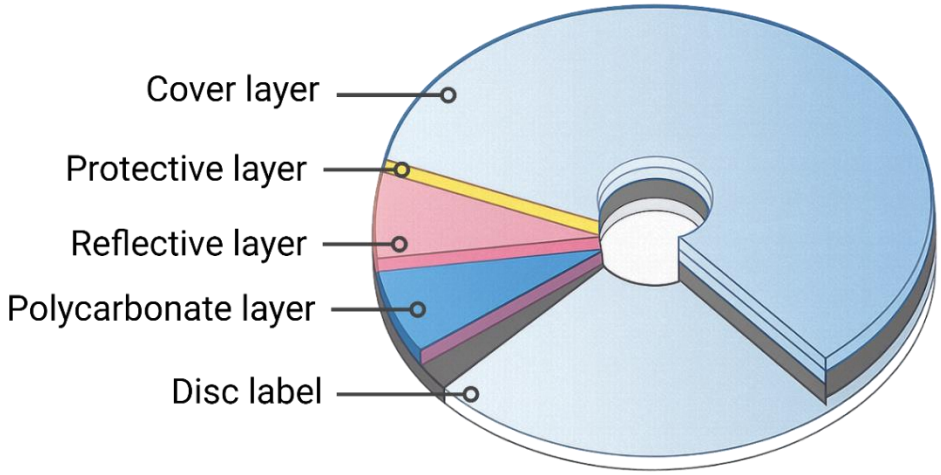


Figure 15. *Scheme of the BD disc structure: (i) disc label; (ii) polycarbonate layer (1.1 mm thick disc); (iii) reflective layer; (iv) protective layer; (v) cover layer.*

As a representative example, López-Muñoz et al. integrated PDMS microfluidics atop a metal-coated BD grating and reported bulk LODs of 6.3×10^{-6} RIU and FOM up to 3.5 RIU, together with label-free immunodetection at low ng/mL levels; while exploiting a centimeter-scale, inexpensive chip. Güner et al. demonstrated smartphone-based SPRi on metal-coated BD substrates using a 3D-printed attachment, achieving bulk LOD 4.14×10^{-5} RIU and on-chip antibody assays. These studies highlight that optical discs can support sensitive and miniaturized plasmonic sensors when combined with appropriate optics and surface chemistry [66,92].

Finally, disc architecture guides practical choices. BDs exist in HTL (High-to-Low) formats that use inorganic recording layers and in LTH (Low-to-High) variants that employ organic dyes (e.g., AZO). Manufacturer datasheets document layer stacks (e.g., reflective metals, dielectrics, cover and hard coats) and track/groove metrics (pitch 0.32 µm; shortest mark length 0.15 µm) [91].

1.4.7 Nanogratings based on Blu-ray discs

The fabrication workflow to obtain BD-derived nanogratings for GC-SPR is straightforward and compatible with low-resource settings. First, the protective cover layer is mechanically lifted or chemically softened and removed to expose the nanostructured PC. Simple sequences (mechanical peel, short solvent soak, DI water

rinse, N_2 dry) have been reported; optional oxygen plasma improves metal adhesion. A uniform Au (or Ag) film is then deposited (e-beam, thermal evaporation, or sputtering), with thickness optimized to balance resonance depth and linewidth (Au 40-70 nm is common). The resulting metalized grating supports TM-polarized coupling under collimated, off-normal illumination. Where needed, adhesion layers can be introduced, but care is taken to avoid undue optical losses; direct Au on PC has been shown effective for thin films and moderate handling, particularly when chips are housed in microfluidic cassettes.

Beyond BDs, related work has exploited DVD-R metal layers directly peeled from discs to form metal gratings for RI sensing, as well as hybrid strategies that transfer a metallized grating onto alternative substrates. While DVD-derived periods typically favor NIR excitation, these studies reinforce the broader principle that optical-disc nanogratings are a scalable manufacturing shortcut for plasmonic devices. Recent reviews of GC-SPR further contextualize disc-based gratings among other large-area fabrication routes (nanoimprint, interference lithography), emphasizing how grating topography (period, depth, duty cycle) governs resonance quality and, consequently, analytical performance [56].

Design considerations specific to biosensing follow from the BD geometry and near-field physics. The visible-range coupling enabled by BD pitch permits economical sources and detectors; the shallow groove depth yields relatively narrow linewidths when combined with optimized metal thickness and clean surfaces; and the large area and uniformity support SPRi or multi-spot assays with internal references. In this case, the BD platform is paired with oriented immunocapture and antifouling SAMs to ensure that binding occurs within the responsive near field and that the gain in optical figure of merit is translated into low concentration LOD/LOQ in serum.

1.4.8 Integration with Microfluidics

Integrating LSPR sensors with microfluidics converts the surface selectivity of plasmonic transducers into controlled, high-fidelity assays that are compatible with clinical workflows. At the scale of tens to hundreds of micrometers, laminar flow, short diffusion paths, thinning the concentration boundary layer, and enhancing mass transport to the surface so that measured association rates reflect molecular kinetics rather than transport limits. Microfluidic architectures also enable multiplexing (arrayed channels crossing nanostructure arrays), low sample consumption (μL), and portability, all while retaining the label-free, real-time advantages of LSPR for kinetic and affinity analysis [40,73].

Combining LSPR with microfluidics enhances throughput while preserving the biosensor's sensitivity. It also supports simultaneous detection of multiple biomarkers, which is crucial for complex diseases like Myasthenia Gravis, where multi-analyte screening can improve diagnostic accuracy and guide therapy selection. Furthermore, microfluidics reduces reagent consumption and allows closed-system designs, improving biosafety and sustainability.

CHAPTER 2 | MOTIVATION AND OBJECTIVES

2.1 MOTIVATION

Myasthenia Gravis (MG) is a chronic autoimmune neuromuscular disease in which pathogenic autoantibodies disrupt the neuromuscular junction (NMJ), leading to fluctuating muscle weakness, fatigue, and, in severe cases, respiratory failure. Despite advances in clinical management, diagnosis and disease monitoring remain challenging. Current diagnostic tools, such as serological assays for autoantibodies, neurophysiological tests, and bedside examinations, are either invasive, time-consuming, or lack sensitivity and specificity. Moreover, they do not reliably capture the dynamic immunopathological processes that underlie disease activity.

The central mechanism driving tissue damage in MG is the activation of the complement system. The formation of the terminal complement complex C5b-9 (sC5b-9) at the postsynaptic membrane directly contributes to neuromuscular junction destruction. With the advent of complement-targeting therapies, such as monoclonal antibodies against C5, there is a growing clinical need for diagnostic tools that can assess complement activation in real patient samples. However, no standardized, rapid, or sensitive assays exist to monitor sC5b-9 levels in MG, limiting the ability to stratify patients or to guide complement inhibitor therapies.

This gap highlights the urgent motivation for developing a biosensor platform specifically tailored to MG. These platforms have the potential to miniaturize complex laboratories procedures, integrating all the functionalities into a single device. A tool capable of detecting sC5b-9 in serum could provide clinicians with actionable information to support early diagnosis, identify patients likely to benefit from complement inhibitors, and monitor treatment efficacy. By focusing on this biomarker, this research addresses an unmet need at the interface of clinical decision-making and therapeutic innovation. The goal is to contribute to more precise and personalized care for MG patients by providing a sensitive, accessible, and real-time diagnostic approach.

2.2 OBJECTIVES

The primary objective of this thesis is to develop and optimize label-free plasmonic biosensors based on localized surface plasmon resonance (LSPR) using BD-derived nanostructures. The goal is to establish a cost-effective, rapid, and extremely sensitive diagnostic platform capable of detecting clinically relevant biomarkers in real time, with applications in a wide spectrum of diseases.

This research is particularly focused on the detection of the soluble complement complex C5b-9 (sC5b-9) in serum samples from patients with Myasthenia Gravis (MG), where complement activation plays a key pathogenic role. By addressing limitations of current diagnostic methods and harnessing the advantages of nanoplasmonic detection, this work

aims to contribute a significant step forward in the development of personalized diagnostic tools for point-of-care (POC).

2.3 SPECIFIC OBJECTIVES

1. **Design and Fabrication of a Label-Free Biosensor**

   Develop and optimize a nanoplasmonic biosensor platform using BD-derived nanostructures that enables label-free detection with high reproducibility and stability.

2. **Enhance Sensitivity and Specificity for Low-Concentration Biomarkers**

   Optimize the biosensor to detect low levels of sC5b-9, overcoming the common challenge of limited sensitivity in complex biological matrices such as serum.

3. **Selective Detection of Complement Complex in Real Patient Samples**

   Demonstrate the biosensor's capability to specifically recognize and quantify sC5b-9 in serum samples from MG patients and assess its clinical relevance.

4. **Address the Diagnostic Gap in MG**

   Provide a tool to help identify candidates for complement inhibitor therapies, addressing the current challenge of limited prognostic markers to guide such treatments.

5. **Benchmark Against Current Gold Standards**

   Compare the biosensor’s performance with existing diagnostic methods such as ELISA or radioimmunoassay, evaluating advantages in terms of cost, time, safety, and practicality.

6. **Promote Portability and Validation**

   Develop a biosensing platform with potential for miniaturization, integration with microfluidics, and use in decentralized healthcare settings.

CHAPTER 3 | MATERIALS AND METHODS

3.1 DEVELOPMENT AND CHARACTERIZATION OF NANOPLASMONIC CHIP

3.1.1 Introduction

GC-LSPR/GC-SPR biosensors are powerful tools for label-free, real-time detection of molecules at low concentrations due to their sensitivity to changes in the refractive index (RI) at the metallic-dielectric interface. This sensitivity is inherently dependent on the nanostructure of the metallic substrate, which enhances the electromagnetic field and biochemical interactions [58].

In this work, we propose a cost-effective, scalable method to fabricate nanoplasmonic biosensors by repurposing commercially available BDs as the structural substrate. Such discs inherently contain a groove height of 25 nm and periodic nanograting structures of 320 nm that can induce localized surface plasmon resonance (LSPR), eliminating the need for expensive and labor-intensive fabrication techniques such as electron-beam lithography.

Prior studies by López-Muñoz et al. have already validated optical disc-based substrates for surface plasmon resonance (SPR) sensing, laying a foundation for their broader applicability [66]. Compared to more complex optical platforms, the fabrication process is relatively simple, cost-effective, disposable, and has the potential to be scalable [93] making them excellent candidates for accessible and efficient biosensing to study complement activation in MG.

The following section details the design, fabrication, and characterization of these nanoplasmonic sensors based on nanogratings structures, which are critical for ensuring reproducible resonance behavior and minimizing background noise and spectral broadening (**Figure 16**).

This approach provides a promising platform for the integration of sensitive and portable biosensing devices for disease-specific biomarkers, particularly complement activation markers relevant to autoimmune diseases such as Myasthenia Gravis. This chapter is based on joint work with Torabi, M., Bauzon, P., Cortés, A., and Ruiz, M.

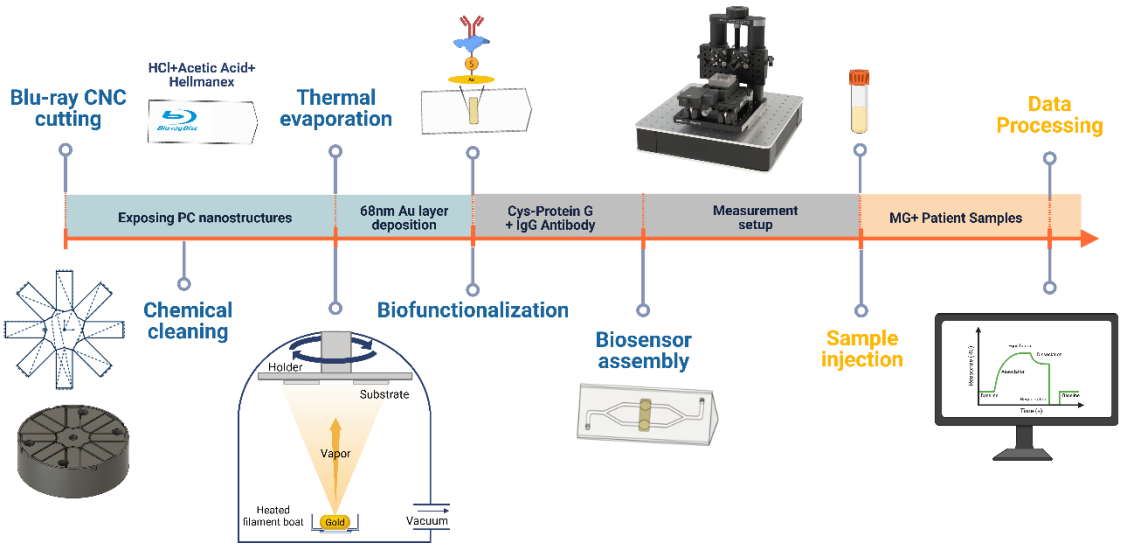


***Figure 16**. Schematic representation of the experimental pipeline of the biosensor.*

3.2 FABRICATION PROCESS OF THE CHIP

3.2.1 Chemical reagents and materials

All reagents used for substrate preparation and cleaning, including Hydrochloric acid 37% (HCl, VWR International Eurolab, 7647-01-0), Hellmanex® III (Sigma-Aldrich, Germany, 7778-53-2) and Glacial Acetic Acid (CH3COOH, Panreac AppliChem, Spain, 64-19-7) were analytical grade. Buffer compounds including Tween®-20 (9005-64-5), sodium acetate buffer (SAB, 126-96-5), and phosphate-buffered saline (PBS, pH 7.4), were obtained from Sigma-Aldrich (Steinheim, Germany).

Blu-ray discs (BD-R SL 25GB, Verbatim, USA), Matte removable vinyl (V12-BMR-DKGRN, Silhouette, USA), 140 µm thick double-sided adhesive tape (ARcare® 90106NB, Adhesive Research, USA), and 2 mm poly(methyl methacrylate) (PMMA) (Servei Estació, Spain).

All the chemical reagents and other materials including Blu-ray discs and microfluidic components are detailed in Table A1 in the Annex.

3.2.2 Chip substrate generation.

Individual sensing chips were fabricated by precision-cutting commercial BDs into rectangular pieces measuring 40 mm × 16 mm. This cutting process was conducted using a computer numerical control (CNC) router (Genmitsu 3020-PRO MAX V2, USA) equipped with a specialized diamond cutting tip. To ensure accurate alignment, uniform dimensions, and stable fixation during the CNC machining, custom support was designed and 3D-printed using Autodesk Fusion 360® software and Creality Ender 3 S1 Pro printer (**Figure 17**). BDs were firmly secured onto this custom support prior to machining. Precise CNC parameters, including spindle rotation speed (400 rpm) and XYZ-axis

alignment, were carefully configured and monitored through the Candle control software to maintain consistent quality and reproducibility across all fabricated sensing chips.

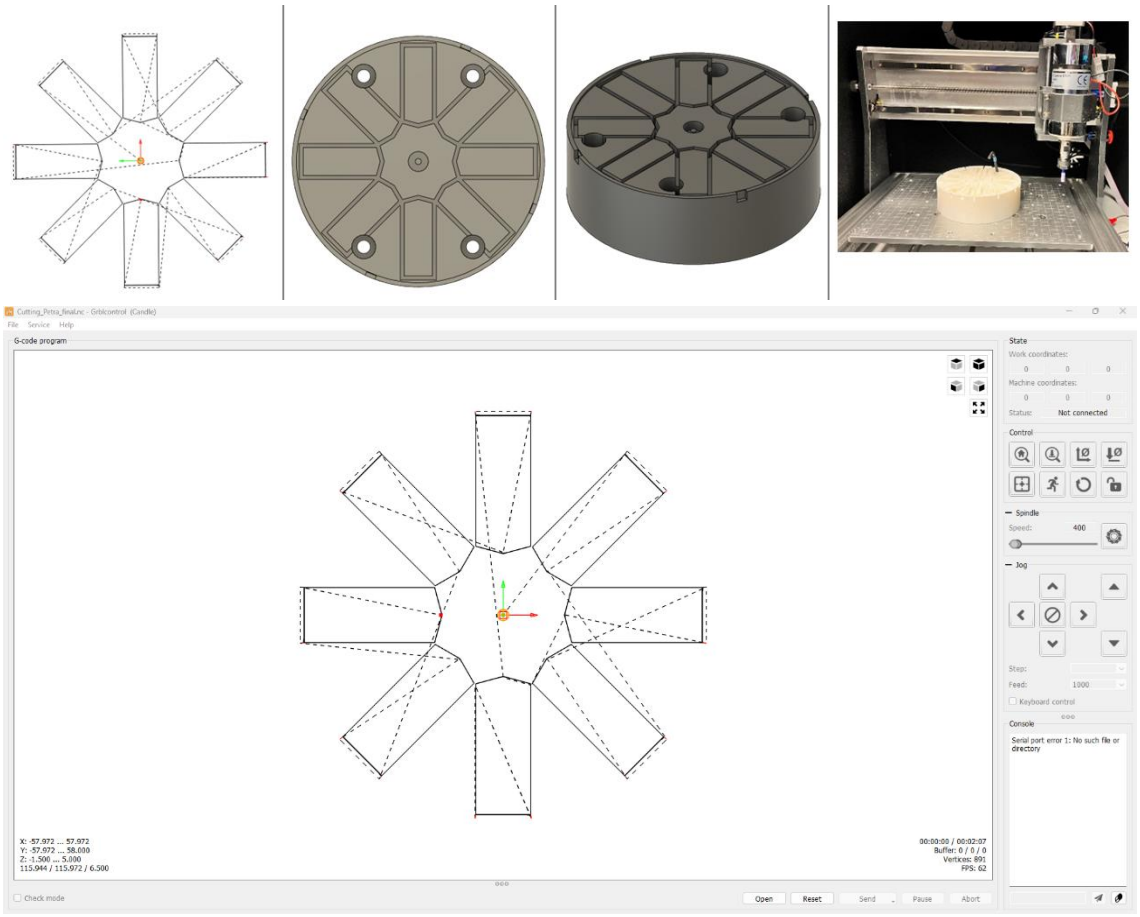


Figure 17. *CAD design of the 3D-printed support used for the CNC router cutting of Blu-ray chips. (a) Cutting pattern, (b) Top view, (c) Side view, and (d) Mounted on the CNC machine. Candle Software user interface.*

3.2.3 Protective layer removal

After CNC cutting, individual sensing chips were first rinsed thoroughly with Milli-Q water to remove machining debris. Subsequently, to strip off the reflective and protective layers present on the BDs, the chips were immersed in a 0.75 M hydrochloric acid (HCl) solution at 40 °C for 24 hours. This step ensured complete dissolution of the metallic reflective layer and other protective coatings, revealing a clean polycarbonate (PC) substrate.

To eliminate residual contaminants and organic impurities, the substrates underwent a sequential ultrasonication cleaning protocol, each step lasting 3 minutes. Ultrasonication was performed in the following order: first in a solution of 20% acetic acid, then Milli-Q water, followed by 1% Hellmanex® detergent solution, and finally in pure isopropanol. After completion of these cleaning steps, the chips were carefully dried using compressed

nitrogen gas (N_2), preventing contamination or water-spot formation on the sensor surface.

This comprehensive cleaning protocol was critical to achieving consistent, high-quality substrates, which were then ready for subsequent thermal evaporation of the gold layer, ensuring reproducibility and optimal biosensor performance.

3.2.4 Gold thermal deposition

Before thermal deposition, we want to define a sensing area on the chip. For this purpose, a custom vinyl mask was designed using Silhouette Studio® software and cut with a Cameo 4 plotter (Silhouette, USA) and placed onto the clean PC chips as a deposition mask. Following this, the masked chips were taken to the clean room facilities for thermal evaporation of gold (Au) under high vacuum (10^{-7} mbar) at a deposition rate of 1 Å/s using an Oerlikon Leybold Univex 450B system. A 68 nm-thick Au layer was deposited, after which the vinyl mask was removed by peeling it off, revealing the defined sensing zone. Any excess glue was removed carefully with isopropanol and dried with N_2 (**Figure 18**).

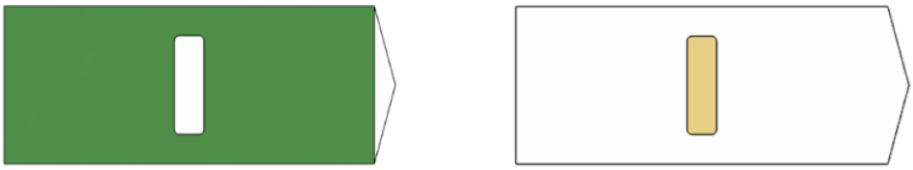


Figure 18. *Vinyl-masked chip before and after gold deposition.*

3.2.5 Scanning electron microscopy analysis

Scanning Electron Microscopy (SEM) was performed to characterize and confirm the effectiveness of the cleaning process applied to the polycarbonate (PC) substrates and to verify the uniformity, homogeneity, and integrity of the thermally deposited gold layer. SEM imaging also allowed evaluation of gold coverage over the nanograting structures inherent to BDs substrates, which directly influences the plasmonic performance of the biosensor.

The substrates were imaged using a Nova NanoSEM microscope (FEI Company), employing accelerating voltages ranging from 5 to 10 kV to achieve optimal resolution without surface damage or charging effects. Multiple areas across different chips were analyzed at various magnifications to ensure representative coverage and consistency in substrate preparation.

3.2.6 Microfluidic system

Integration of microfluidics significantly enhances sensor performance by providing controlled sample delivery, reproducible sample volumes, and reduced variability, essential for real-time sensing applications. Therefore, a microfluidic layout was computationally optimized prior to physical prototyping, ensuring stable laminar flow conditions, uniform analyte distribution, and reproducible biosensor responses.

The microfluidic design was done in Autodesk Inventor Professional® and to ensure optimal fluid flow and uniform distribution across the sensing area, COMSOL Multiphysics® simulations were conducted employing the laminar flow interface module.

The microfluidic system consisted of one inlet and one outlet, a main channel (1 mm wide), from which two symmetrical branches diverge at 60° angles leading to two circular sensing chambers (3 mm diameter). These sensing chambers are centrally positioned to enable dual and parallel measurements on the same substrate, which increases efficiency and replicability. The vertical height of the microfluidic channels is 140 µm, defined by the thickness of the double-sided adhesive tape used as the microchannel spacer (**Figure 19**).

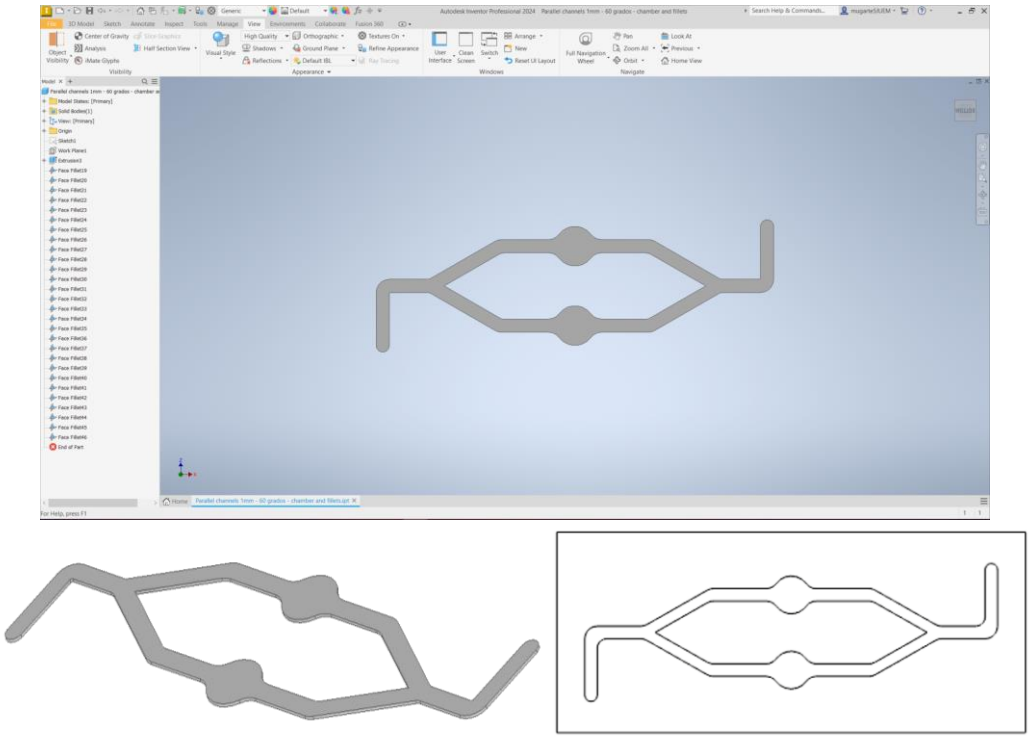


Figure 19. *CAD design of the microfluidic channel architecture created in Autodesk Inventor Professional®.*

The CAD design was exported in *mphi* format to COMSOL Multiphysics®, where simulations were performed using the single-phase laminar flow module (**Figure 20**). The simulation setup included defining boundary conditions and material properties such as fluid (water) and channel walls (plastic-coated paper, acrylic plastic, and PMMA). The output included spatial velocity distributions, helping to assess the suitability of the design for steady-state sensing applications.

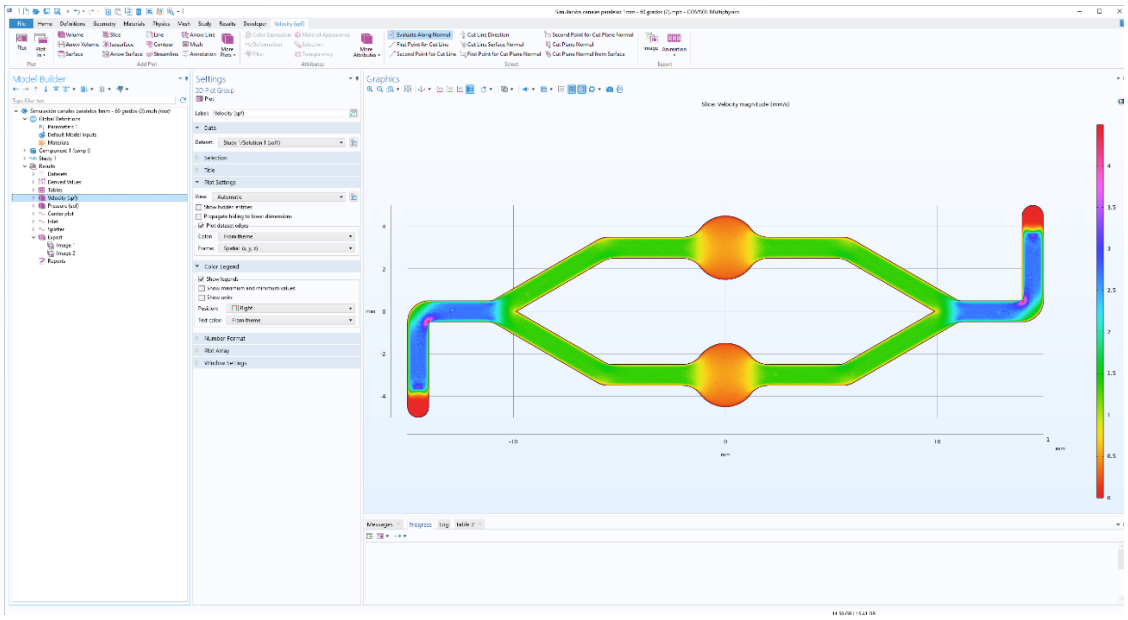


Figure 20. *COMSOL Multiphysics® interface showing flow simulations within the microfluidic layout.*

Once finalized, the microfluidic pattern was physically fabricated by cutting the double-sided adhesive tape using a Silhouette Cameo 4 plotter, which offers precision cutting suitable for microfluidic prototyping. The blade was configured for depth = 4, pressure = 33, and cutting speed = 3, parameters that were empirically optimized to cleanly cut through the tape while preserving adhesive integrity (**Figure 21**).

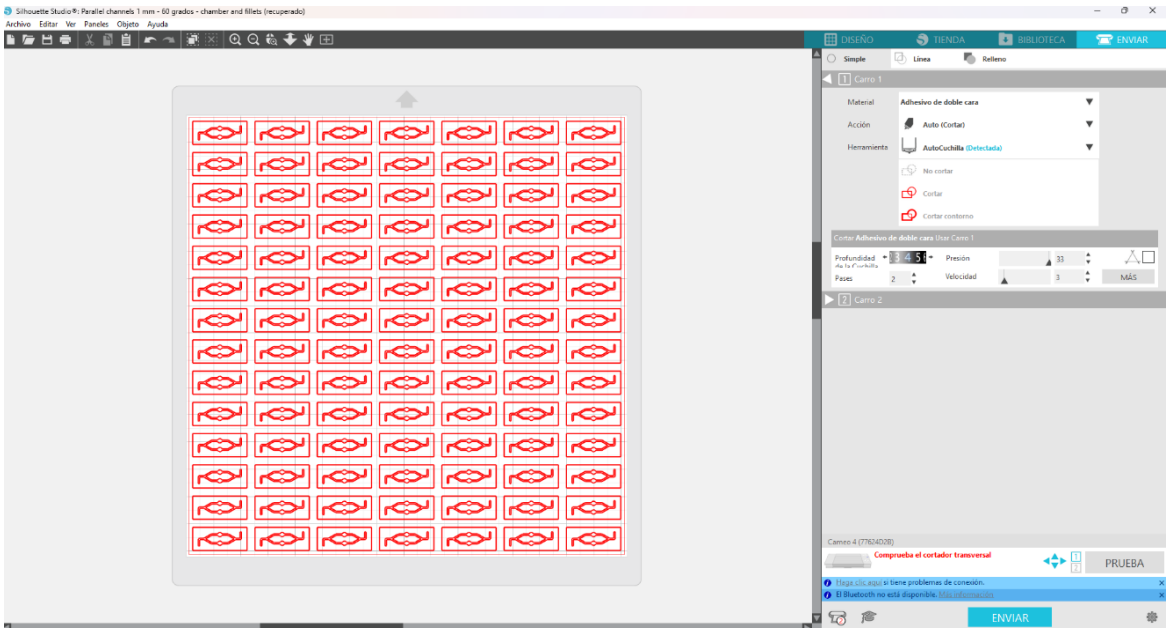


Figure 21*. Silhouette Studio interface for configuring plotter parameters and visualizing the cutting path.*

3.2.7 Optical Lid

The uppermost layer of the chip consists of a transparent PMMA sheet with a thickness of 2 mm, serving as the optical lid, sealing the microfluidic channels, and facilitating optical measurements.

This component not only seals the microfluidic channels but also allows light to transmit through the sensing regions without distortion. Two 2.25 mm diameter holes were laser-cut into opposite corners of the PMMA lid to serve as inlet and outlet ports, precisely aligned with the microfluidic layer beneath.

The cutting process was performed using a CO_2 laser cutter (Omtech, K40+, USA). The lid design was imported into LightBurn, the laser cutter's control software. The parameters for laser cutting were optimized for 2 mm PMMA, ensuring clean edges and minimal thermal deformation (**Figure 22**).

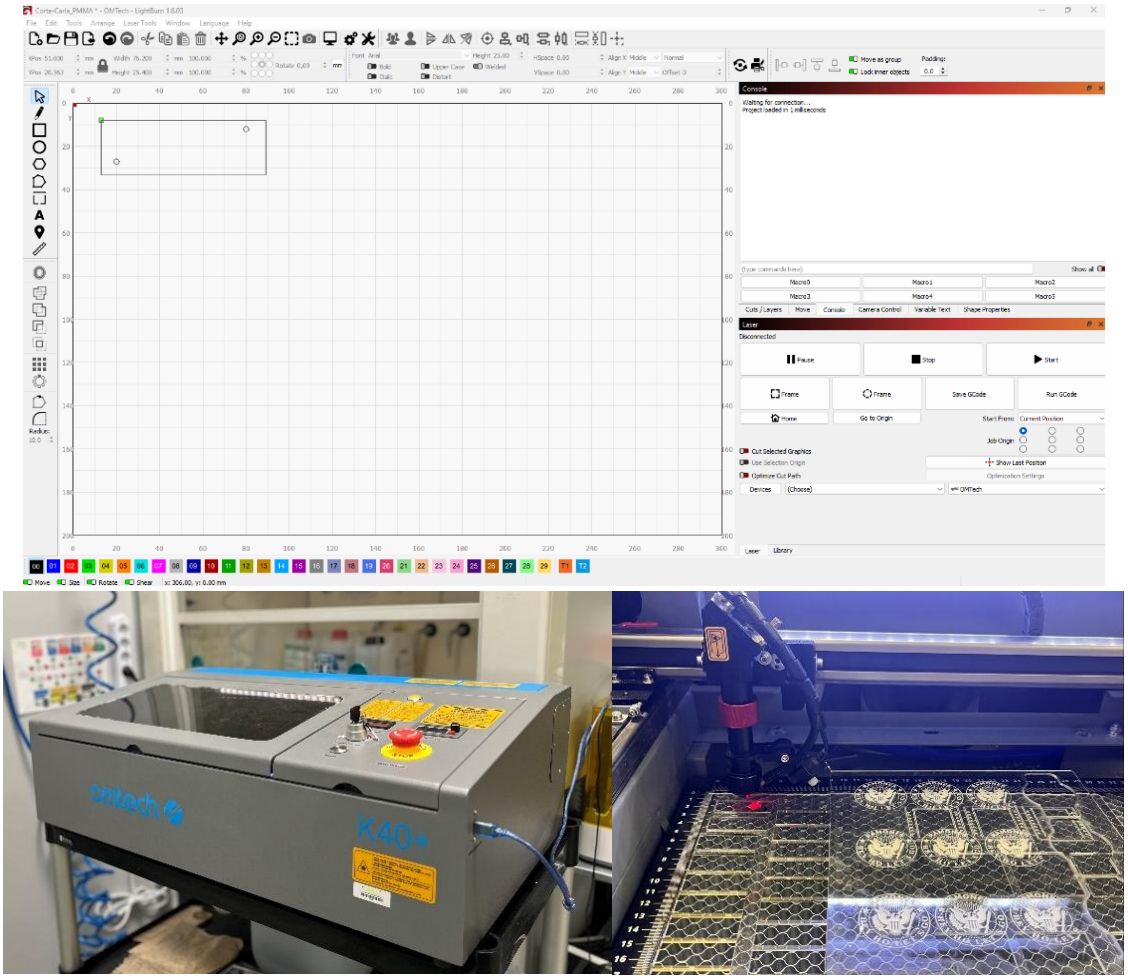


Figure 22. *LightBurn software user interfaces with the preview of the patterned lid and the parameter selection and on the bottom the laser cutter setup.*

3.2.8 Chip assembly

After fabrication, all components (Au-coated polycarbonate substrate, adhesive microfluidic layer, and PMMA lid) were assembled to form the complete sensing chip. The double-sided tape served both as the fluidic layer and adhesive interface, enabling a clean, leak-proof bond between layers. (**Figure 23**)

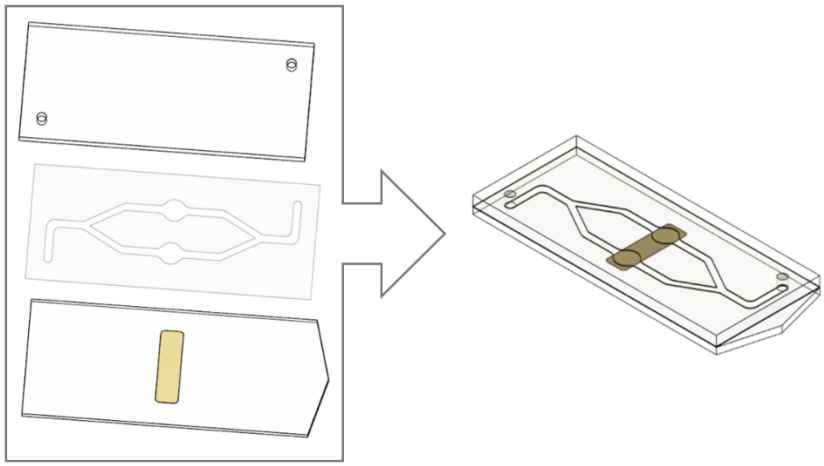


Figure 23. *Expanded view of the sensor assembly: a) PMMA Lid, b) Double-sided tape microfluidics (140 µm), c) Au-coated PC substrate (68 nm), d) Final assembled sensor.*

Prior to microfluidic chip assembly, the PMMA lid was thoroughly cleaned using 70% ethanol to remove any dust particles, surface residues, or artifacts resulting from the manufacturing process. This cleaning step was essential to achieve uniform sealing and maintain reproducible optical and fluidic performance.

The microfluidic chip assembly required precise manual alignment of the PMMA lid over the sensor substrate to ensure exact alignment between the inlet/outlet ports in the PMMA lid and the underlying microfluidic channels and sensing chambers. Proper alignment was crucial because even minor misalignment could result in fluid leaks, inconsistent flow rates, and measurement inaccuracies.

Following alignment, gentle and uniform manual pressure was applied across the assembled device, carefully removing any air bubbles trapped at the interface between the lid and adhesive layer. Removal of trapped air was vital to maintain optimal fluid dynamics, ensure leak-free sealing, and prevent disruption to the sensor's optical properties (**Figure 24**).

It is important to note that the biofunctionalization step of the sensor substrate was completed separately, prior to assembly of the microfluidic system (as detailed previously in Section 1.2.4). This approach ensured that bioreceptors remained undisturbed, uniformly immobilized, and active under controlled conditions, thereby enhancing reproducibility and functional integrity of the assembled biosensor.

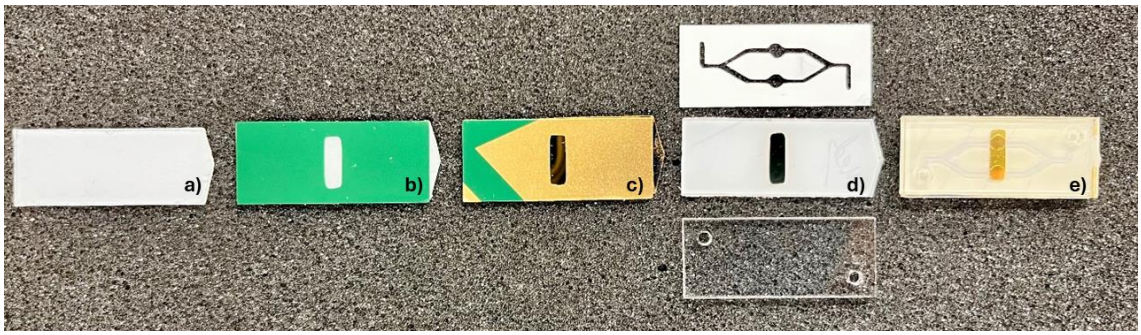


***Figure 24**. Overview of the fabrication and assembly workflow: a) PC substrate, b) Vinyl masking, c) Gold deposition, d) Adhesive layer integration, and e) Final chip.*

3.2.9 Sensing platform setup

We developed an LSPR sensing platform at the Biosensors for Bioengineering group at The Institute for Bioengineering of Catalonia (IBEC) and allows real-time monitoring at a fixed angle of incidence ($\theta = 45°$). The optical platform integrates a microfluidic system, and an optomechanical platform designed for stable measurements.

The optical setup consists of a broadband halogen light source (Ocean Optics HL-2000, USA) covering the 360-2400 nm spectral range, coupling optics (F230SMA-B, 633 nm, f = 4.43 mm, NA = 0.56 and F220SMA-532, 532 nm, f = 10.90 mm, NA = 0.25), a Ø550 µm core optical fiber (400-2200 nm) arranged at a 45° fixed angle. Light from the source is collimated and passes through a polarizing element before illuminating the sensing spot on the chip. The reflected light is collected by a second collimator and directed to a spectrophotometer (Avantes NEXOS, Netherlands).

The mechanical stage comprises a motorized linear stage with built-in controllers (Zaber Technologies, T-LSM025A, USA) and a manual translation/rotation stage (ThorLabs, XYR1/M, Germany) (**Figure 25**). We carefully adjusted the position of the optical fiber and the chip to ensure precise alignment of the light beam with the sensing area.

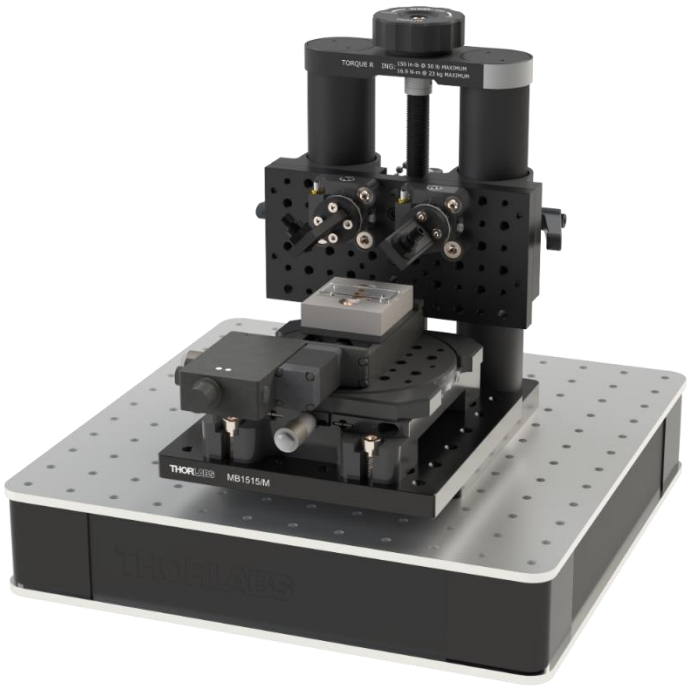


Figure 25. *A schematic representation of the optical sensing platform.*

Reliable and reproducible fluid handling is crucial for achieving stable and accurate biosensing measurements. To this end, we implemented an integrated microfluidic system composed of several components. A precision syringe pump (KD Scientific, KDS 101-CE, USA) was employed to ensure precise fluid delivery rates and consistent flow control. The flow rate can be set from the panel, to achieve the desired flow conditions i.e., 40 μL/min.

Additionally, an integrated bubble trap (Elveflow, Elvesys group) was included to eliminate air bubbles that could interfere with sensor performance or disrupt stable fluid flow. A vacuum pump (SparkFun Electronics, USA) further facilitated bubble prevention by enabling quick priming and efficient degassing of the fluidic channels prior to experimentation (**Figure 26**).

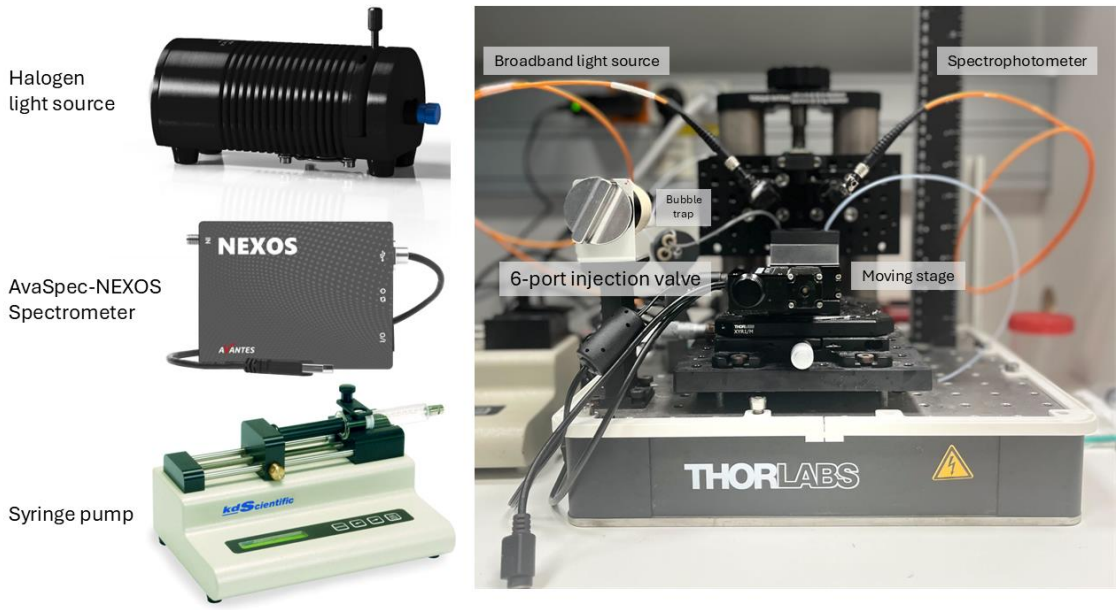


Figure 26. *General overview of the experimental LSPR sensor setup with the microfluidic system and opto-mechanical system.*

Sample injections were conducted using a manual 6-port injection valve (Cheminert C22-3186, Valco Instruments Co., USA), which allows the continuous flow of the running buffer alongside accurate and repeatable sample loading. The valve is equipped with a loop of precisely 200 µL internal volume, ensuring consistent and reproducible injection volumes for each analyte measurement. During normal operation ("closed state"), running buffer flows through the sensor system; when injecting a sample ("open state"), the valve redirects the fluid path, allowing the loaded sample loop contents to enter the microfluidic chip.

Connections between system components were made using chemically resistant PTFE tubing (internal diameter × outer diameter: 0.8 mm × 1.58 mm; Sigma-Aldrich, Z609714, Germany). This tubing securely connects the injection valve, bubble trap, vacuum pump, syringe pump, and waste reservoir, ensuring robust and leak-proof fluidic pathways.

To interface the PTFE tubing directly with the chip's PMMA lid, Mini Luer tube tuck connectors (ChipShop, Fluidic 1579, Germany) were employed. These connectors offer a leak-proof seal and provide simple, reliable insertion of 1/16-inch tubing into the chip. To further enhance reliability and prevent accidental tubing disconnections caused by platform movements, we designed and 3D-printed a custom fixation lid equipped with integrated magnets. This lid firmly secures the Luer connectors and tubing in position on a custom-designed, in-house fabricated chip holder, thus maintaining stable fluid connections and ensuring consistent sensor operation throughout experiments (**Figure 27**).

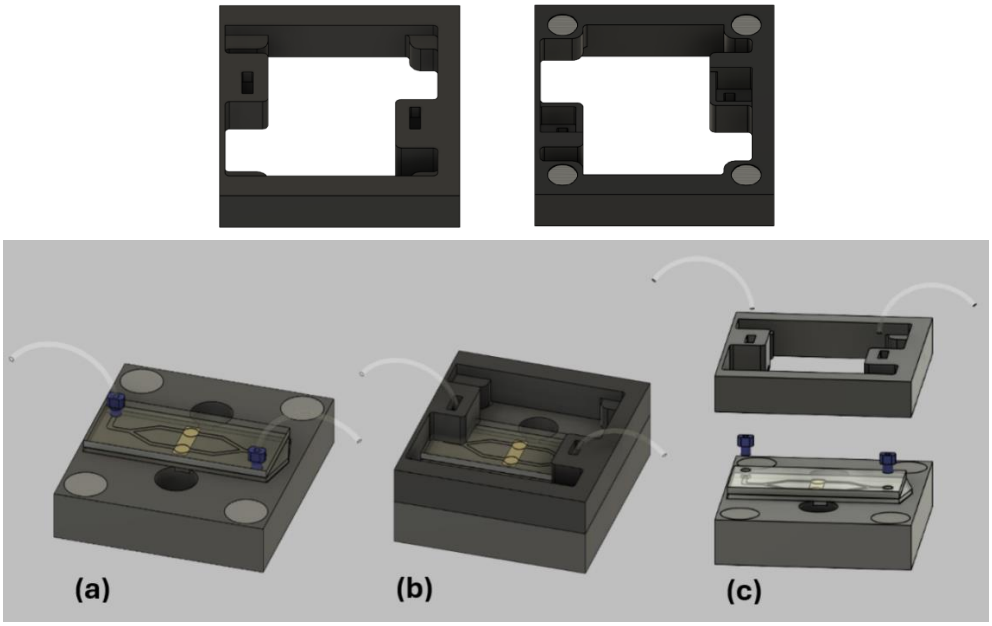


Figure 27. *Schematic representation of the fixation lid and the microfluidic connected chip on the platform holder. A) chip with luer connectors on the platform holder, b) positioning of the lid and the connected chip, c) side view of the lid chip connecting sequence.*

The reflected spectra are recorded using the AvaSpec-NEXOS™ spectrometer and visualized through a custom LabVIEW interface, which we developed specifically for this platform. The software manages real-time spectral acquisition, data fitting, and controls the mechanical components.

In the Spectrometer and Fitting tab of the interface (**Figure 28A**), we can define all acquisition and analysis parameters, including the number of channels, integration time, averaging, and dark correction. We also control fitting parameters such as pixel range, model selection, polynomial order, and LSPR guess value.

In the Sensing tab (**Figure 28B**), we monitor the LSPR shift in real time as data points are collected. This enables us to track changes in refractive index on the sensor surface dynamically during analyte binding or elution events.

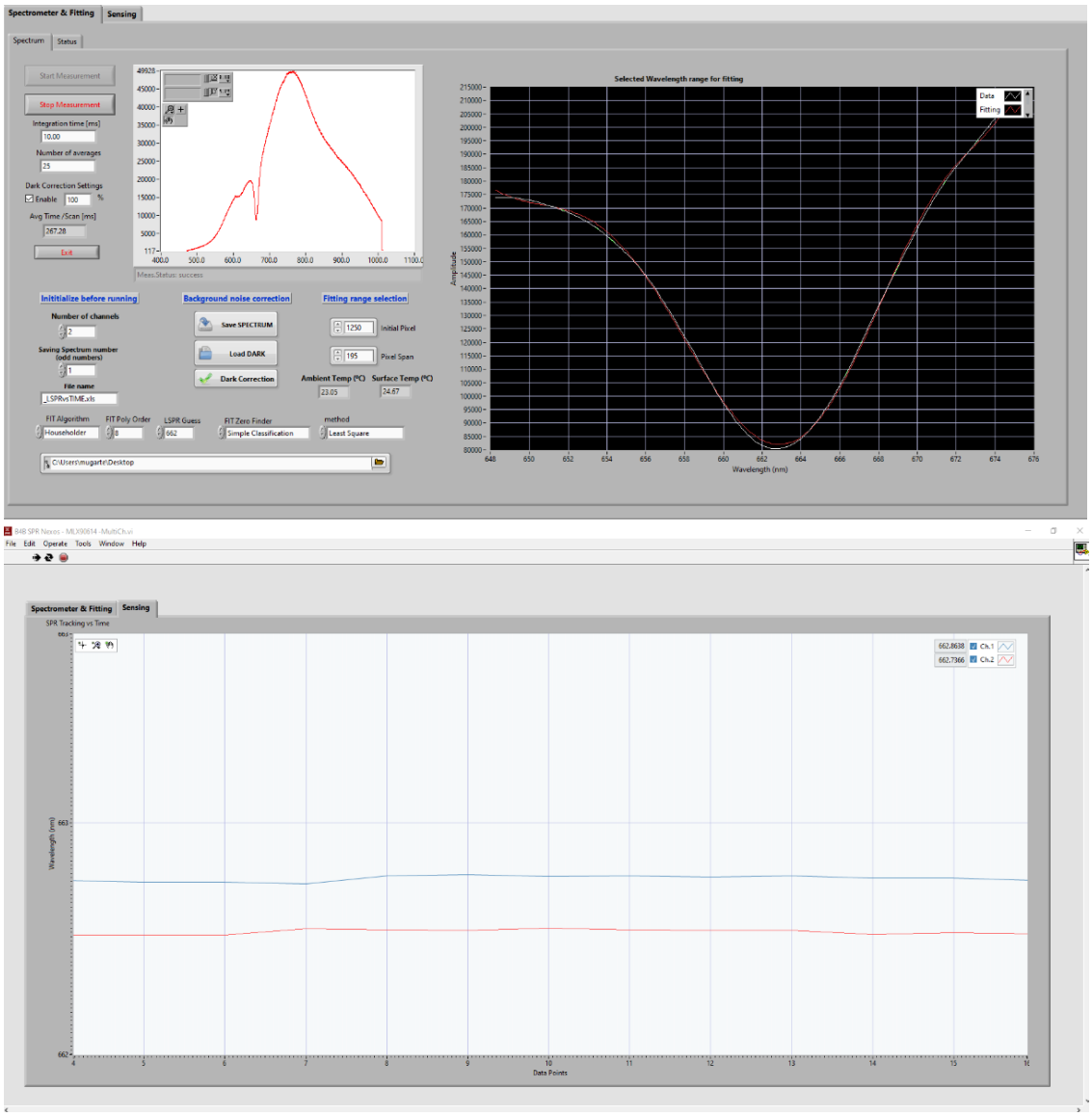


Figure 28. *LabView software user interface. A) Spectrometer and Fitting tab to allow parameter selection, customization, and b) Sensing tab to visualize real-time data point collection.*

3.2.10 Data Analysis

Sensor response data obtained from the nanoplasmonic biosensors were processed and analyzed using multiple software packages to ensure robust and accurate interpretation. Initially, raw sensor data, represented as wavelength shifts (Δλ, nm), were recorded and organized using Microsoft Excel (Microsoft, USA) for preliminary data handling, baseline correction, and initial visualization. Subsequently, Origin 8.0 software (OriginLab, USA) was employed for detailed graphical representation, enabling precise visualization of biosensor response dynamics and facilitating the evaluation of response trends and reproducibility across replicates.

Quantitative data analysis and graphical representation, including sensor calibration, curve fitting, and statistical comparisons, was performed using GraphPad Prism

(GraphPad Software, Inc., USA). Prism software was specifically used to fit experimental data into a four-parameter logistic (4PL) regression model, facilitating reliable interpolation of unknown analyte concentrations from the biosensor calibration curves. Prism also enabled rigorous statistical evaluation of assay sensitivity, specificity, reproducibility, and precision through appropriate statistical tests, including the determination of limits of detection (LOD), confidence intervals (CI), and regression goodness-of-fit metrics (R^2).

In summary, sensor response ($\Delta\lambda$, nm) was systematically correlated with analyte concentrations (ng/mL) to yield quantitative, interpretable analytical results, essential for both calibration and clinical validation phases of the biosensor development.

3.2.11 Bulk calibration

To assess the bulk refractive-index (RI) sensitivity of the fabricated nanoplasmonic biosensor chips, a systematic calibration procedure was conducted using hydrochloric acid (HCl) solutions at varying concentrations. HCl concentrations prepared for the calibration experiments included 0.5 M, 0.25 M, 0.1 M, 0.05 M, and 0.025 M, spanning a wide refractive index range to thoroughly evaluate sensor performance. The refractive index of each HCl solution was independently measured using a portable digital refractometer (Reichert Technologies, Brix/RI-Chek, USA), ensuring accurate and reproducible RI reference values for calibration purposes (**Table 5**).

During calibration, 200 µL aliquots of each HCl solution were sequentially injected over the sensing surface at a fixed flow rate, and the resulting changes in the plasmonic resonance wavelength shift ($\Delta\lambda$, nm) were continuously monitored and recorded. The relationship between the measured sensor response ($\Delta\lambda$) and the corresponding refractive index of each solution was plotted, allowing determination of the sensor's bulk sensitivity in terms of wavelength shift per refractive index unit (nm/RIU). This calibration step provided a foundational assessment of sensor sensitivity, confirming the sensor's capability to detect subtle changes in refractive index prior to biospecific detection assays.

Table 5. *Refractive Index values of the HCl solutions used in the bulk calibration of the sensor chips.*

Solution	Measured RI
MiliQ water	1.3325
0.5 M HCl	1.3368
0.25 M HCl	1.3346
0.1 M HCl	1.3334
0.05 M HCl	1.3331
0.025 M HCl	1.3330

3.3 SENSOR SURFACE BIOFUNCTIONALIZATION

3.3.1 Introduction

In this chapter, we describe the biofunctionalization strategy of cys-Protein G self-assembles monolayer (SAM) immobilization with an IgG antibody and evaluate the performance of the functionalization in different matrixes. The performance of any label-free plasmonic biosensor critically depends on the quality and stability of its biorecognition layer [94]. SAMs offer a versatile platform for tailoring surface chemistry at the nanoscale, enabling precise control over receptor density, orientation, and nonspecific adsorption [95,96]. In the context of GC-SPR, a well-ordered SAM can significantly enhance both signal-to-noise ratio and overall sensitivity by reducing background refractive-index fluctuations and maximizing the fraction of bound analyte that contributes to the evanescent field [83].

Among SAM strategies, cysteine-tagged Protein G (cys-Protein G) has emerged as an effective means to orient immunoglobulin G (IgG) antibodies via their Fc region, thereby exposing antigen-binding (Fab) domains toward the sample matrix [97]. Oriented immobilization not only increases the active capture probe density but also preserves antibody activity over extended assays, which is essential when detecting low-abundance targets such as complement sC5b-9 in complex media [98]. Despite these advantages, many reported Protein G-based surfaces neglect the role of electrostatic pre-concentration at the protein's isoelectric point (pI). Pre-concentrating cys-Protein G near its pI enhances thiolate-gold binding and yields higher surface coverage, translating into improved assay sensitivity [90].

Conventional chemical coupling methods, such as EDC/NHS activation, often require multiple reagents, long incubation times, and can result in random receptor orientation or crosslinking artifacts, limiting throughput and scalability. In contrast, cys-Protein G SAMs can be generated in a single step under mild conditions, consume fewer reagents, and are readily compatible with batch fabrication of disposable chips. In this chapter, we build established GC-SPR optimization principles [83] to develop an improved, pI-driven cys-Protein G immobilization protocol. Our goal is to maximize the active antibody population, minimize nonspecific fouling, and deliver the robust, reproducible biointerface required for sensitive detection of sC5b-9 in human serum.

3.3.2 Biofunctionalization strategy

Physical adsorption is a widely used and straightforward biofunctionalization strategy in which biomolecules adhere to a sensor surface through non-covalent intermolecular forces, including electrostatic interactions, hydrogen bonding, van der Waals forces, and hydrophobic effects [99]. The strength and nature of these interactions depend on both the surface chemistry and biomolecular structure, making adsorption sensitive to environmental parameters such as pH and temperature. While this approach allows immobilization via multiple binding sites, it often results in random orientation of the receptors and can induce partial denaturation [90].

On gold surfaces, cysteine-tagged proteins exploit the strong affinity of thiol groups for Au-S chemisorption, while the remaining protein engages in additional physisorption contacts that stabilize the monolayer. This dual chemisorption-physisorption mechanism enhances the longevity, reproducibility, and sensitivity of the biointerface. Lee *et al.* (2007) demonstrated an effective biofunctionalization protocol for cys-Protein G and human IgG antibodies on gold, and the method employed here is a modified version of that strategy [90].

3.3.3 Materials and Methods for immobilization

For sensor biofunctionalization and assay development, all buffer solutions including Tween®-20, saline acetate buffer (SAB), phosphate-buffered saline (PBS, pH 7.4), 2-[4-(2-hydroxyethyl)-1-piperazinyl] ethanesulphonic acid (10 mM HEPES, pH 7.0) buffer, and CHAPS (3-[(3-Cholamidopropyl)dimethylammonio]-1-propanesulfonate hydrate, 331717-45-4) were obtained from Sigma-Aldrich (Steinheim, Germany). For anti-fouling PLL20-g(30)-MPEG45 was obtained from NanoSoft Biotechnology (NC, USA) and bovine serum albumin from Sigma-Aldrich (BSA, pH 5.2).

Recombinant cys-Protein G was purchased from ProSpec (catalog #PRO-1238). Purified rat anti-mouse IL-6 antibody and recombinant mouse IL-6 was obtained from BD Pharmingen™. Mouse anti Human SC5b-9 antibody was purchased from Bio-Rad Laboratories, and purified Human Complement sC5b-9 Complex was acquired from Novus Biologicals. Commercial Human Serum (CHS) was purchased from Merck Life Science (S7023-50ML). It contains various plasma proteins, amino acids, polypeptides, growth factors, fat, carbohydrates, nucleic acid derivatives, hormones, inorganic minerals, and vitamins. According to Merck Life Science the sera is pooled from multiple normal subjects and collected from clotted whole blood without additives. The donor pool consists of up to 200 donors and are sterile filtered through a 0.22-micron filter.

3.3.4 Optimization (model IgG)

To optimize the biofunctionalization process, the biosensor was initially characterized using an anti-Interleukin-6 (anti-IL-6) antibody. IL-6 was selected for preliminary testing due to its well-characterized nature and availability as a standardized antibody, facilitating consistent and reproducible optimization of immobilization parameters. Additionally, cys-Protein G has been shown to bind various IgG subtypes with differing affinities (**Table S4**), specifically recognizing the Fc region [90], which makes it suitable for oriented antibody immobilization regardless of target specificity.

IL-6 was also a relevant biological choice, as it is an inflammatory cytokine known to be elevated in myasthenia gravis (MG) patients and has been implicated in promoting complement activation through increased C5 levels. Therefore, although IL-6 is not the target of interest in this work, it served as a biologically and technically appropriate surrogate to fine-tune sensor functionalization prior to implementing anti-C5b-9 antibodies for specific detection [26].

3.3.4.1 Pre-concentration of the protein

The effect of pre-concentrating of cys-Protein G near its pI was evaluated. Protein immobilization was therefore evaluated at three different pH conditions (4, 5 and 6) in SAB buffer to identify conditions that promote optimal surface coverage and stability of the immobilized protein layer.

For these experiments, cys-Protein G was prepared at 20 µg/mL in SAB at each pH and immobilized onto freshly cleaned sensor surfaces. Subsequently, a standard antibody (anti-mouse IL-6, BD Pharmingen; 50 µg/mL) was introduced after protein immobilization. The functionalized chips were evaluated by injecting 200 µL of recombinant mouse IL-6 (200 ng/mL in PBST 0.5%).

Separate sensor chips were prepared and used individually for each pH condition to ensure consistency and prevent cross-contamination. Immobilization efficiency and sensor response were evaluated based on the wavelength shift obtained upon injection of the antigen. The highest and most stable biosensor response was observed at pH 4; therefore, this condition was selected as optimal for subsequent immobilization steps.

3.3.4.2 Protein and antibody concentration

Following the selection of the optimal immobilization pH, experiments were conducted to further optimize the surface biofunctionalization by varying the concentrations of cys-Protein G and antibody.

Initially, different concentrations of cys-Protein G (20, 50, and 100 µg/mL in SAB at pH 4) were immobilized while maintaining a fixed antibody concentration of 50 µg/mL. Subsequently, antibody concentrations (20, 50, and 100 µg/mL) were evaluated using the optimal concentration of cys-Protein G (100 µg/mL, pH 4). The biosensor responses were evaluated based on the magnitude of the wavelength shifts obtained during antigen injection.

Optimal immobilization conditions were determined to be 100 µg/mL of cys-Protein G and 50 µg/mL of antibody, as this combination consistently yielded the strongest and most reproducible biosensor signals. These optimized parameters were utilized throughout the remainder of this study for the biofunctionalization of all plasmonic sensor chips.

3.3.5 Standard biofunctionalization workflow

Based on the optimized parameters described above, sensor surfaces were biofunctionalized via an *ex-situ* method. Prior to functionalization, gold-coated sensor substrates were activated for 30 minutes by UV/ozone treatment Procleaner (Bioforce Nanosciences). This activation step enhanced surface hydrophilicity and removed potential organic contaminants, promoting uniform adsorption of the protein layer.

Next, a 20 µL droplet of 100 µg/mL cys-Protein G in SAB buffer (pH 4) was deposited onto the activated surface and incubated for 1 hour at 4 °C. Unbound or weakly adsorbed protein was then rinsed off thoroughly with PBST 0.5%. Next, 50 µg/mL of IgG antibody

was deposited in the same manner and incubated under identical conditions, followed by a second PBST 0.5% rinse to eliminate non-adsorbed antibody.

3.3.5.1 Anti-fouling

Our anti-fouling strategy combined PLL-PEG with 1% BSA to minimize nonspecific adsorption. Polyethylene glycol (PEG) is considered the gold standard for resisting protein adsorption because its hydrated polymer brush increases surface hydrophilicity and sterically repels approaching biomolecules. Bovine serum albumin (BSA), a highly abundant plasma protein, exhibits strong affinity for hydrophobic and metallic surfaces like gold, effectively passivating exposed sites and further suppressing background binding in complex serum matrices [99,100].

To block non-specific adsorption, the surface was treated with 0.75 mg/mL PLL-PEG diluted in HEPES buffer for 10 minutes at room temperature, then incubated overnight at 4 °C with 1% BSA. This two-step blocking regimen effectively minimizes background binding and was used for all subsequent biofunctionalization steps. This biofunctionalization workflow consistently produced robust and reproducible biorecognition surfaces, ensuring optimal biosensor performance for subsequent analytical measurements (**Figure 29**).

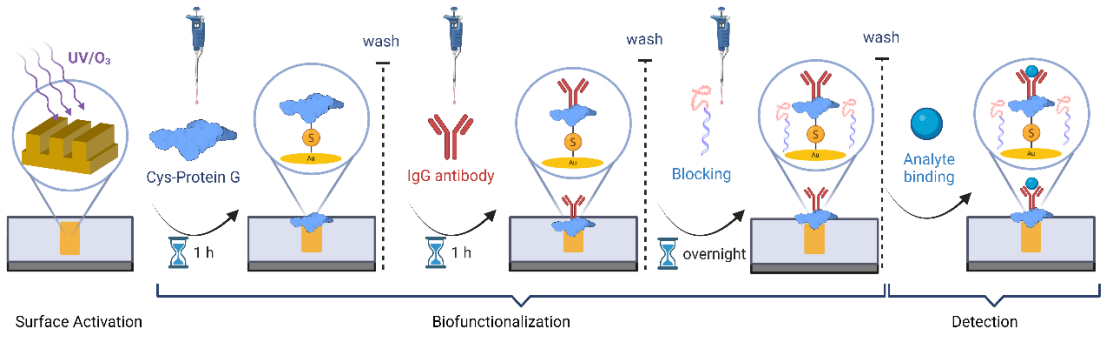


Figure 29. *Schematic representation of the biofunctionalization technique ex situ of the sensor surface. Created in BioRender. Ugarte Orozco, M. (2025) https://BioRender.com/orlbaea*

3.3.6 Time stability test

To assess the long-term stability and reliability of the biofunctionalized cys-Protein G/anti-C5b-9 sensor surfaces, we conducted a systematic evaluation over an extended period. Freshly biofunctionalized sensor chips were stored under two different conditions to investigate how environmental factors might influence biorecognition layer integrity: immersed in phosphate-buffered saline (PBS) and stored dry, both at 4 °C. These conditions mimic typical storage environments in laboratory and clinical settings.

Sensor stability was evaluated at multiple defined intervals: 48 hours, 22 days, and 1 month after initial functionalization. At each predetermined time point, individual biosensors were removed from storage and immediately mounted onto the GC-SPR

system. To ensure accurate measurements, the sensors were equilibrated for 5 minutes with running buffer (PBST 0.5% + CHAPS 25 mM) at a flow rate of 40 µL/min until a stable baseline was established. Subsequently, the functional stability was assessed by injecting 200 µL of recombinant sC5b-9 (100 ng/mL) diluted in the same running buffer, maintaining a flow rate of 40 µL/min. The sensor response, represented by the steady-state wavelength shift (Δλ), was continuously recorded.

To quantify stability over time, the Δλ values at each tested interval were compared against the initial response obtained immediately after biofunctionalization (day 0). This comparative analysis enabled us to identify any degradation in the recognition layer or loss of antibody binding activity. Each time point evaluation was performed on separate, independently stored sensor chips to eliminate variability associated with repeated use or regeneration processes. No regeneration steps were performed between assays to ensure that each data point reflected the intrinsic stability of the original biofunctionalized surface.

This systematic approach provides essential insights into the practical shelf-life and storage conditions required for reliable sensor deployment, contributing to the broader applicability and clinical translation of our biosensor platform.

3.3.7 Matrix effect of serum and affinity validation

To evaluate the impact of serum components on sensor performance, the functionalized cys-Protein G/Ab C5b-9 were challenged with serial dilutions of commercial human serum (CHS) prepared in PBST 0.5% (1:100, 1:50, 1:10, and undiluted). Initial optimization employed PBST alone as the running buffer, but to enhance signal stability and reduce nonspecific binding, the buffer was subsequently replaced with PBST 0.5% supplemented with 25 mM CHAPS.

Each dilution was evaluated on a fresh biofunctionalized chip: after a 5-minute baseline equilibration with PBST 0.5% + CHAPS at 20 µL/min, 200 µL of the CHS sample was injected at the same flow rate for 15 minutes, followed by a 5-minute wash with PBST 1% to remove loosely bound material. Surface regeneration between runs was achieved with a pH 2.2 glycine solution, ensuring consistent starting conditions. To determine assay accuracy, the entire procedure was repeated with CHS samples spiked with 250 ng/mL sC5b-9. All matrix-effect and accuracy data are presented in **Section 4.9.2**.

3.3.8 BRE affinity in complex matrix

One sensing spot of the plasmonic chip was functionalized with cys-Protein G + anti-C5b-9 antibody (BRE), while the other served as a control (functionalized with cys-Protein G only).

To evaluate the specific binding capability of the immobilized biorecognition element (BRE, Ab C5b-9), a control assay was performed injecting a dilution of CHS spiked with 250 ng/mL of recombinant sC5b-9 into the biosensor.

The sensing surface was divided into two regions: one spot was functionalized with cys-Protein G / Ab C5b-9 (with BRE), while the control spot was only functionalized with cys-Protein G (without BRE). After baseline stabilization with PBST 0.5% + CHAPS 25mM as running buffer, the target analyte sC5b-9 (200 µL) was injected at 40 µL/min for 15 minutes. The surface was washed with PBST 1% for 5 minutes.

The affinity of the anti-C5b-9 biorecognition element (BRE) was assessed on a dual-spot nanoplasmonic chip. One spot was functionalized with cys-Protein G and anti-C5b-9 antibody (BRE), while the other contained only cys-Protein G as a negative control. Then, both sensing spots were blocked with 0.75 mg/mL PLL-PEG for 10 minutes at room temperature and subsequently with 1% BSA overnight at 4 °C, then rinsed with PBST 0.5% to remove unbound blocking reagents. The assembled chip was mounted in the sensing platform, and PBST 0.5% + 25 mM CHAPS was used as running buffer at 40 µL/min.

After baseline stabilization, a 200 µL sample of 1:100 diluted CHS spiked with 250 ng/mL recombinant sC5b-9 was injected at 40 µL/min for 10 minutes, and the real-time wavelength shift (Δλ) recorded. Finally, the surface was washed with PBST 1% for 5 minutes at 40 µL/min to observe dissociation. No regeneration was performed; each assay was conducted on a fresh chip to ensure reproducibility.

3.4 CALIBRATION AND VALIDATION OF THE BIOSENSOR

3.4.1 Introduction

Accurate quantification of analyte concentration from plasmonic sensor responses mandates a robust calibration strategy that spans both idealized buffer conditions and biologically complex media. Calibration in buffer establishes the intrinsic relationship between resonance shift (Δλ) and known sC5b-9 concentrations, enabling determination of key analytical parameters such as limit of detection, dynamic range, and assay precision [101].

However, serum components can alter refractive-index backgrounds and introduce nonspecific interactions, necessitating parallel calibration in complex matrices to correct for matrix effects and ensure reliable performance in real-world samples [102]. To model the characteristic sigmoidal binding behavior of immunoassays and accommodate analyte saturation at high concentrations, we applied a four-parameter logistic (4PL) regression, which is widely accepted for biosensor and ELISA calibration due to its flexibility and interpretability [103]. Following matrix-matched calibration, clinical validation against well-characterized human sera confirms the assay's accuracy and suitability for detecting sC5b-9 in patient samples.

3.4.2 Materials and biological compounds

Biofunctionalized biosensors with cys-Protein G / Ab C5b-9 as previously described were used for the assays of this section.

All buffer solutions including Tween®-20, phosphate-buffered saline (PBS, pH 7.4), and CHAPS (3-[(3-Cholamidopropyl)dimethylammonio]-1-propanesulfonate hydrate, 331717-45-4) were obtained from Sigma-Aldrich (Steinheim, Germany). Dulbecco's Modified Eagle Medium (DMEM; ThermoFisher).

Patient serum samples were collected at *the Institut de Recerca Hospital de la Santa Creu i Sant Pau* (Barcelona, Spain). A total of 13 serum samples from adult donors were analyzed: 8 from patients diagnosed with AChR+ MG, 3 from patients positive for anti-MuSK antibodies (MuSK+ MG), and 2 from healthy donors. Together, the MuSK+ MG and healthy donor samples (n=5) were used as negative or blank controls, as these are not expected to contain sC5b-9 levels associated with AChR+ MG. In addition, commercial human serum (CHS) was also evaluated to further assess background signal and specificity. All procedures complied with institutional and/or national ethics standards, including the 1964 Helsinki Declaration and its later amendments.

3.4.3 Calibration curve sC5b-9 in complex matrices

Calibration curves were generated to establish a reliable quantitative relationship between measured biosensor signal (Δλ) and known concentrations of the target analyte, soluble C5b-9 (sC5b-9). To assess the influence of complex matrices on sensor performance, two distinct matrix environments were selected: Dulbecco's Modified Eagle Medium (DMEM), representing a biologically relevant, protein-rich medium potentially applicable to future cell-based assays (e.g., bead-based Cytometric Bead Array (CBA) platforms for sC5b-9 detection), and diluted commercial human serum (CHS), to simulate direct clinical serum samples.

For the initial calibration, DMEM (ThermoFisher) was chosen as the running buffer due to its complexity and clinical relevance. Prior to analyte injections, each biofunctionalized sensor chip was stabilized with DMEM flowing at 40 µL/min for 5 minutes, allowing the establishment of a stable baseline. Subsequently, serial dilutions of recombinant sC5b-9 ranging from 0.1 to 1000 ng/mL in DMEM were prepared. Each dilution (200 µL) was individually injected into the biosensor at a flow rate of 40 µL/min, and the resulting wavelength shifts (Δλ) were continuously recorded. After each analyte injection, unbound molecules were removed by washing the biosensor surface with PBST 0.5% at 40 µL/min for 3 minutes.

To evaluate sensor behavior under conditions more representative of clinical serum samples, a second calibration was conducted using PBST 0.5% supplemented with 25 mM CHAPS and 1:100 diluted CHS as the running buffer. This calibration followed the same experimental protocol as the DMEM calibration, using fresh biofunctionalized chips and identical serial dilutions of sC5b-9. Two independent biosensor chips, each with dual technical replicates, were evaluated for both matrices to ensure reproducibility and accuracy of the data.

The collected calibration data from both matrices were then analyzed using GraphPad Prism software, fitting the sensor response to a four-parameter logistic (4PL) regression

model. This nonlinear model was chosen due to its suitability for capturing the characteristic sigmoidal behavior of plasmonic immunoassays, accurately modeling both low-concentration sensitivity and high-concentration saturation of the analyte-binding response. The resulting curves provided essential analytical parameters, including limit of detection (LOD), and effective quantification range, crucial for subsequent clinical validation.

3.4.4 Clinical Validation with Real Samples

Clinical validation was conducted to demonstrate the practical applicability of the developed biosensor platform for quantifying sC5b-9 in real patient serum samples. A total of 11 patient samples were analyzed: eight samples from patients diagnosed with AChR+ MG, and three samples from patients positive for anti-MuSK antibodies (MuSK+ MG). For each clinical measurement, a freshly biofunctionalized biosensor chip was used to ensure consistent performance and avoid carry-over effects.

All serum samples were diluted 1:100 in PBST 0.5% + 25 mM CHAPS to reduce nonspecific binding and to stabilize the assay conditions. Prior to patient sample injections, a baseline was established by injecting 200 µL of similarly diluted commercial human serum (CHS, 1:100 dilution in PBST 0.5% + CHAPS) at a constant flow rate of 40 µL/min. Subsequently, a diluted serum sample from a healthy control (also 1:100 in PBST 0.5% + CHAPS) was injected as a negative control to confirm the absence of non-specific signal attributable to healthy serum components. After these control injections, patient serum samples (200 µL, diluted 1:100) were individually introduced under identical flow conditions (40 µL/min).

Post-injection, the biosensor surface was washed thoroughly with PBST 1% for 3 minutes at a reduced flow rate (20 µL/min) to remove unbound serum components and ensure a stable and specific sensor response. Each patient serum sample was initially evaluated using two technical replicates (dual spots on the biosensor chip) to confirm reproducibility of the measured signal. Following initial validation against the healthy control (n= 2 technical replicates), subsequent measurements were simplified by direct comparison of CHS baseline to the patient serum response.

The final sensor responses (Δλ, nm) were interpolated from previously generated calibration curves to determine sC5b-9 concentrations quantitatively. All data points were measured in triplicate (n= 3; technical replicates per condition) to enhance statistical reliability. Data analysis and graphical representation were conducted using GraphPad Prism, ensuring robust statistical interpretation and visualization of results.

3.4.5 Data Analysis and Curve Fitting

Raw spectra were processed using a developed Python script to separate channels and peak position. GraphPad Prism 10 (GraphPad Software Inc., USA) was used for further data processing and statistical analysis. The biosensor signal was expressed as the wavelength shift (Δλ, in nm).

Calibration curves were generated by plotting Δλ (mean ± standard deviation) versus the protein concentration. The data were fitted to a four-parameter logistic (4PL) regression model, described by the following parameters:

$$y = d + \frac{(a - d)}{[1 + \left(\frac{x}{c}\right)^{b}]}$$

a = the minimum value that can be obtained,

b = Hill's slope of the curve,

c = the point of inflection (represents the half-maximal inhibitory concentration IC50),

d = the maximum value that can be obtained.

The 4PL model was selected based on comparison with alternative models (5PL, one-site specific binding, exponential growth) using GraphPad's model comparison tool. In this model, y represents the biosensor response (Δλ, nm) and x the analyte concentration (ng/mL).

The limit of detection (LOD) was calculated using the formula:

$$LOD = 3.3\frac{\sigma}{S}$$

S = is the slope of the calibration curve,

σ = is the standard deviation of the response.

3.4.6 ELISA of sC5b-9

ELISA measurements were conducted according to the manufacturer's protocol provided with NOVUS Biologicals product manual for Human C5b-9 ELISA Kit (Colorimetric) (NBP266708). A standard curve was determined for the concentration of range of 31.25-2000 ng/mL in twofold serial dilutions. Optical density was measured using a microplate reader set to 450 nm.

CHAPTER 4 | RESULTS AND DISCUSSION

4.1 INTRODUCTION

The primary objective of this work is to develop and analytically validate a GC-LSPR biosensor for rapid, label-free detection of sC5b-9, a clinically relevant protein of complement activation in myasthenia gravis (AChR+ MG). The platform BD-derived polycarbonate nanogratings coated with a 68 nm Au film, an oriented Fc-capture layer (cys-Protein G/IgG) to preserve antibody activity, and a fixed-angle spectral readout that converts nanoscale binding events into robust wavelength shifts (Δλ, nm).

This chapter presents, step-by-step, the design optimization, biointerface engineering, and analytical performance of the sensor, then demonstrates its applicability in clinical matrices (serum). We first establish batch-to-batch reproducibility of the substrate fabrication, followed by microfluidic flow optimization. We then characterize the biofunctionalization conditions (pH and concentration) to maximize active antibody density and minimize nonspecific binding. Next, we quantify the bulk sensitivity, perform noise characterization (LoB/LoD) using standardized criteria, and construct calibration curves to translate spectral shifts into sC5b-9 concentrations. Finally, we assess matrix effects, regeneration, and run-to-run precision in serum.

These results support the low-cost, disc-derived GC-LSPR sensors being able to deliver sensitive, fast, and practical quantification of complement activity, providing a path toward diagnostic tools for MG.

4.2 DESIGN ITERATIONS

Initial testing of the single-channel chip architecture (**Figure 30**) revealed significant discrepancies in sensing performance between the two detection zones, prompting a design overhaul to a parallel-channel structure that significantly improved sensor performance and facilitated simultaneous dual measurements.



Figure 30. *First design of the nanoplasmonic chip with two sensing spots in one single microfluidic channel.*

In the original layout (**Figure 31**), both nanoplasmonic regions (“Zone 1” and “Zone 2”) resided in a single continuous microfluidic chamber, delivering the analyte in series.

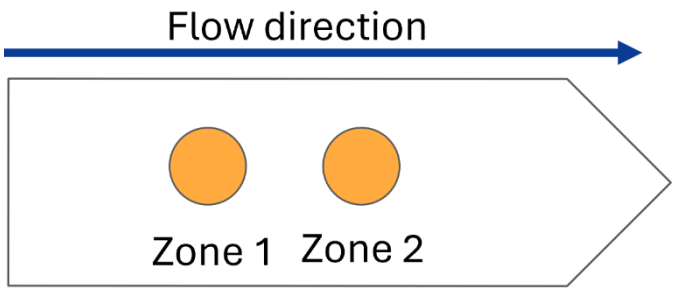


Figure 31. *Design of the sensing flow with continuous sensing spots ("Zone 1" and "Zone 2") in a single microfluidic channel.*

To quantify reproducibility, five independently fabricated and biofunctionalized chips were challenged with a model protein (IL-6) across a broad concentration range (0-10 000 ng/mL), and the accumulated wavelength shifts (Δλ, nm) were recorded (**Figure 32**). Although Zone 1 consistently produced tightly clustered response curves (mean Δλ at 4 000 ng/mL = 5.2 ± 0.1 nm), Zone 2 exhibited substantially greater variability (mean Δλ at 4,000 ng/mL = 5.8 ± 0.5 nm), indicating up to five-fold higher coefficient of variation.

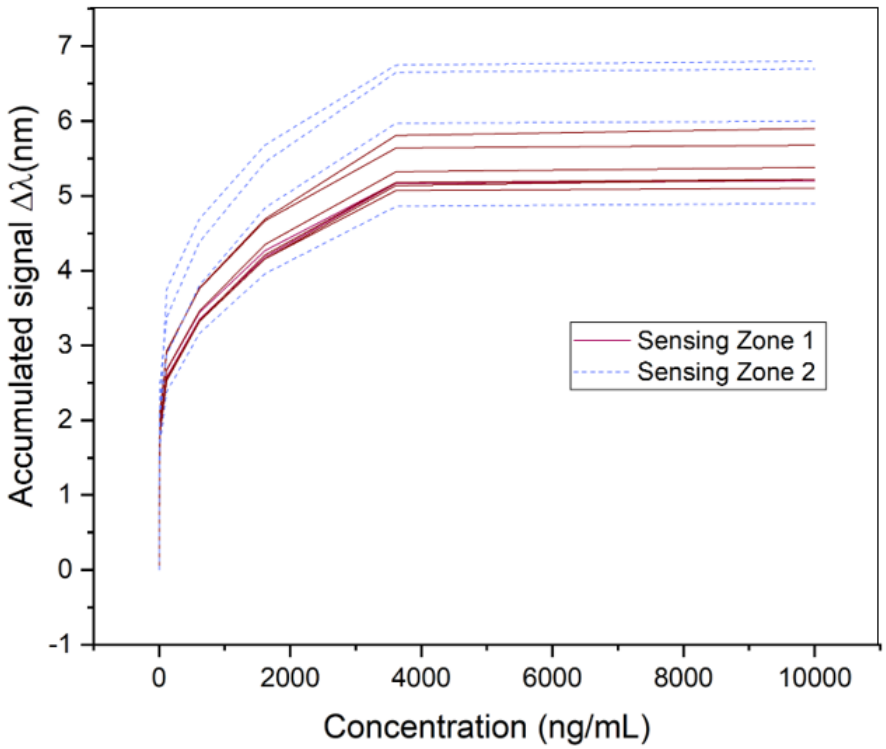


Figure 32. *Result from sensograms (n=5) measurement of concentration curve of IL-6.*

We hypothesized three potential contributors to this non-uniformity: (i) the laminar flow path inherently favors the upstream region (Zone 1), granting it first access to the analyte and potentially depleting downstream concentration; (ii) differences in the local evanescent-field decay length or surface roughness between zones; and (iii)

inconsistencies in substrate preparation, particularly protective-layer removal and gold deposition, which could magnify batch-to-batch variability.

These findings motivated the transition to a parallel-channel format (**Figure 24**), wherein each sensing spot receives the analyte simultaneously under identical hydrodynamic and surface conditions. By isolating the flow paths, we anticipated equal analyte availability and more consistent field conditions across both sensing spots. The parallel design not only harmonizes sensor responses but also enables true technical replicates in a single assay, thereby improving throughput and confidence in measured signals.

4.3 PROTECTIVE LAYER REMOVAL OPTIMIZATION

The layer removal process for the fabrication of the GC-LSPR chips was systematically optimized through three iterations (protocols v1.0, v2.0, and v3.0). The primary challenge during early protocols was incomplete removal of the reflective metallic and adhesive layers, which resulted in poor gold (Au) adhesion and dampened plasmonic responses. This was most evident in protocol v1.0, where residues from the protective polymer and reflective aluminum layer produced heterogeneous surfaces. SEM imaging confirmed significant roughness and debris, which directly affected the plasmon resonance peaks.

In the first fabrication iteration, thermal printable BDs (BD-R SL, Verbatim 43743) were cut into chips by CNC, and the reflective/protective layer was removed by immersing the pieces in 1 M HCl for 24 h at 40 °C, followed by 2 min ultrasonication in Milli-Q water and 2 min in ethanol.

To assess the surface quality, we visualized the sensors with two microscopy techniques: SEM inspection of the cleaned polycarbonate (PC) surfaces pre-Au deposition and post-Au deposition and with optical microscopy (OLYMPUS BX51RF).

The SEM images of the substrates prepared under the initial fabrication protocol (v1.0) provide unmistakable evidence of incomplete protective layer removal and surface contamination (**Figure 33**). Panels (a-c) depict the PC surface post-cleaning but pre-Au deposition. At low magnification (a, b), the surface appears heterogeneous, with irregular clusters and roughened domains that correspond to residual metallic alloy (Ag-based "MABL" layer) and incompletely removed protective coatings. At higher magnification (c), particulate debris and patchy regions are evident, obscuring the characteristic nanoslit pattern expected from BDs-derived gratings. This suggests that the chemical stripping (1 M HCl, 24 h at 40 °C) combined with brief sonication was insufficient to fully eliminate the reflective and adhesive layers, leading to an uneven exposure of the underlying PC nanostructure.

Following Au deposition, SEM inspection (d-f) shows that the nanoslit grating periodicity (320 nm pitch) becomes more apparent, confirming partial exposure of the substrate pattern. However, numerous bright contrast spots, corresponding to debris or Au agglomerates nucleating on contamination residues, remain visible across the surface. At higher magnification (e, f), these particulates disrupt the continuity of the Au thin film,

creating localized defects. Such discontinuities can compromise plasmon resonance by introducing scattering losses, reducing uniformity of the near-field enhancement, and thereby lowering sensitivity and reproducibility [81], [104].

Complementary optical microscopy (g-i) corroborates the SEM observations: while the Au-coated surface displays the expected golden hue, non-uniformities such as scratches, particulate debris, and dark irregular patches are visible. These defects indicate incomplete cleaning and poor film adhesion, which are likely to result in unstable baselines and increased sensor-to-sensor variability.

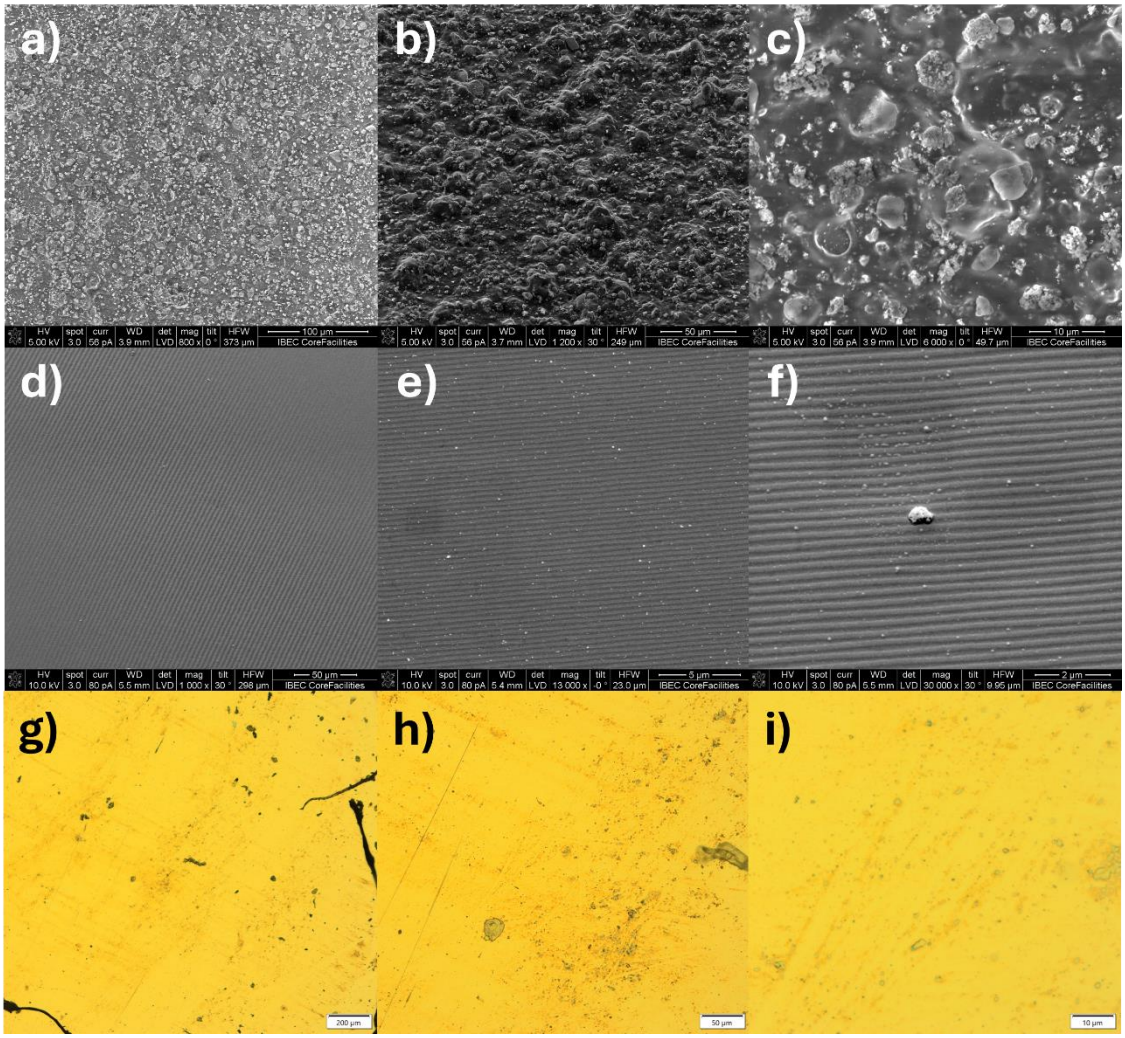


***Figure 33**. Panels (a-c) show SEM imaging of polycarbonate substrate after protective-layer removal using protocol v1.0 (1 M HCl, 24 h at 40 °C; brief sonication). Panels (d-f) show SEM imaging of sensors after Au film deposition (68 nm). Panels (g-i) show Au surface in microscopy. Scale bars as indicated.*

These results demonstrate that the first cleaning protocol was inadequate for preparing high-quality PC substrates for reproducible nanoplasmonic sensing. Although residual metal facilitated SEM visualization of the nanograting features, its presence undermines the fabrication process by impairing film adhesion and increasing optical noise. These findings highlight the critical importance of surface preparation in BD-derived

biosensors: even lesser amounts of residue at the nanoscale can have disproportionate effects on the continuity of thin metal films and on the plasmonic resonance quality factor, thereby degrading biosensor performance [66]. This motivated the development of subsequent, more rigorous cleaning strategies (protocols v2.0 and v3.0), which will be discussed in the following sections.

Nonetheless, to further evaluate the adhesion of the Au film layer to the PC substrate a simple qualitative test, known as the 'Scotch tape test,' was used [105,106]. The test consists in using a strip of adhesive tape and adhere firmly to the sensor, after removal of the tape, it indicates if the adhesion of the Au film was poor or limited. Minimal removal of the Au film was observed (**Figure 34**).



Figure 34. *Photograph of 'Scoth tape test' after the Au film deposition (68 nm) on PC substrate with cleaning protocol v1.0.*

To improve removal of the protective layer and Au deposition, we implemented a two-step acid stripping protocol: immersion in concentrated hydrochloric acid (37% HCl) for 1 h at 40 °C, followed by 1 M HCl for 48 h at 40 °C. SEM inspection confirmed a decrease in contaminants and label residues on the PC surface and a clearer exposure of the nanoslit grating. Ag-alloy/label residues observed with v1.0 are largely absent, overall roughness is reduced, and the nanoslit grating is clearly visible in **Figure 35** (panels a-c). Only sparse particulates remain, yielding surfaces suitable for uniform Au deposition and stable plasmonic response. Visually, chips showed cleaner, more uniform surfaces, which translated into more consistent Au deposition and improved batch-to-batch yield.

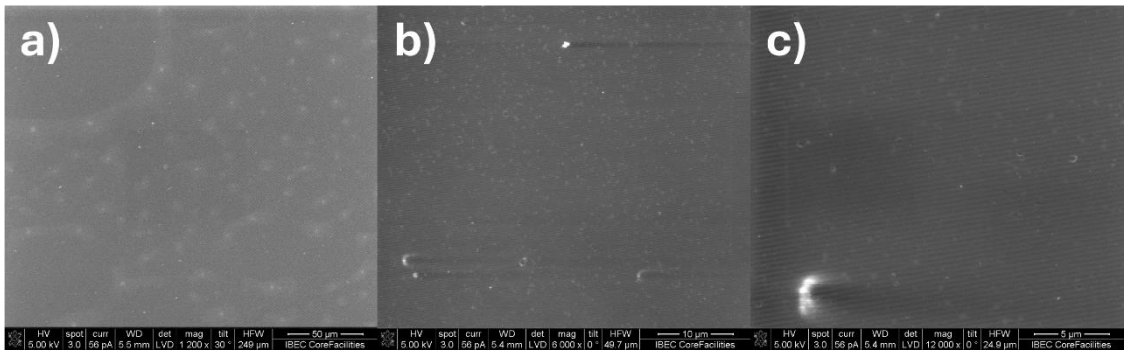


Figure 35*. Panels (a-c) show SEM imaging of Blu-ray-derived polycarbonate after improved protective-layer removal (protocol v2.0: 37% HCl, 1 h, 40 °C → 1 M HCl, 48 h, 40 °C; sequential ultrasonication in 20% acetic acid, water, 1% Hellmanex®, isopropanol; N_2 dry). Scale bars as indicated.*

Although the optimized protocol initially performed well, subsequent lots of the same BDs product introduced variability. After cleaning, several PC substrates exhibited surface roughness and residual label flaking, which compromised gold film continuity. The evaporated Au layer showed poor reflectivity and localized delamination, and the LSPR resonance could not be observed (**Figure 36**). These issues indicate that incoming substrate quality, rather than the cleaning protocol, was the limiting factor for reliable Au deposition and optical performance.

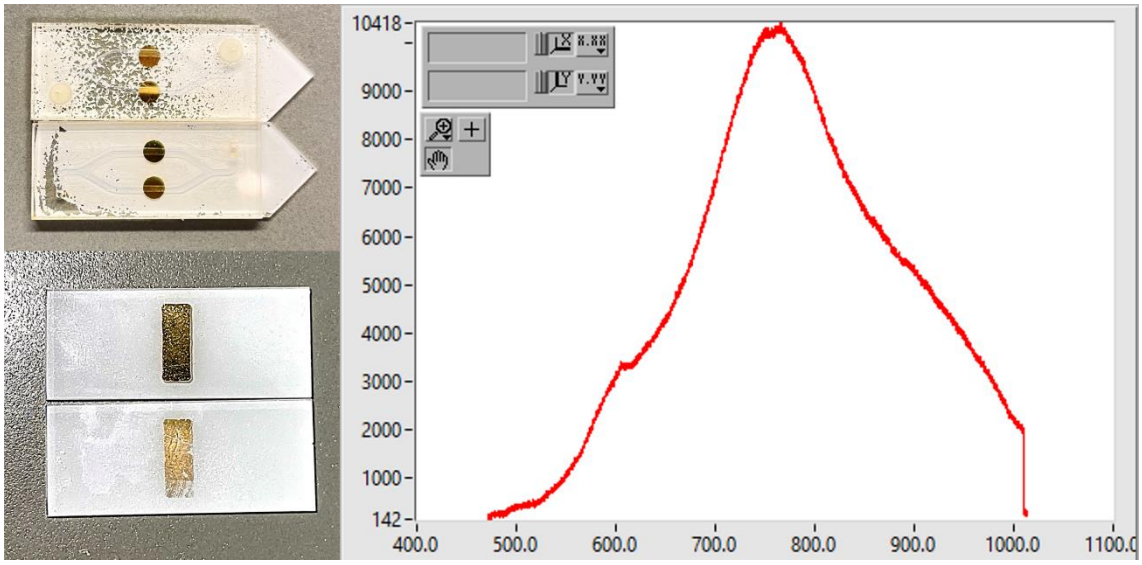


Figure 36. *Photographs of lot-dependent Au film failure and loss of plasmonic response. Left, top: assembled chip showing particulate contamination and label flaking. Left, bottom: two substrates after Au evaporation; the upper chip exhibits a rough, matte, non-uniform film, and the lower chip shows partial delamination—both incompatible with reliable optics. Right: reflected spectrum acquired under standard conditions; the trace lacks a distinct LSPR plasmon, consistent with poor coupling caused by the rough/flaking Au layer.*

The previously robust cleaning protocol began to fail when a new lot of discs, ordered under the same catalog number (Verbatim 43743), arrived with “DL” (double-layer) labeling instead of “SL” (single-layer). This lot change altered the substrate and, consequently, its response to acid stripping. Double-layer BDs incorporate additional recording/reflective layers and protective coating; these extra layers increase chemical and mechanical resistance, making the HCl-based removal less effective and leaving a rough, porous PC surface after treatment (**Figure 37**).

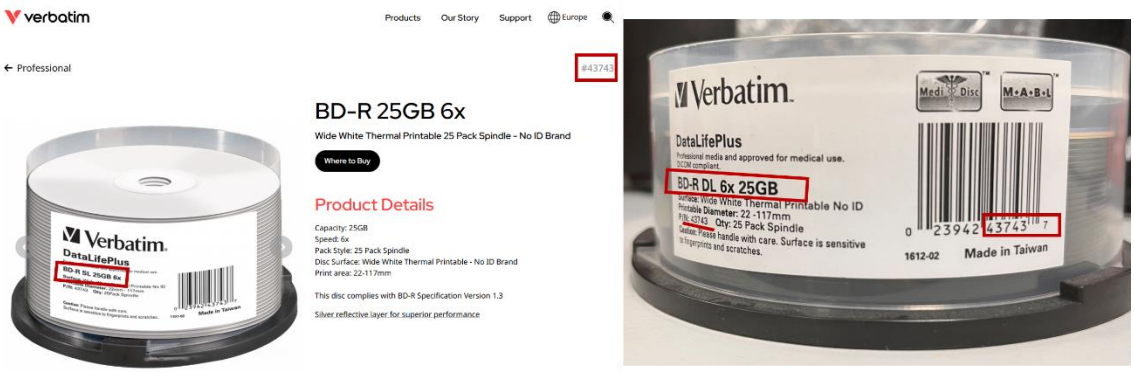


Figure 37*. Catalog consistency issue and lot effects on substrate quality. Left: example listing for Verbatim BD-R SL 6 x 25 GB (cat. 43743) "Wide White Thermal Printable, no ID." Right: packaging from the received lot labeled BD-R DL 6 x 25 GB but bearing the same catalog number (43743). The DL construction adds extra functional and protective layers that hinder complete removal by the established acid protocol and, together with label flaking, lead to roughened PC surfaces and poor Au deposition.*

By repeating the 'scotch test' on the sensors we could observe the adhesion of the Au was not optimal and was easily removed by it (**Figure 38**).



Figure 38. *Photograph of 'Scoth tape test' after the Au film deposition (68 nm) on PC substrate with cleaning protocol v2.0 in BD-R DL derived substrates.*

The printable label formulation of the new lot exhibited poor adhesion and flaked during processing, introducing particulates that further degraded gold film continuity. Together, the added multilayer stack and label flaking explain the loss of mirror-like Au, diminished optical quality, and failure to observe a distinct plasmon resonance (**Figure 39**).

The introduction of BD-R DL discs under the same catalog number as the previously used BD-R SL substrates highlighted a critical issue in material sourcing for reproducible fabrication. As shown in **Figure 39** (panels a-c), SEM inspection of the DL substrates after protocol v2.0 cleaning revealed large circular domains, microcracks, and extensive residual debris. These features likely arise from incomplete dissolution of the reflective and adhesive layers, which in DL discs are thicker and chemically more resistant than in SL constructions [81]. The persistence of these multilayers produced a roughened and porous polycarbonate (PC) surface, compromising the nanoslit visibility and making it unsuitable for uniform Au depositions.

Following Au evaporation (panels d-f), the films exhibited discontinuities and poor adhesion, confirmed by the "Scotch tape test," which stripped off the Au layer with minimal force. This points to insufficient chemical activation of the PC substrate, combined with contamination by insoluble residues and label fragments, which disrupted the polymer-metal interface. Importantly, such discontinuities not only reduce film conductivity and optical quality but also broaden the plasmon resonance peak, thereby lowering sensor sensitivity [107,108].

The printable labeling of the DL lot further exacerbated the issue. As seen in optical images (panels g-i), label flaking and embedded particulates generated non-uniform regions across the chip, leading to inhomogeneous reflectivity. Label formulations are typically based on UV-cured resins or thermosetting adhesives, which resist HCl etching and can detach in fragments during cleaning, scattering across the surface. These particulates hinder Au continuity, create uncontrolled scattering centers, and further diminish reproducibility.

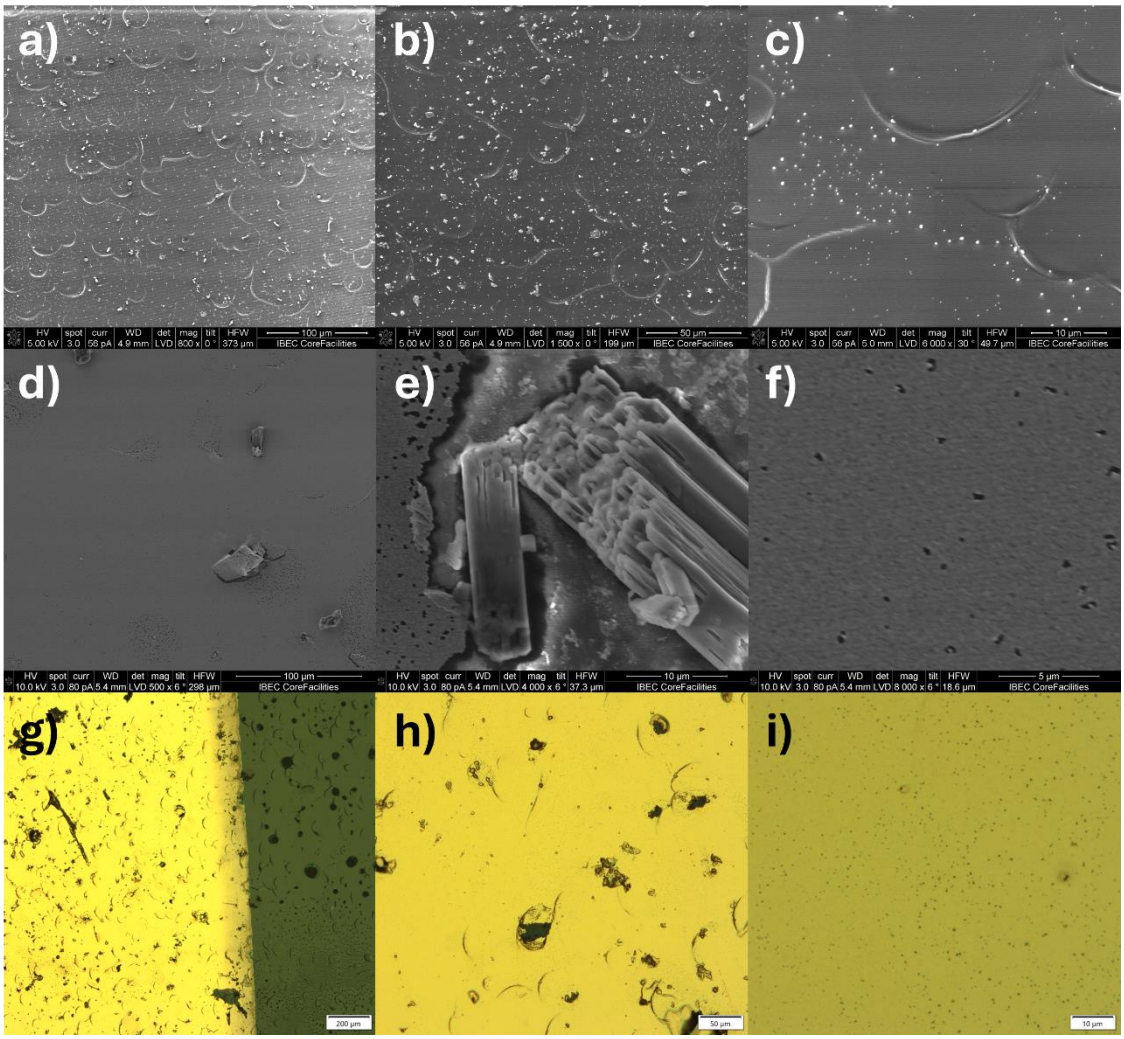


Figure 39. *Panels (a-c) show SEM imaging of polycarbonate substrate after protective-layer removal using protocol v2.0 (37% HCl, 1 h, 40 °C → 1 M HCl, 48 h, 40 °C; sequential ultrasonication in 20% acetic acid, water, 1% Hellmanex®, isopropanol; N_2*

dry). Panels (d-f) show SEM imaging of sensors after Au film deposition (68 nm). Panels (g-i) show Au surface in microscopy. Scale bars as indicated.

To eliminate label flaking and standardize the process, we screened several BDs and identified BD-R single-layer (SL), Verbatim 43742 as the most consistent for PC quality and Au adhesion, for future reference non-printable recordable discs work better than the printable line. However, applying the harsher protocol v2.0 (37% HCl, 1 h → 1 M HCl, 48 h; 40 °C) to this SL disc was overly abrasive, producing shallow pitting and surface roughness on the PC that translated into non-uniform Au films and damped/ill-defined plasmon peaks (**Figure 40**).

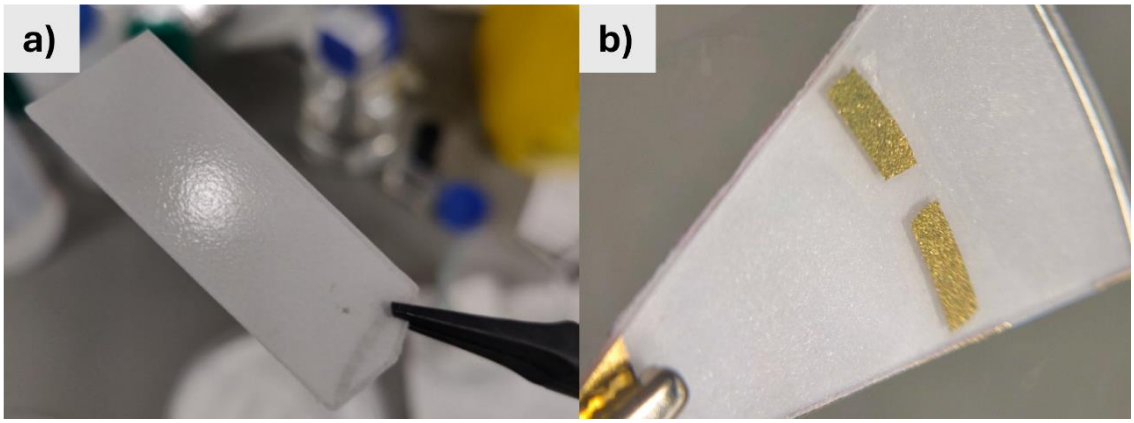


***Figure 40**. Cleaning protocol v2.0 applied to BD-R SL (Verbatim 43742). Left: PC substrate after stripping shows micro-roughness/pitting. Right: Au-coated chips also have roughness/pitting.*

We therefore introduced a gentler protocol v3.0 (0.75 M HCl for 24 h at 40 °C as described in the materials and methods section) which yielded smooth PC surfaces, clean exposure of the nanoslit grating, mirror-like Au films, and a stronger, well-defined LSPR resonance. SEM and optical microscopy confirmed the improved morphology, and the reflectance spectra showed higher peak intensity and signal-to-noise. Protocol v3.0 was adopted as the standard for all subsequent chip batches (**Figure 41**).

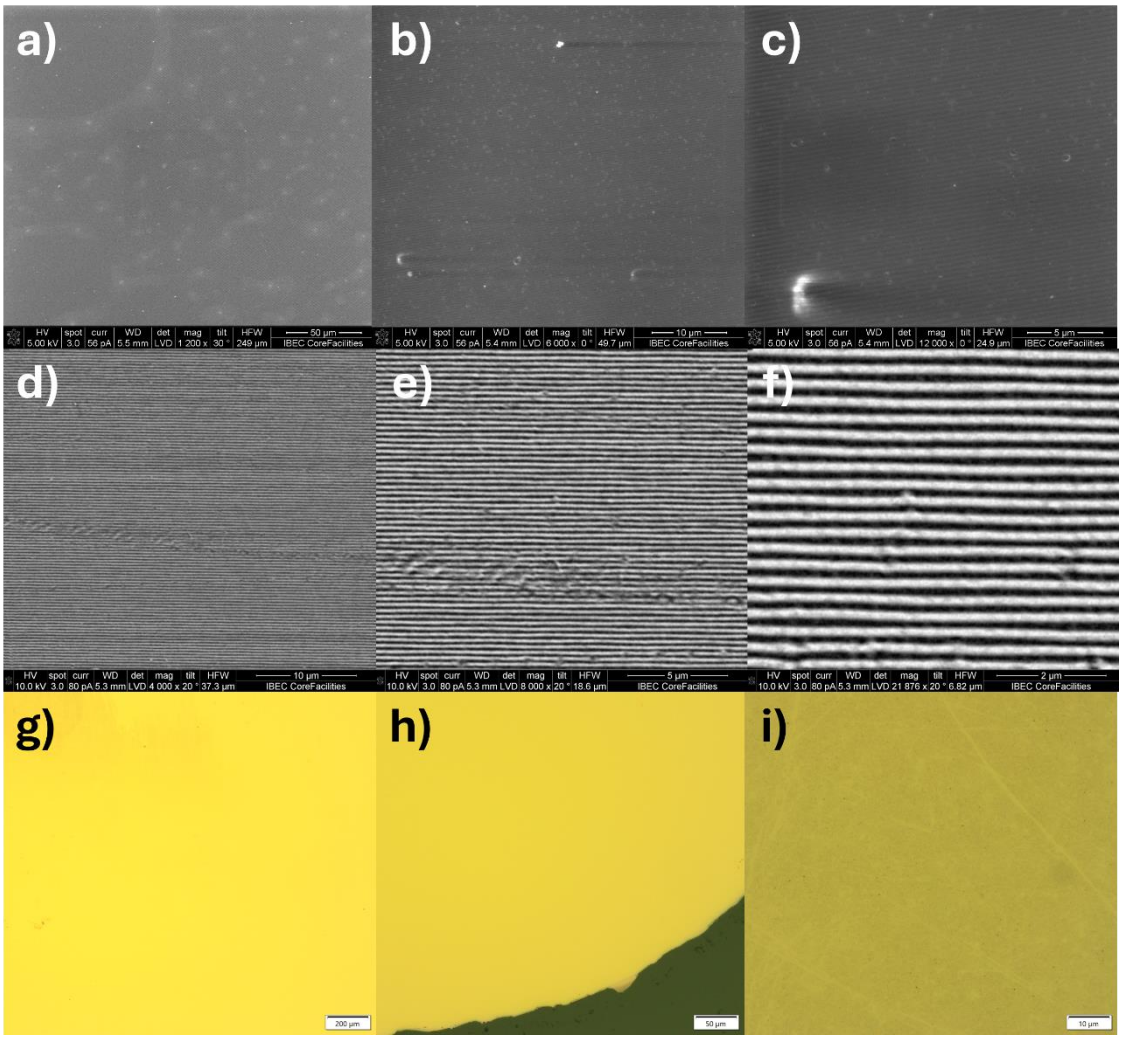


Figure 41. *Panels (a-c) show SEM imaging of polycarbonate substrate after protective-layer removal using protocol v3.0 (0.75 M HCl for 24 h at 40 °C; sequential ultrasonication in 20% acetic acid, water, 1% Hellmanex®, isopropanol; N_2 dry). Panels (d-f) show SEM imaging of sensor after Au film deposition (68 nm). Panels (g-i) show Au surface in microscopy. Scale bars as indicated.*

The introduction of protocol v3.0 (0.75 M HCl, 24 h, 40 °C) provided a decisive improvement in surface quality and sensor reproducibility. SEM inspection of the polycarbonate (PC) substrate revealed smooth surfaces with minimal debris, in contrast to the roughened, porous morphologies observed in earlier iterations (protocols v1.0 and v2.0). The nanoslit gratings were cleanly exposed (panels d-f), with well-defined periodicity and reduced contamination, which is critical for achieving reproducible plasmon coupling. Optical microscopy (panels g-i) confirmed the formation of a uniform, mirror-like Au coating, free from pitting or discontinuities, indicative of improved adhesion between the metal film and the PC template.

This improvement can be due to two key mechanisms. First, reducing the acid concentration from 1 M to 0.75 M minimized polymer surface damage while still effectively dissolving the metallic reflective layer. This balance preserved the nanoslit

fidelity, avoiding the shallow pitting observed with harsher conditions, which otherwise function as scattering centers and dampen plasmon resonances [81]. Second, the sequential multi-step cleaning (acetic acid → water → Hellmanex® → isopropanol) ensured efficient removal of organic residues and label particulates, both of which previously contributed to poor Au continuity.

We were able to characterize the nanogratings as observed in **Figure 42** with ImageJ image processing. The periodicity is around 320 nm, constant with the manufacturer's track pitch, proving that we did not lose the characteristic periodic nanograting from BDs. The periodic gratings enable the resonant coupling between light and surface plasmon through diffraction-mediated phase matching, which controls the resonance wavelength, linewidth, and near-field strength for sensing [66].

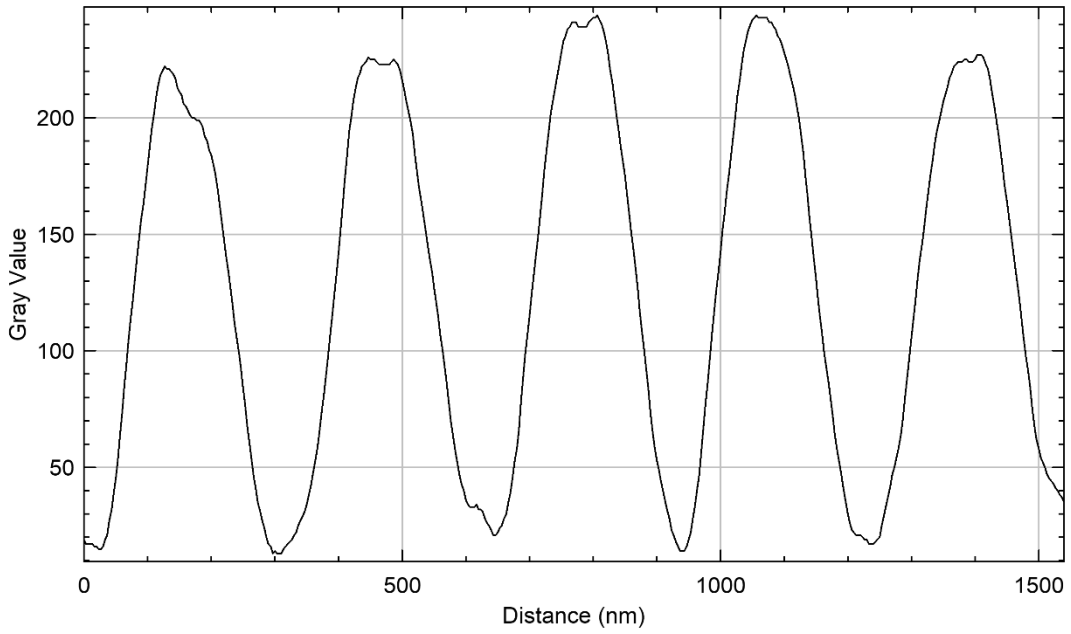


Figure 42. *Periodicity (P=320 nm) calculated from the SEM imaging of the nanoslits.*

The impact of these improvements was also evident in the optical response. Sensors fabricated with protocol v3.0 consistently display sharper, higher-intensity LSPR peaks with lower baseline noise, resulting in morphological uniformity and the smooth, continuous Au film that reduces plasmon damping and promotes coherent electron oscillations across the grating [109], thereby enhancing sensitivity. **Figure 43** summarizes the three different protocols and their impact on substrate and optical performance.

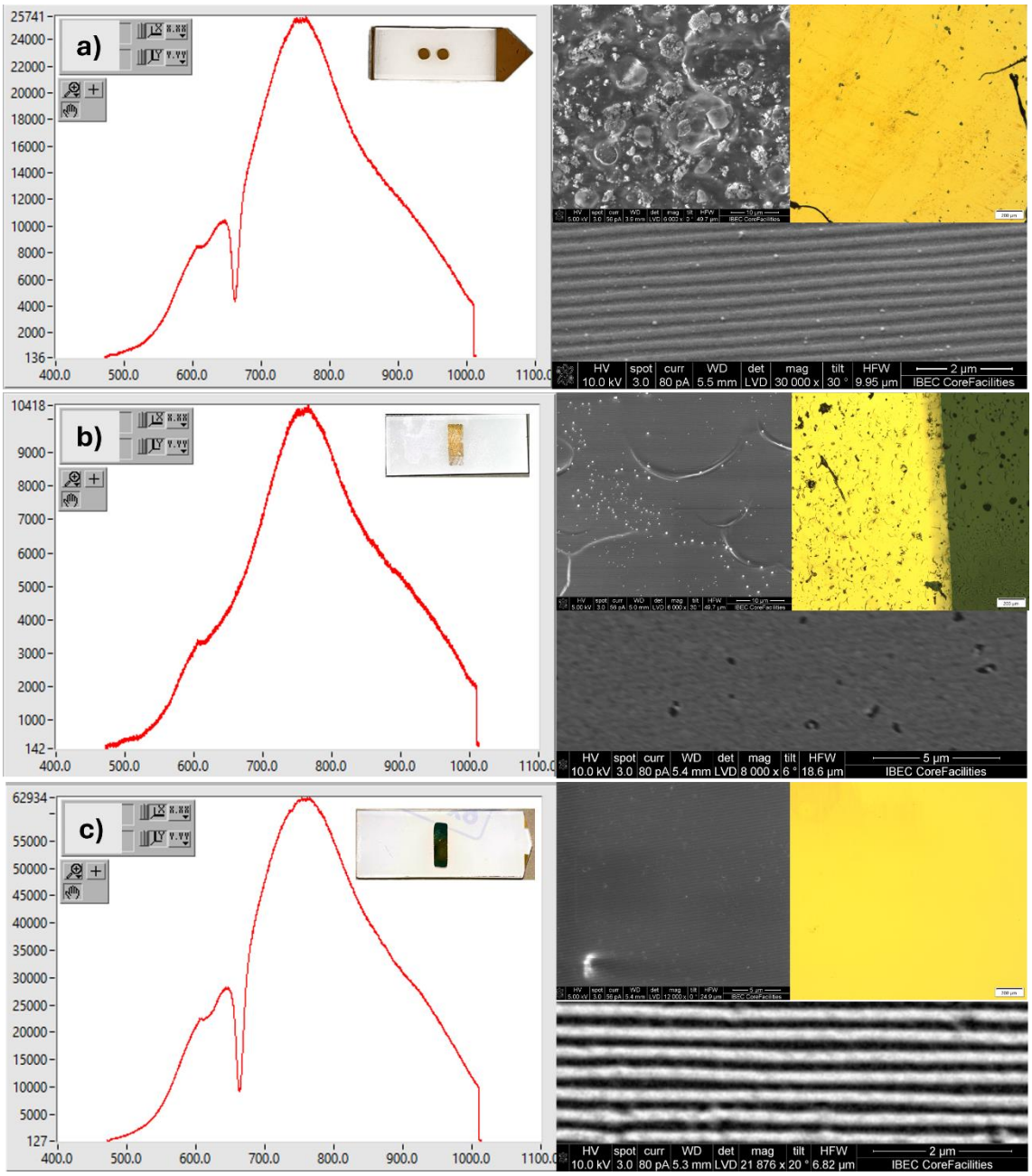


Figure 43. *Comparative characterization of three cleaning protocols and their impact on substrate and optical performance.* ***(a)*** *Protocol v1.0 (1 M HCl, 24 h, 40 °C) on printable BD-R SL (cat. 43743): lower LSPR reflectance peak; SEM (PC pre-Au) shows Ag-alloy/label residues; SEM (post-Au) shows roughness and particles; Microscopy shows scratches on the gold surface and debris.* ***(b)*** *Protocol v2.0 (37% HCl, 1 h → 1 M HCl, 48 h; 40 °C) on BD-R DL (43743): reflectance peak is not present; SEM (PC pre-Au) shows over-etched texture; SEM (post-Au) shows roughness, not clear deposition; Microscopy shows damaged surface and indicates poor film quality.* ***(c)*** *Protocol v3.0 (0.75 M HCl, 24 h, 40 °C) on BD-R SL (43742): strong, well-defined LSPR reflectance peak; SEM (PC pre-Au) shows clean nanoslit grating with minimal debris; SEM (post-Au) shows smooth, continuous film; Microscopy uniform, mirror-like Au. Scale bars as indicated.*

To further evaluate the adhesion of the Au film layer we repeated the 'Scotch tape test, and no removal of the Au film was observed. Compared to the other protocols, this new iteration of the sensors produced a robust Au film that resisted delamination. This improvement is critical, as delamination can alter the dielectric interface and cause resonance instability or loss of signal (**Figure 44**).

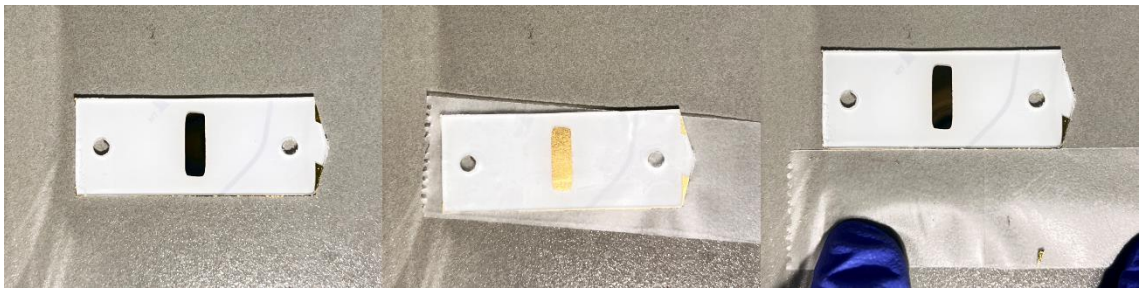


Figure 44. *Photograph of 'Scoth tape test' after the Au film deposition (68 nm).*

The absence of sharp resonance in protocols v1.0 and v2.0 sensors accentuates the inability of partially cleaned substrates to support stable plasmon peaks. By contrast, protocol v3.0 with an improved multilayer removal exhibited strong, well-defined plasmon peaks, validating the relation between surface preparation and optical performance.

Notably, adopting v3.0 standardized the fabrication workflow, enabling reliable batch-to-batch reproducibility. This was previously compromised by the variable response of BD-R DL substrates (protocol v2.0) and the incomplete protective layer removal in v1.0. Literature on DVD- and BD-derived plasmonic gratings confirms that optimized chemical etching is critical for ensuring structural fidelity and reproducibility, with small deviations in cleaning parameters leading to significant optical variability [110]. By aligning with these best practices, protocol v3.0 positions the platform for robust and scalable biosensor fabrication.

Another relevant finding was the unexpected variation between BDs batches. It is important to carefully source and screen all new disc batches to implement standard sensor quality. The improvements achieved with protocol v3.0 fabrication directly translated into enhanced analytical performance. Clean and uniform nanograting enabled sharp resonance peaks, which allow detection of smaller RI changes. Substrate optimization is a great factor for sensitivity, reproducibility, and LOD in biosensing.

Overall, the optimization of fabrication protocols demonstrates that BD-derived gratings, when properly processed, can yield reproducible and high-quality nanoplasmonic chips.

4.4 BATCH-TO-BATCH REPRODUCIBILITY EVALUATION

After the optimization of the substrate cleaning, we wanted to assess if we had achieved reproducibility between batch-to-batch fabrication for producing a dependable nanoplasmonic chip as it is important to achieve high-throughput GC-LSPR sensors that

offer dependable biosensing. We measured n= 9 sensors (three per batch; identical 68 nm Au evaporation) in Mili-Q water to obtain the spectra as shown in **Figure 45**.

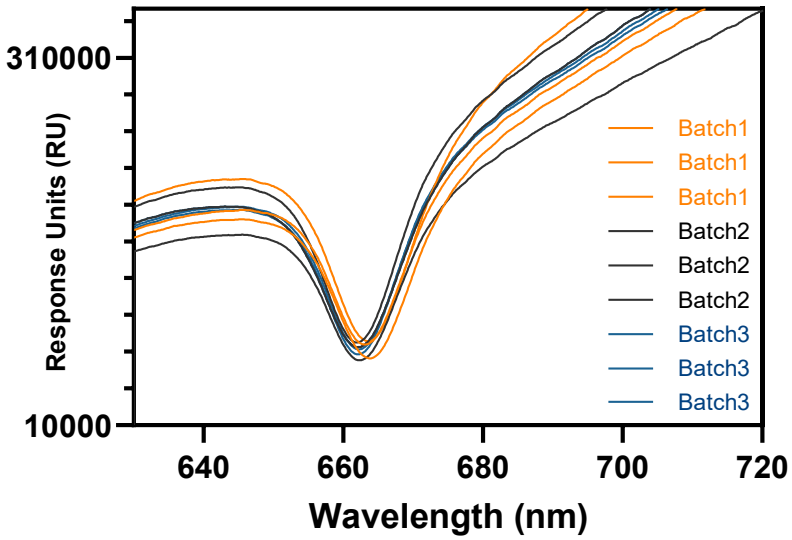


***Figure 45**. Reproducibility evaluation of the fabrication process. Sensograms of n=9 different sensors with a 68 nm Au layer from three different fabrication batches.*

The overlaid spectra show nearly coincident lines; after normalizing the data to the maximum, the sensor spread in λ (nm) we found was σ± 0.06 nm, indicating spectral consistency. The sensor spread can be due to temperature on the surface generated by the fiber-optic light source probe, as it can shift the wavelength to the order of 0.13 nm per degree Kelvin [111]. This drift is expected, since the RI of the liquids will change more sensitively with temperature; we have a temperature sensor set up to monitor thermal condition and ensure that the spread is due fabrication rather than to environment conditions.

It is important to achieve robust fabrication because in GC-LSPR sensors and thin Au film deposition, slight changes in Au thickness and surface roughness can shift the λ (nm), broaden the dip, and reduce signal-to-noise and sensitivity. Literature shows that Au thickness strongly influences LSPR spectra and coupling efficiency, while increased roughness adds damping that broadens or shallows the resonance, degrading the LOD [112].

Batch to batch reproducibility is key when producing plasmonic chips, as it keeps the resonance wave where you would expect it, lowering uncertainty and making results comparable [113]. Small fabrication drifts (e.g., gold thickness, roughness from the substrate surface) can influence the resonance wavelength and directly impact the sensitivity and LOD. Our sensor indicated reproducible fabrication, which allowed us to continue with confidence that batch effects would not dominate our biosensing results.

4.5 MICROFLUIDIC SYSTEM

Microfluidic integration is a critical part of nanoplasmonic sensors, as it not only accelerates assay times and enhances overall sensitivity by maintaining a steady, controlled flow of analyte across the sensing surface, but also ensures efficient delivery and rapid exchange of sample to and from the active regions. In our initial configuration (**Figure 46**), we employed a single continuous microfluidic channel of 1 mm width formed by double-sided adhesive tape, the height of the channel being the thickness of the double-sided tape (140 µm), which greatly simplified device assembly but introduced two key challenges: suboptimal flow uniformity in corner regions and a heightened risk of bubble entrapment. Computational fluid dynamics simulations in COMSOL revealed that, upon navigating 90° turns of the inlet/outlet, the flow velocity decreased markedly, creating low shear "dead zones" prone to air pocket formation. These stagnant regions can compromise measurement reproducibility and even block the optical path.

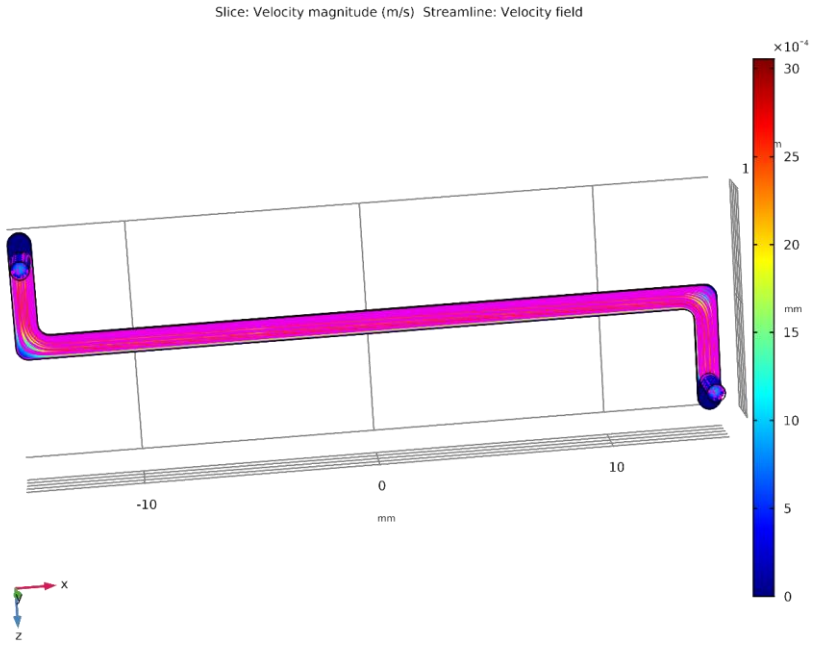


Figure 46. *COMSOL velocity magnitude (m/s) and streamline profile: velocity field of the single channel microfluidic design.*

A second consideration was the mechanical integrity of the bond between the polycarbonate (PC) sensor substrate and the adhesive microfluidic layer. Residual surface contaminants on the PC-typically remnants of the protective BDs layers-impaired adhesion, leading to delamination under flow and further exacerbating bubble issues or leakage. By introducing a rigorous, multistep cleaning regimen (described in Section 3.2.3) we achieved a hydrophilic, contaminant-free PC surface that forms a robust, leak-proof seal with the tape.

To solve these issues, we redesigned the microfluidics to a parallel-channel layout with rounded corners. This design not only maintains high-velocity flow throughout the network, minimizing stagnant zones, but also delivers simultaneous, identical analyte

streams to each sensing spot, thereby reducing variability and bubble formation without sacrificing the simplicity of double-tape fabrication.

To enable true technical replicates and eliminate the flow issues observed in our initial single-channel design, we developed a series of parallel-channel microfluidic geometries that split the incoming sample into two identical streams. Each branch was maintained at a constant width of 1 mm, but the splitting angle was varied systematically, 40°, 60°, and 90°, to identify the configuration that would preserve uniform flow velocity and minimize recirculation zones.

COMSOL Multiphysics simulations of the velocity magnitude and streamlines revealed distinct differences among these geometries (**Figure 47**). At a shallow 40° split (**Figure 47A**), the flow paths remained close together, causing slight interference between branches and minor low-velocity regions near the bifurcation. A right-angled 90° split (**Figure 47B**) produced pronounced stagnation zones at the turn, with streamlines decelerating abruptly and increasing the risk of bubble entrapment. In contrast, the 60° split (**Figure 47C**) delivered smooth, symmetric flow division: both branches maintained nearly identical velocity profiles (peak velocity ~3.2×10^{-2} m/s) and exhibited minimal recirculation at the junction.

Then, we evaluated an optimized 60° design that incorporated an expanded sensing chamber of 3 mm in diameter to match the diameter of the optical light source spot, thereby maximizing the active sensing area and increasing the amount of plasmonic signal collected from each channel (**Figure 47D**).

This modification eliminated the remaining corner vortices and produced the most uniform velocity distribution across both sensing branches but could not be used as having the inlet/outlet in a single line made the connecting microfluidic tubing get in the way of the light beam.

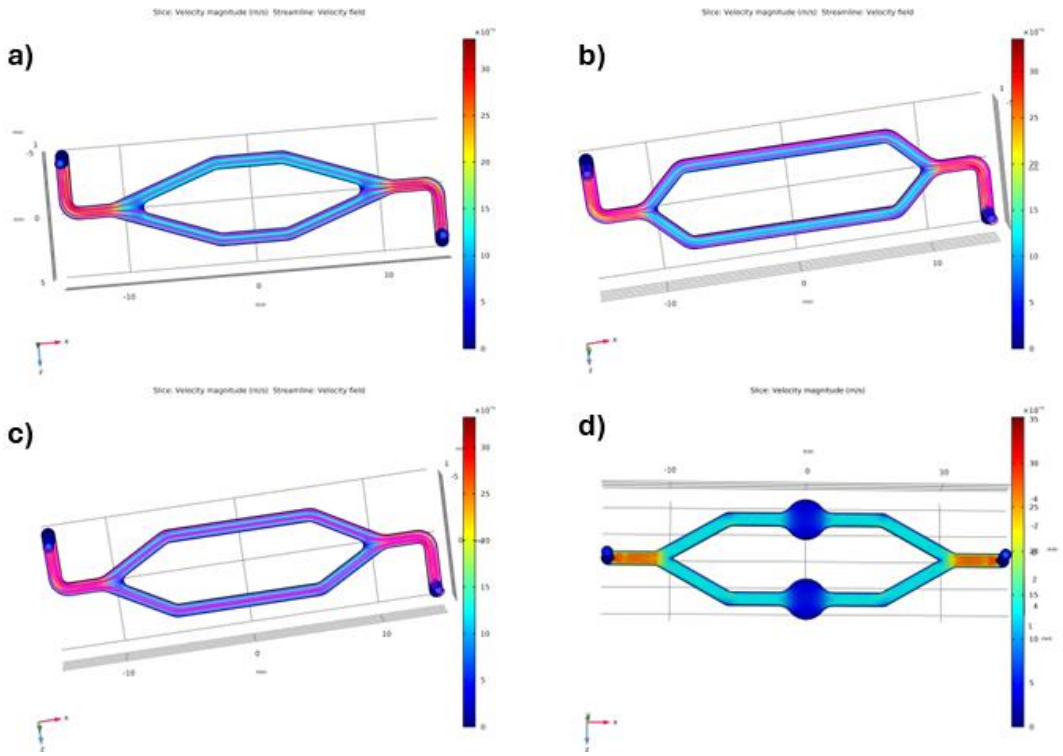


Figure 47. *COMSOL velocity magnitude (m/s) and streamline profile. A) 1 mm parallel-channel split at 40º, b) 1 mm parallel-channel split at 90º, c) 1 mm parallel-channel split at 60 º, d) 1 mm parallel-channel split at 60º with straight channel for inlet/outlet.*

Based on these results, the 60° parallel-channel geometry with bent inlet/outlet transitions, and the incorporated sensing chamber of 3 mm diameter was selected for fabrication, ensuring reproducible analyte delivery to each sensing spot, reducing dead volumes, and minimizing bubble formation.

To verify uniform flow through both channels and across the enlarged sensing zones, we extracted velocity-field profiles at three critical cross-sections (**Figure 48**). At the inlet (**Figure 48A**), the velocity magnitude remains nearly constant (2.6 mm/s) across the full width of the channel, confirming a stable entry flow. Within the parallel branches (**Figure 48B**), each 1 mm channel maintains a uniform velocity of approximately 1.3 mm/s, demonstrating symmetric splitting with minimal imbalance. Finally, across the sensing chamber itself (**Figure 48C**), the velocity profile remains centered and nearly identical in each branch (0.5 mm/s), ensuring homogeneous analyte exposure beneath the optical spot.

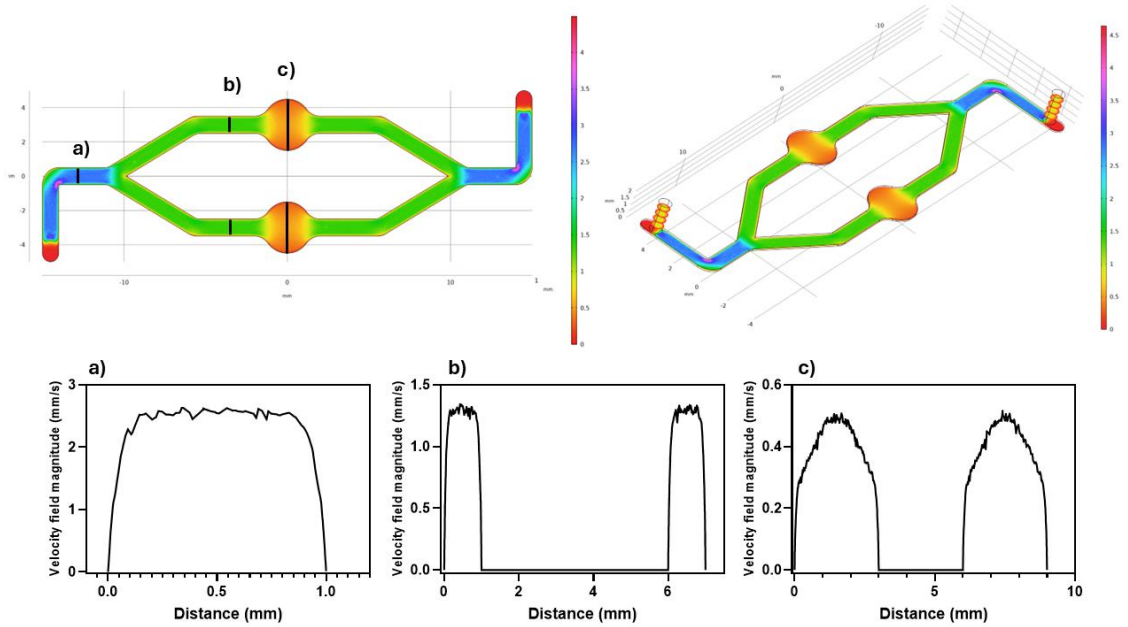


Figure 48. *Velocity field magnitude (mm/s) of the cross-sections. A) The velocity field at the inlet, b) the velocity field of both channels, c) the velocity field of the sensing chamber.*

These COMSOL Multiphysics simulations confirm that the final microfluidic geometry promotes stable laminar flow, minimizes dead volumes, and delivers reproducible analyte distribution to every sensing region; key prerequisites for high-precision, dual-channel nanoplasmonic measurements. At the typical assay flow rates used in this work (e.g., 40 µL/min), the redesigned 1 mm x 140 µm with 60º parallel-channel with a 3 mm sensing chamber operates in a laminar, shear-assisted regime that supports uniform mass transport, minimizing bubble formation, and enables true replicates.

4.6 SENSING PLATFORM SETUP

The first benchtop platform assembled in the Biosensors for Bioengineering lab comprised a low-flow peristaltic pump (LabV1), a fixed-angle opto-mechanical stage, a broadband halogen source, and a fiber-coupled spectrophotometer (BW-Spec). Samples were introduced manually at the chip inlet; effluent was routed to waste (**Figure 49**). Spectra were collected at user-defined timepoints with the BW-Spec software and exported for analysis in Origin 8.0. While this setup enabled monitoring of LSPR peak shifts (Δλ), it suffered from three limitations: (i) discrete, operator-timed measurements that hindered continuous kinetic tracking; (ii) pulsatile flow from the peristaltic pump, which added baseline ripple and increased noise during injections; and (iii) lack of synchronization between fluidic events (injection/wash) and spectral acquisition, making the assay user-dependent and prone to timing errors.

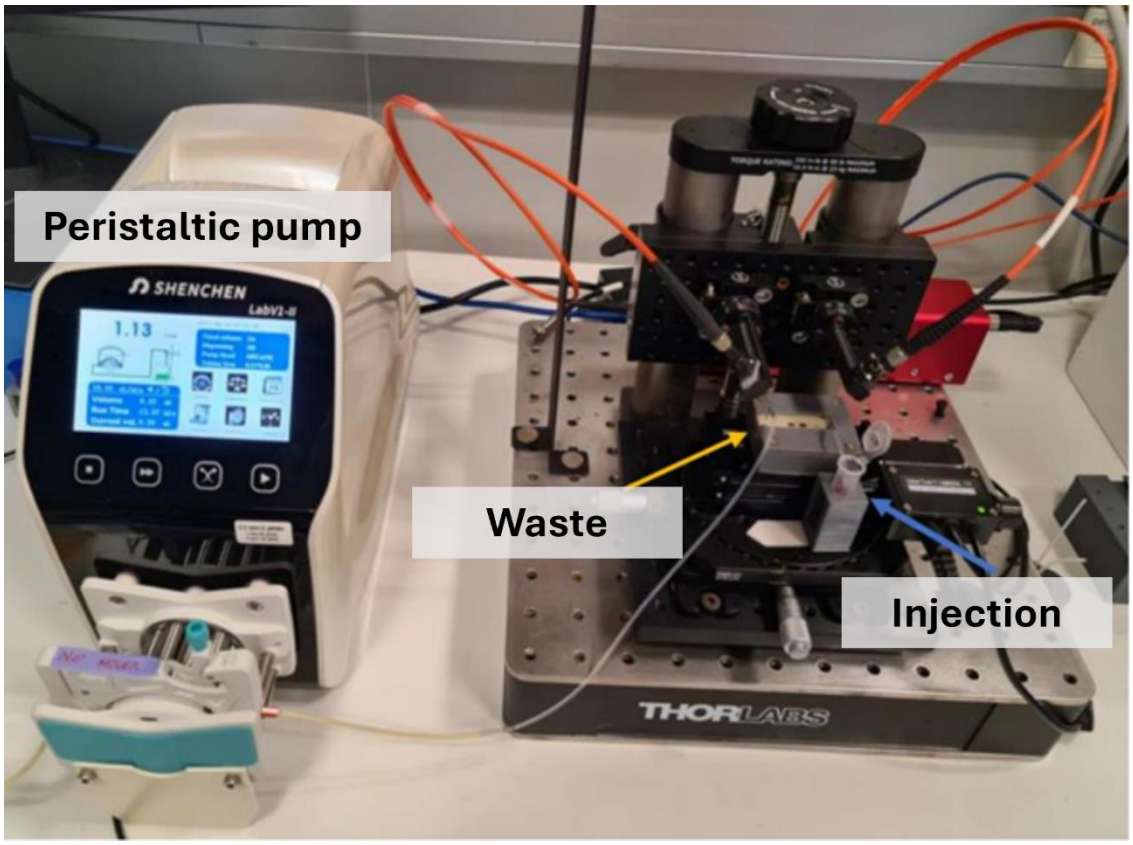


***Figure 49**. Photograph of the initial sensing platform (v1). Left: low-flow peristaltic pump (LabV1). Right: fixed-angle opto-mechanical stage with chip holder; labeled "Injection" indicates the sample inlet; "Waste" indicates the outlet. In this configuration, spectra were acquired at discrete timepoints via BW-Spec software, which allowed Δλ tracking but not continuous, synchronized, real-time acquisition.*

To achieve true real-time sensing with synchronized fluidics and optics, the platform was subsequently reconfigured as seen in **Figure 50** (see Materials and Methods section for more detailed information): a syringe-pump/6-port valve fluidic path with a bubble trap replaced the peristaltic flow, an Avantes NEXOS spectrometer provided continuous spectra at fixed angle, and custom LabVIEW software handled live peak tracking, baseline correction, and event logging. This upgrade reduced user bias, improved signal-to-noise, and enabled kinetic analyses (association/dissociation) and automated data archiving.



Figure 50. *Photograph of the real-time sensing platform (v2). In this configuration, spectra were acquired via LabVIEW software, which allowed Δλ tracking real-time acquisition.*

4.7 BULK CALIBRATION

To verify plasmonic behavior and quantify the bulk refractive-index (RI) sensitivity of the unfunctionalized nanoslit grating, we performed a bulk calibration (Section 3.2.11). The assembled chip was mounted on the fixed-angle platform and equilibrated with Milli-Q water (baseline). Aliquots of hydrochloric acid (HCl) solutions of known RI (**Table 6**) were then injected in decreasing concentration, with water washes between steps to avoid carry-over. For each injection, spectra were acquired continuously, and the resonance wavelength (Δλ, nm) was extracted. The real-time sensogram (left panel) shows discrete, stable plateaus for each solution, and the corresponding spectra (right panel) exhibits wavelength shift with increasing RI (**Figure 51**).

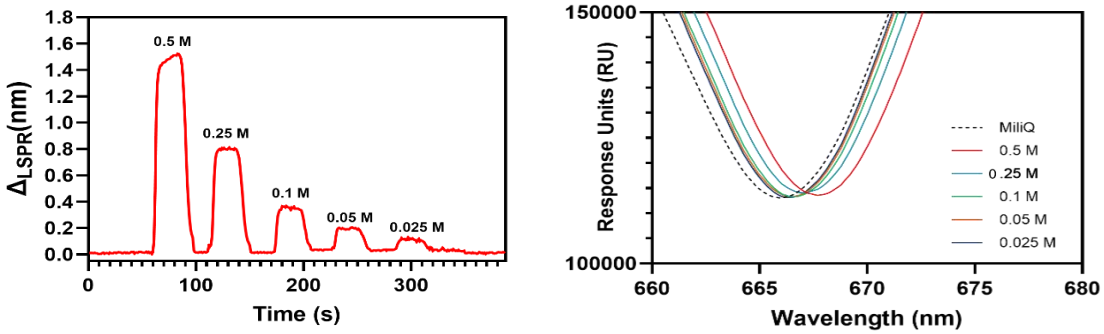


Figure 51. *Bulk calibration sensogram. (a) Real-time measurement of wavelength shifts (Δλ, nm) caused by subsequent injections of decreasing HCl concentrations in time (s). (b) wavelength displacement shifts (Δλ, nm) of decreasing HCl concentrations.*

To assess the bulk sensitivity (S_B), which is defined as the shift in resonance peak caused by the change in refractive index (RI) of the dielectric medium of the sensor surface, we measured and plotted the LSPR wavelength shift displacement (Δλ, nm) as a function of the RI changes employing MiliQ water as the running buffer and reference RI ($\eta_0 = 1.3325$). By fitting the data to a linear regression, we obtained a calibration curve (**Figure 52**).

$$\Delta\lambda = S_B * \Delta n + b$$

Table 6. *Refractive index (RI) of HCl solutions used for bulk calibration (reference $\eta_0 = 1.3325$).*

Solution	RI (n)	Δn (RIU)
0.5 M HCl	1.3368	0.0043
0.25 M HCl	1.3346	0.0021
0.1 M HCl	1.3334	0.0009
0.05 M HCl	1.3331	0.0006
0.025 M HCl	1.3330	0.0005

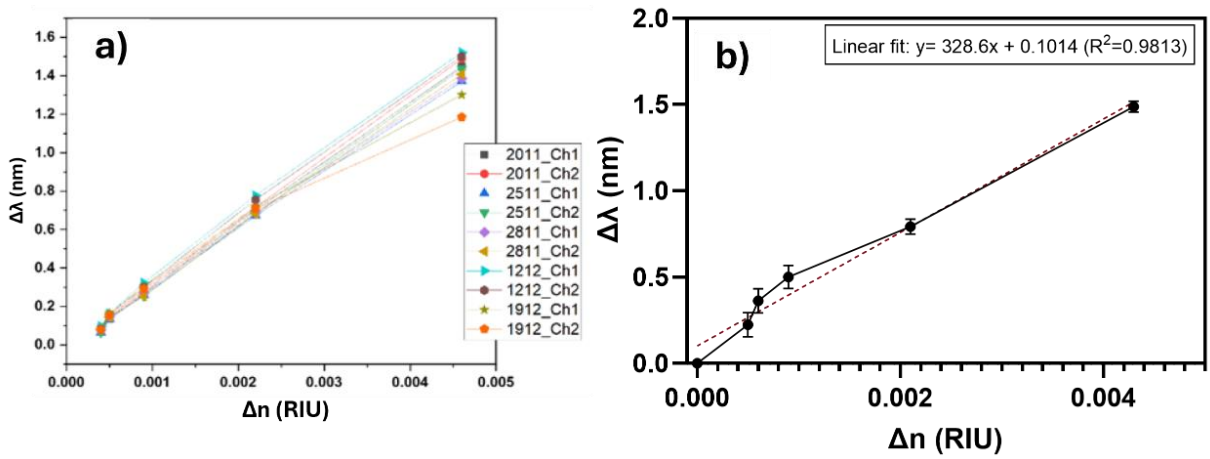


Figure 52*. Bulk sensitivity of the GC-LSPR sensor. (a) Calibration curves from 10 bulk calibrations $\Delta\lambda$ vs Δn; (b) mean calibration curve, the slope corresponds to $S_B = 328.6\ nm/RIU$. Each measurement corresponds to the mean ± σ of the measurements.*

The sensitivity value of 328.6 nm/RIU places our GC-LSPR sensor within the expected performance window of nanoplasmonic gratings derived from cost-effective substrates, such as DVD-R gratings (312 nm/RIU) and miniaturized GC-SPR devices (490 nm/RIU)

[114]. Confirming that our fabrication and Au deposition protocols yield surfaces that preserve the necessary optical coupling for strong plasmon excitation.

4.8 NOISE ANALYSIS AND LIMIT OF DETECTION

According to the IUPAC definition (1975), later clarified by the American Chemical Society (ACS), the limit of detection (LOD) is the lowest concentration of an analyte that an analytical process can reliably distinguish from the absence of that analyte [82]. To estimate the LOD of the GC-LSPR sensor in real-time measurements, the baseline noise level was quantified. Milli-Q water flowed over the sensing surface at 40 µL/min for 3160 min, and the output signal was recorded (**Figure 53**).

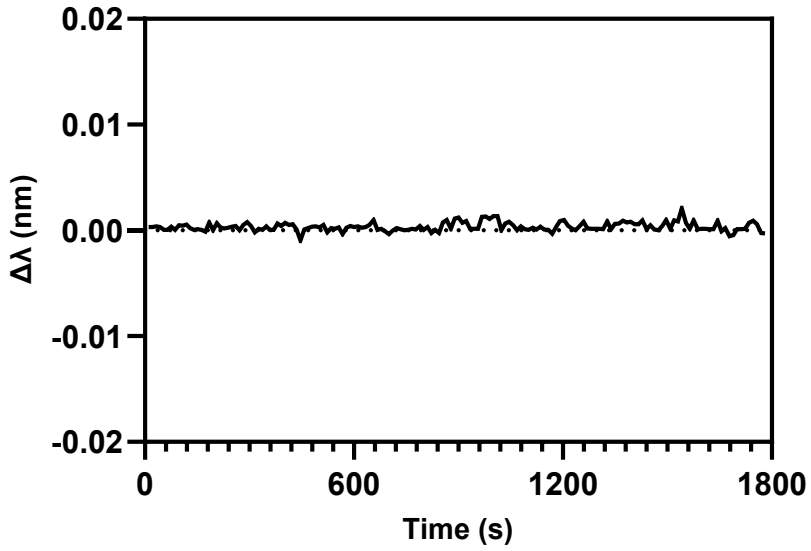


***Figure 53**. Noise level estimation from the baseline sensor response.*

From this baseline, the standard deviation was calculated as $\sigma_{blank} = 4.15 \times 10^{-4}$ nm, with a mean baseline value of $\mu_{blank} = 3.43 \times 10^{-4}$ nm.

There is no single universally correct formula for LSPR LOD determination; the choice depends on the sensor configuration, measurement noise characteristics, and data availability:

- σ (SD of blank measurements): the simplest approach, suitable when the blank noise dominates [64,65].
- σ_{low} (SD of the low-conc replicates): preferred when low-level measurements have additional variability due to factors such as binding kinetics or sample handling [64,65].

Considering the average bulk sensitivity of the GC-LSPR sensor ($S_B = 328.6$ nm/RIU) the limit of blank (LoB) and LOD were determined following the Clinical and Laboratory Standards Institute (CLSI) EP17-A2 guideline [115], which is widely adopted in biosensor performance evaluation. This method separates the contribution of baseline

(blank) noise from the variability at low analyte levels, yielding a statistically defined detection threshold.

The LoB was calculated as:

$$LoB = \mu_{blank} + 1.645\sigma_{blank}$$

$$LoB = 3.43x10^{-4} + 1.645(4.15x10^{-4}) = 1.026x10^{-3}\ nm$$

And the LOD as:

$$LOD = LoB + 1.645\sigma_{blank}$$

$$LOD = 1.026x10^{-3} + 1.645(4.15x10^{-4}) = 1.708x10^{-3}\ nm$$

Converting the signal to RIU we obtain:

$$\Delta RIU = \frac{LOD - \mu_{blank}}{slope}$$

$$\Delta RIU = \frac{1.708x10^{-3} - 3.43x10^{-4}}{328.6} = 4.16x10^{-6}\ RIU$$

This value matches the LOD obtained using the International Council for Harmonisation (ICH) analytical chemistry formula [65]:

$$LOD = 3.3\frac{\sigma}{S}$$

$$LOD = 3.3\frac{4.15x10^{-4}}{328.6} = 4.17x10^{-6}\ RIU$$

Both methods are valid; the CLSI EP17-A2 procedure explicitly accounts for blank behavior and low-level variability, while the ICH approach is more direct and suited to systems with a well-characterized linear calibration at low concentrations. The use of LoB and LOD calculations in this study ensures that the reported sensitivity reflects the intrinsic performance of the sensing platform, independent of any specific analyte calibration, enabling fair comparison with other LSPR and SPR-based grating sensors [64].

Comparable GC plasmonic sensors have reported bulk RI detection limits in the same order of magnitude: Au-coated replicated gratings with differential "optical switch" readout (~10^{-6} RIU) [116], BDs replicated nanogratings with Au films (6.3×10^{-6} RIU) [66], and modified DVD-based GC-SPR (7×10^{-6} RIU) [117]. The GC-LSPR sensor developed here, with a bulk LOD of 4.2×10^{-6} RIU, works well within the state-of-the-art range for gold grating-based plasmonic biosensors (**Table 7**).

Table 7. *Comparison of bulk refractive index detection limits of grating-coupled plasmonic sensors.*

Sensor platform	LOD (RIU)	Reference	Notes

Au-coated gratings	× 10^{-6}	[116]	High stability via optical switching
BDs nanograting with Au film	6.3 × 10^{-6}	[66]	Integrated microfluidics; high FOM
Modified DVD-based GC-SPR	7× 10^{-6}	[117]	Surface modification to sharpen resonance
GC-LSPR (this work)	**4.2 × 10^{-6}**	-	Real-time measurement

4.9 CHARACTERIZATION OF THE SENSOR SURFACE BIOFUNCTIONALIZATION

The analytical performance of plasmonic biosensors is dominated by surface chemistry and the biochemical changes that can be detected. Biofunctionalization has three main characteristics: (i) capture efficiency and orientation of the immobilized receptor, (ii) specificity of analyte recognition/anti-fouling, and (iii) signal stability because it can control receptor orientation, packing density, and nonspecific adsorption at the metal/dielectric interface. Literature of plasmonic surface chemistry shows that poorly oriented or overly dense antibody layers reduce active binding sites, whereas optimized chemistries enable lower LOD and better reproducibility [118,119].

To improve antigen-binding accessibility while anchoring immunoreceptors on gold, oriented immobilization strategies are preferred over random physisorption. Fc-selective capture via Protein G presents Fab domains and increases functional activity compared with randomly adsorbed IgG [120]; cysteine-tagged recombinant Protein G on Au is a well-documented route that strengthens attachment through Au-S bonds and enhances IgG binding. At the same time, antibody surface density must be tuned to avoid steric crowding, which otherwise limits target access and lowers apparent affinity [121].

Having these principles in mind, we optimized an oriented Fc-capture layer using cys-Protein G to immobilize anti-C5b-9 IgG on the Au-coated nanogratings. pH-guided preconcentration was used to promote electrostatic accumulation during coupling while minimizing denaturation; antibody concentration was then adjusted to reach optimal working conditions [119]. Because clinical matrices (e.g., serum) are biologically complex, we also incorporated PLL-PEG + BSA blocking to suppress nonspecific adsorption and stabilize the baseline during real-time LSPR readout. Together, this strategy targets high on-rate capture, low background, and robust regeneration, which are key requirements for label-free quantification of sC5b-9 in patient samples.

4.9.1 Biofunctionalization strategy

For the biofunctionalization of the sensor surface, we utilized a modified cys-Protein G with a dual chemisorption-physisorption mechanism and exploit the formation of covalent bonds between the thiol groups of the cysteines to the gold surface (Au-S).

The immobilization of cys-Protein G onto the gold surface relies on a dual-step physisorption-chemisorption process dictated by pH. Chemically, the terminal cysteine residue binds to the gold surface via the oxidative cleavage of its thiol group ($-SH$), resulting in the loss of a proton and the formation of a stable, covalent-like gold-thiolate ($Au-S$), bond (**Error! Reference source not found.**) [90]. The pH is important for favoring immobilization and avoiding nonspecific binding because it influences the electrostatic interactions between the bioreceptor and the sensor surface [122]. At optimal pH levels, the charges on both components are balanced, promoting specific binding while minimizing nonspecific interactions. Additionally, pH affects protein conformation and reactivity of functional groups involved in immobilization.

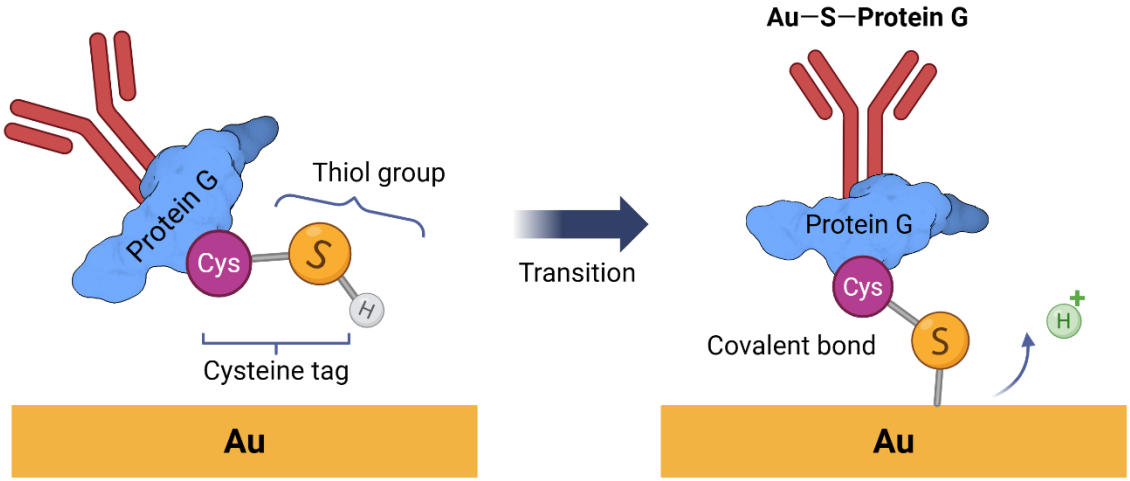


Figure 54. *Schematic illustration of the immobilization mechanism of cys-Protein G onto the gold surface. (Left) The protein tagged with the cysteine and its terminal thiol group (-CH_2-SH) into proximity of the gold surface. (Right) The oxidative addition drives the cleavage of the S-H bond, resulting in the loss of a proton (H^+) and the formation of covalent bond of Au-S-Protein.*

Although, alkaline conditions favor the formation of the highly nucleophilic deprotonated thiolate ion ($-S^-$) the macromolecular electrostatic architecture of the protein dominates the assembly kinetics. Recombinant Protein G exhibits an isoelectric point (pI) of approximately 4.1.

By selecting the appropriate pH for preconcentration we enhance specific binding and reduce nonspecific adsorption, leading to more efficient immobilization. At pH 4.0, the protein maintains a net positive charge, facilitating strong electrostatic attraction and pre-concentration toward the slightly negative gold surface. As the pH increases to 5.0 and 6.0, the protein transitions past its pI, reducing its net positive charge and inducing electrostatic repulsion both between adjacent protein molecules and the gold interface.

This directly hinders effective surface packing and results in the lower LSPR signal response observed in **Figure 55a.**

Next, we proceeded to optimize the bioreceptor concentration by testing a range of concentrations and high responses were observed with both 50 µg/mL and 100 µg/mL of cys-Protein G, but 100 µg/mL was selected as the optimal concentration to maximize the available Fc-binding sites in an oriented fashion on the surface for antibodies to attach and preserve Fab accessibility (**Figure 55b**) [106].

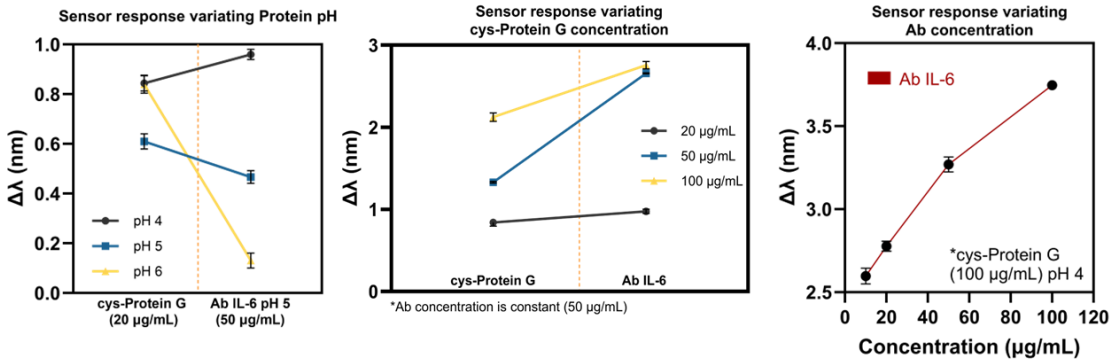


***Figure 55**. Effect of the pH and concentration in the immobilization-response of the biosensor (a) Plot demonstrates cys-Protein G attachment efficiency to the surface with different pH values. (b) Plot demonstrating different concentrations of cys-Protein G and IgG antibody to determine most efficient working conditions. (c) Curve displacements of different antibody concentrations by monitoring the shifts in the plasmonic band position (Δλ, nm).*

Finally, when varying the antibody concentration (anti-IL-6), the biosensor showed an increasing response (Δλ) to its target analyte (IL-6, 250 ng/mL), suggesting efficient antibody immobilization and orientation. It is worth noting that the maximum saturation behavior was not achieved likely due to the steric hindrance effect. Based on these results, 50 µg/mL was selected as the optimal concentration for performance and material efficiency. **Figure 55** shows the combined effect of pH and concentration optimization on sensor performance.

The cys-Protein G/IgG strategy provides an oriented, high-capacity capture layer that when pre-concentration is performed below its pI (pH 4; SAB) and use the optimized concentrations we maximize Fab exposure and increase sensitivity.

4.9.2 Anti-fouling technique

To minimize and prevent nonspecific adsorption and interaction of biomolecules on the sensor surface when working with complex matrices such as serum, a common strategy is to add a (i) non-fouling polymer such as PLL-PEG and (ii) BSA protein. The protection property of PLL-PEG is due to their steric-entropic barrier properties coupled with hydration molecules of PEG and the BSA at 5% has been proven to effectively reduce nonspecific interaction from serum for its strong adsorption of gold [20,100]. After

reaching optimal sensing conditions with complex media, it was later assessed with Ab C5b-9 (**Figure 58**).

The anti-fouling performance of PLL-PEG was evaluated by monitoring the wavelength shift (Δλ, nm) upon injection of single-protein solutions. As shown in **Figure 56**, when 1% BSA was introduced to a biosensor surface previously treated with 0.75 mg/mL PLL-PEG, a residual shift of Δλ = 0.23 nm was observed relative to bare gold. This indicates incomplete blocking and some degree of non-specific adsorption.

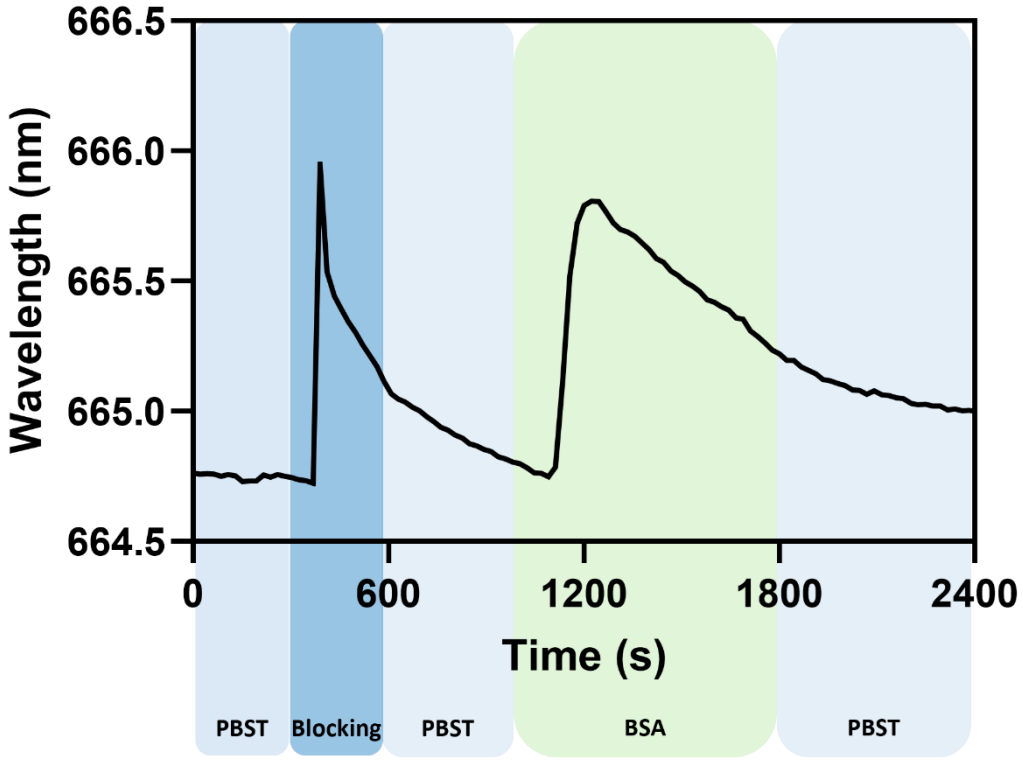


Figure 56. *Real-time sensogram showing the response of a biosensor surface treated with 0.75 mg/mL PLL-PEG after the injection of 1% BSA. A residual shift (Δλ = 0.23 nm) indicates partial non-specific adsorption.*

To improve anti-fouling performance, a combined blocking strategy using 0.75 mg/mL PLL-PEG and 1% BSA was evaluated. A biosensor functionalized with anti-C5b-9 was exposed first to a control protein (recombinant IL-6, 100 ng/mL). As shown in **Figure 57**, no significant wavelength shift was detected, indicating effective suppression of non-specific binding. In contrast, subsequent injection of the specific target (sC5b-9) resulted in a clear shift in Δλ (nm), confirming the specificity of the functionalized biosensor surface.

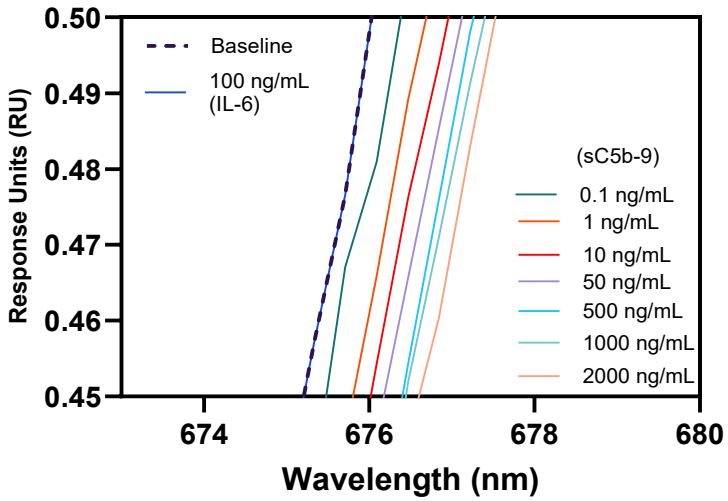


Figure 57. *Sensogram showing the biosensor response with anti-C5b-9 after anti-fouling treatment with 0.75 mg/mL PLL-PEG + 1% BSA. No shift was observed after injecting IL-6 (100 ng/mL), while a specific signal was recorded after serial injection of sC5b-9.*

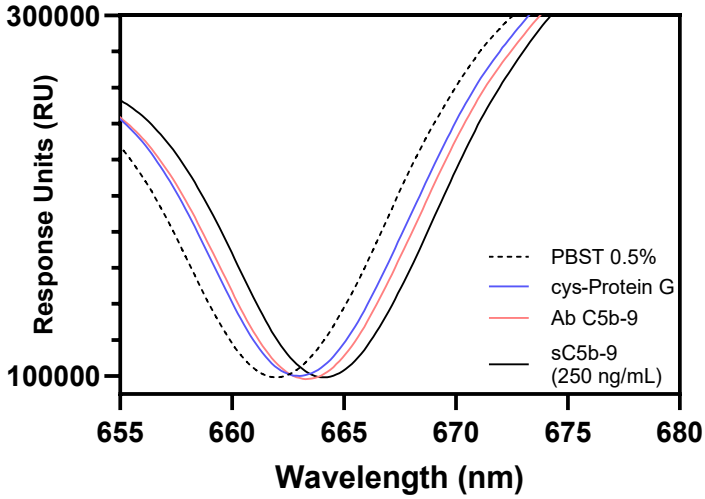


Figure 58*. Sensogram peak shift response in wavelength (Δλ, nm) of the biosensor when performing the biofunctionalization of cys-Protein G and Ab C5b-9 onto the surface and its response to sC5b-9 (250 ng/mL).*

One of the main challenges in working with serum samples is the high abundance of proteins such as albumin, globulins, and lipoproteins, which tend to adsorb nonspecifically to metallic or hydrophobic surfaces. In plasmonic biosensors, this "matrix effect" manifests as baseline shifts, steric hindrance of analyte binding, and competitive interactions with capture antibodies, ultimately reducing assay specificity and sensitivity [123,124].

To mitigate this interference, antifouling strategies are essential. PLL-PEG is widely considered a gold standard for antifouling, as its hydrated PEG chains create a steric and entropic barrier that resists protein adsorption by increasing hydrophilicity and repelling biomolecules [99].

However, PLL-PEG layers alone can exhibit incomplete coverage or degradation over time, leaving exposed regions susceptible to fouling. In contrast, bovine serum albumin (BSA) acts by strongly adsorbing onto metallic surfaces such as gold, passivating exposed sites, and reducing nonspecific interactions, though with less structural robustness compared to polymeric coatings [100]. In this work, we demonstrated that a combined strategy using PLL-PEG (0.75 mg/mL) and BSA (1%) provided synergistic benefits: PEG contributed steric-hydration repulsion, while BSA occupied residual adsorption sites, together achieving superior suppression of nonspecific binding (**Figure 56** & **Figure 57**). This mixed-blocking approach offers a practical compromise between advanced antifouling coatings such as oligo(ethylene glycol) self-assembled monolayers or zwitterionic polymers, both highly effective but more complex and costly to implement, and the simplicity of protein-based blockers. The PLL-PEG + BSA method thus represents a rational and scalable solution for ensuring reproducibility and specificity in serum-based plasmonic biosensing applications.

4.9.3 Time stability

Long-term stability in LSPR devices is governed by (i) film integrity, (ii) biorecognition layer robustness, and (iii) environmental factors. Gold films are chemically robust compared with Ag, but nanoscale morphology (grain growth, roughening) and Au-thiolate SAM ageing/desorption can still shift the resonance over time, especially under heat or solvent stress. These effects are well documented for SPR/LSPR gold interfaces and SAMs [113,120,121].

The biofunctionalization interface is often the biggest source of drift: antibodies and protein capture layers (e.g., cys-Protein G) can lose activity by denaturation, hydrolysis, or weak/incorrect orientation, which reduces effective binding sites and changes the local refractive index [125]. Oriented Fc-capture and covalent “docking” after pre-concentration improve activity retention vs random physisorption [126,127].

Environmental and operational factors: temperature fluctuations, humidity changes, and pH variability can affect both the bulk refractive index, thus changing the plasmon wavelength and the biorecognition interface [125,128].

To evaluate the long-term stability of the GC-LSPR biosensor performance, a series of real-time measurements were conducted over different time points (48 hours, 22 days, and 30 days) after sensor biofunctionalization. The biosensors were stored at 4 ºC under two conditions: dry and submerged in PBS buffer, to assess how hydration impacts sensor longevity. The sensing response was evaluated by injecting a 100 ng/mL of recombinant sC5b-9 protein.

In **Figure 59**, we can observe sensors stored dry showed a progressive decrease in signal intensity and more pronounced signal drift as storage time increased, with the 30-day

sensor showing a visible lower response and reduced signal stability. This decline is likely due to protein desorption, conformational degradation of antibodies, and possible oxidation of the gold film under dry storage [110].

In contrast, biosensors submerged in PBS buffer maintained a more stable signal response over 48 hours of PBS storage, with minimal signal drift and good stability. This early performance suggests that water activity has yet to influence the degradation of antibodies and their chemical stability [129].

However, on day 22, there was a substantial drop in response amplitude, with Δλ decreasing by over 50% compared to the initial timepoint. By the 1-month mark, the sensor had severely decreased signal intensity, indicating loss of sensing capabilities. This is likely due to protein degradation, hydrolysis, or detachment of the biorecognition element (Ab C5b-9), consistent with literature of protein-based interfaces degrading under constant aqueous exposure [130]. Additionally, the thiol-Au bonds can suffer oxidation in aqueous conditions, further affecting the biointerface performance.

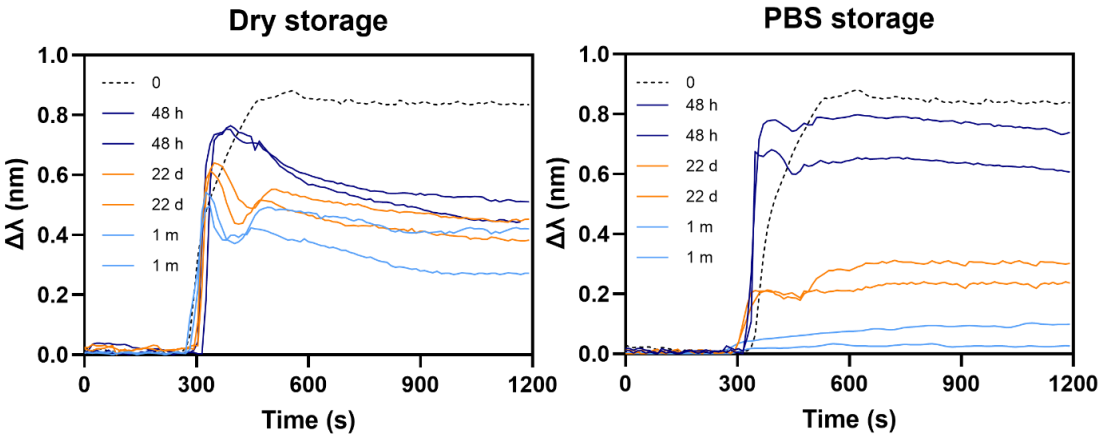


***Figure 59**. Comparison of real-time biosensor response to 100 ng/mL of recombinant sC5b-9 after storage at 4 °C for 48 hours, 22 days, and 30 days under two different conditions. Left panel: biosensors stored dry. Right panel: biosensors stored submerged in PBS buffer. Sensor performance is evaluated based on peak response intensity and dissociation stability.*

These results provide an insight into storage strategy: while PBS immersion supports short-term bioactivity preservation, is not suitable for long-term sensor storage without further stabilization measures such as lyophilization, cryoprotectants, or encapsulation techniques. Therefore, if shelf life is required, optimization of storage protocols must be considered.

4.9.4 Matrix effect in serum

Matrix effect in LSPR biosensors represent one of the most significant challenges when transitioning from optimized buffer conditions to real biological samples. Human serum, a highly heterogeneous fluid, is a complex biological array containing high concentrations of proteins, lipids, metabolites, and other endogenous compounds that can compromise

biosensor performance [123]. Understanding and mitigating these effects is crucial when developing a reliable biosensor for clinical applications.

The matrix effect is typically defined as analyte-independent variations in sensor response caused by the interaction of the sample matrix with the sensing interface , [124,131,132]. These effects manifest in LSPR systems as (i) nonspecific adsorption of serum proteins to the sensor surface, (ii) signal suppression due to surface fouling, and (iii) competitive binding between the target analyte and abundant matrix components [81].

To evaluate matrix interference on biosensor performance, sequential dilutions (1:100 to 1:1) of commercial human serum (CHS) after regenerating with Glycine (1 M; pH 2.2) were assessed. As expected, a strong signal ($\Delta\lambda$ = 2.75 nm) was observed when undiluted serum was injected, indicating high nonspecific adsorption likely due to the elevated protein content and viscosity of native serum (**Figure 60**). But we also observed a loss of biosensor activity, due to regeneration being too harsh on the biofunctionalized structure.

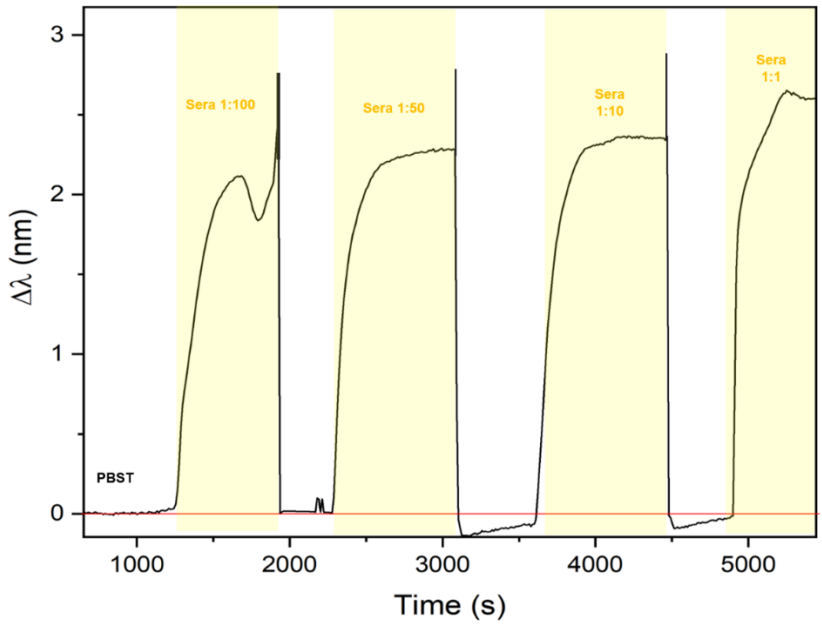


***Figure 60**. Baseline response of different dilutions of commercial human sera (1:100, 1:50, 1:10, and 1:1) attachment before and after regeneration with Glycine. Showing the highest signal Δλ = 2.75 nm for 1:1.*

This result prompted us to evaluate the matrix effect with a fresh biosensor each measurement to assess the balance between reducing nonspecific binding and maintaining sample integrity, CHS with and without recombinant sC5b-9 (250 ng/mL) were compared across serial dilutions (1:1 to 1:100). A stronger signal was consistently observed in spiked samples, confirming the ability of the biosensors to detect the target protein (**Figure 61**).

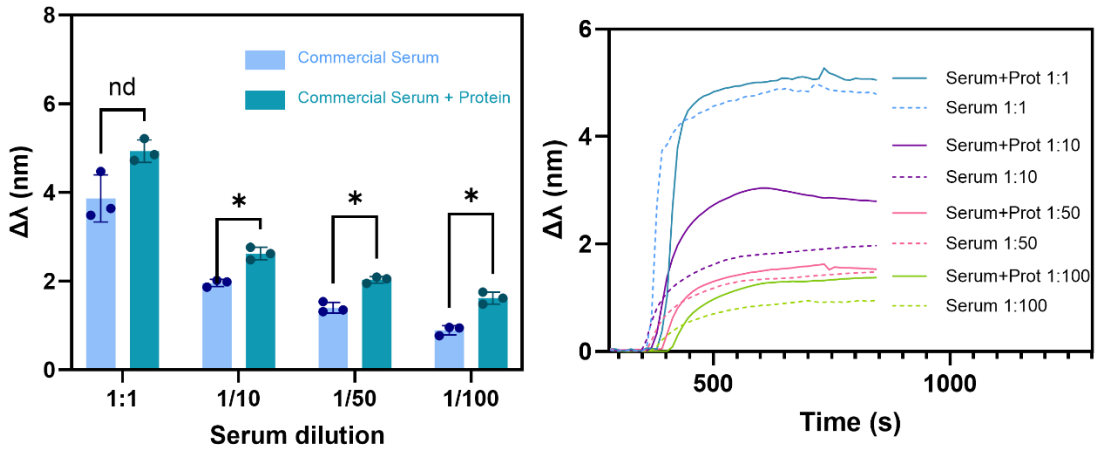


***Figure 61**. Biosensor response to different serum dilutions comparing commercial serum alone and commercial serum spiked with recombinant protein sC5b-9 = (250 ng/mL).*

Although the 1:1 dilution showed the largest absolute shift (Δλ = 1.06 nm), it was not statistically significant (p = 0.055), due to high variability in undiluted serum. Statistically significant differences between blank and spiked samples were found at 1:10, 1:50, and 1:100 dilutions, with the greatest significant shift at 1:100 (Δλ = 0.73 nm). These results indicate that 1:100 is the optimal working dilution for serum analysis with minimal matrix effect and adequate sensitivity. The matrix effect of serum, characterized by nonspecific adsorption of abundant serum proteins, initially compromised signal clarity (**Table 8**).

***Table 8.** Summary of biosensor response shifts (Δλ, nm) at different serum dilutions, comparing commercial serum alone and commercial serum spiked with protein sC5b-9.*

Dilution	Serum (Δλ, nm)	Serum + Protein (Δλ, nm)	Absolute shift (nm)	q-value	Relative increase (%)
1:1	3.867	4.929	1.062	0.0140	27.5%
1:10	1.958	2.622	0.665	0.0016	33.9%
1:50	1.399	2.032	0.633	0.0016	45.2%
1:100	0.890	1.618	0.728	0.0016	81.9%

**Unpaired t test with Welch correction with method of Two-stage step-up (Benjamini, Krieger, and Yekutieli)*

To mitigate these effects, we employed a dual antifouling strategy combining PLL-PEG surface blocking and 1% BSA supplementation. Poly(ethylene glycol)-based coatings are known to resist protein adsorption through the formation of a sterically hydrated layer, effectively minimizing nonspecific binding without compromising target accessibility [133,134]. This strategy, together with dilution, substantially reduced non-specific adsorption while preserving analyte detectability. As shown in **Figure 61**, the 1:100 dilution consistently yielded the most reproducible response and highest relative increase in signal (81.9%) upon spiking with recombinant sC5b-9.

Nevertheless, nonspecific interactions were not completely removed, suggesting that further optimization is necessary for the detection of the protein. Further work should explore alternative anti-fouling chemistries, such as zwitterionic polymers which offer superior resistance to protein fouling in complex matrices or hydrogel coatings [135,136].

Moreover, modifying the running buffer composition and incorporating differential referencing strategies could further enhance analytical robustness. Blank injection was used in this work as a reference correction to account for bulk RI changes and nonspecific binding [101].

In summary, the matrix effect represents a critical barrier to biosensor clinical translation. However, through sample dilution, antifouling strategies, and analytical referencing, our GC-LSPR platform demonstrated effective sC5b-9 detection in diluted serum. The optimal 1:100 dilution provides a practical balance between matrix suppression and analytical sensitivity, representing a promising benchmark for future clinical assay development.

4.9.5 Affinity validation of the BRE in a complex matrix

To evaluate the specific binding capability of the immobilized biorecognition element (BRE, Ab C5b-9), a control assay was performed injecting 250 ng/mL of recombinant sC5b-9 in a complex matrix (CHS) into the biosensor. The sensing surface was divided into two independent regions: one spot was functionalized with cys-Protein G followed by the anti-C5b-9 antibody (with BRE), while the control spot was functionalized with cys-Protein G (without BRE) (**Figure 62**).

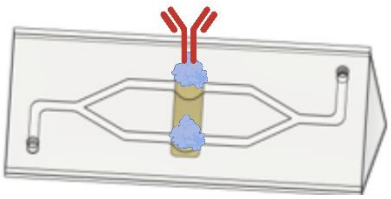


***Figure 62**. Schematic representation of one spot functionalized with cys-Protein G + BRE (Ab C5b-9); while the control spot was only functionalized with cys-Protein G.*

The resulting sensogram shown in **Figure 63** displays the wavelength shift (Δλ, nm), upon injection and dissociation of the analyte. During the association phase, both spots showed an initial increase in signal, reflecting the general RI change induced by biomolecular adsorption at the surface, a common phenomenon in LSPR due to its high surface sensitivity [84]. However, during the dissociation phase, the two spots have significant differences. The BRE-functionalized spot maintained a stable signal of $\Delta\lambda = 0.68$ nm, indicating a specific and high-affinity of sC5b-9. In contrast, the control spot signal decreased over time down to ($\Delta\lambda \approx 0.56$ nm), indicating non-specific adsorption and weak affinity interactions.

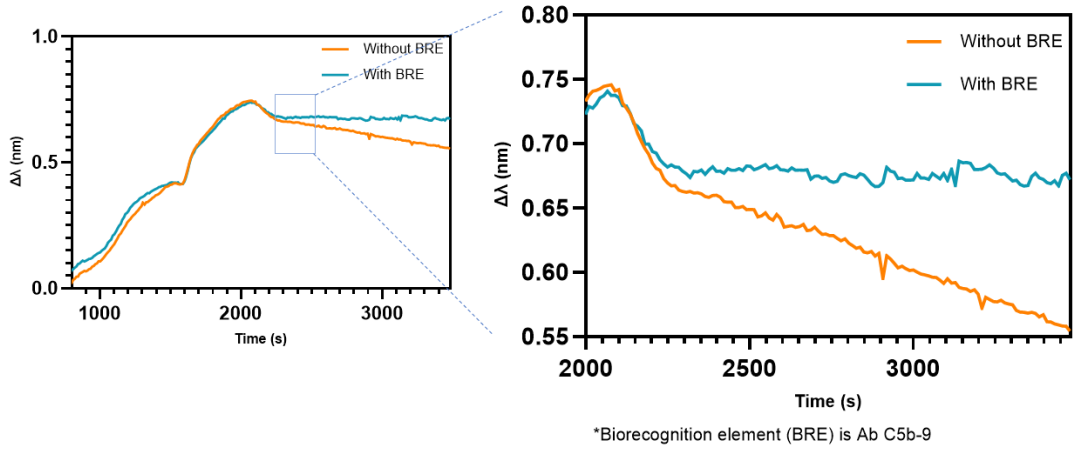


Figure 63. *Real-time sensogram response of the biosensor with two channels. Blue line: Spot functionalized with cys-Protein G + BRE (Ab C5b-9). Orange line: Spot functionalized only with cys-Protein G (control).*

The different behaviors confirm the specific affinity of the Ab C5b-9 towards the target analyte, validating its functionality as a biorecognition element within the sensor surface. For a biosensor it is important to maintain stability over time. The rapid decay in signal observed in the control spot suggests low retention of sC5b-9.

Furthermore, these results validate the affinity performance of the BRE and the efficiency of the cys-Protein G orientation strategy. Tail-on orientation of the antibody is known to enhance the accessibility of the antigen-binding site, leading to improved analyte recognition and stronger binding kinetics [90,137]. Moreover, the ability of the biosensor to maintain a stable response even in complex matrices such as CHS highlights the robustness of both the functionalization and the GC-LSPR sensor.

These results serve as a model for distinguishing nonspecific binding in future work. The integration of a dual channel offers internal referencing capabilities, improving the precision of detection by compensating for background noise or sensor drifts [138]. Overall, this confirms the analytical functionality of the biosensor, ensuring that the immobilized antibody can recognize and bind to sC5b-9 with high specificity.

4.9.6 Calibration of the biosensor

Notably, grating nanostructure designs, especially period and depth, have been shown to significantly affect calibration response by altering the plasmons efficiency [103]. This work provides a BD-derived grating platform combined with a 68 nm Au film and an oriented Fc-capture biointerface that enables analyte detection.

To characterize the analytical performance of the biosensor, calibration curves were constructed using increasing concentrations of recombinant sC5b-9 diluted in two biological relevant matrices: cell culture media (DMEM) and CHS. Calibration is a critical step in biosensor development, as it defines the sensor's quantitative capacity by relating optical response (Δλ, nm) to analyte concentration.

In LSPR biosensors, this relationship is affected by bulk refractive index sensitivity, grating geometry, and surface chemistry, which together affect the dynamic range, LOD, and saturation behavior [103,139]. Biochemical diagnostics procedures, such as protein binding, rely on biomolecular interactions, and therefore, their calibration curves are more complex.

4.9.6.1 Calibration in cell culture media

The calibration curve in cell culture media displayed a sigmoidal response characteristic of molecular recognition and affinity. Curve fitting was performed using both four-parameter (4PL) and five-parameter (5PL) logistic regression models. While the 4PL model is widely used for symmetric curves, the 5PL provided the best fitting of the experimental data due to its added flexibility when challenged with asymmetry. Selecting an appropriate model improves the reliability of quantitative estimates.

The LOD (0.1618 ng/mL) was calculated using the ICH method where the standard deviation of the blank media was calculated as $\sigma = 0.7798\, ng/mL$, following the equation:

$$LOD = 3.3\frac{\sigma}{S}$$

$$LOD = 3.3\frac{0.7798}{15.9} = 0.1618$$

The IC_{50} was 223.3 ng/mL, with a steep Hill slope of 15.9 indicating cooperativity binding, which suggest the biosensor's capacity to differentiate slight changes in analyte concentration around the threshold (**Figure 64**). The analytical parameters can be found in **Table 9** and the sensor response in **Table 10**.

Table 9. *Analytical parameters for the calibration curve in cell culture media using 5PL fitting.*

Parameter	**Value**
LOD	0.1618 ng/mL
IC_{50}	222.3 ng/mL
Hill slope	15.9
R squared	0.9470

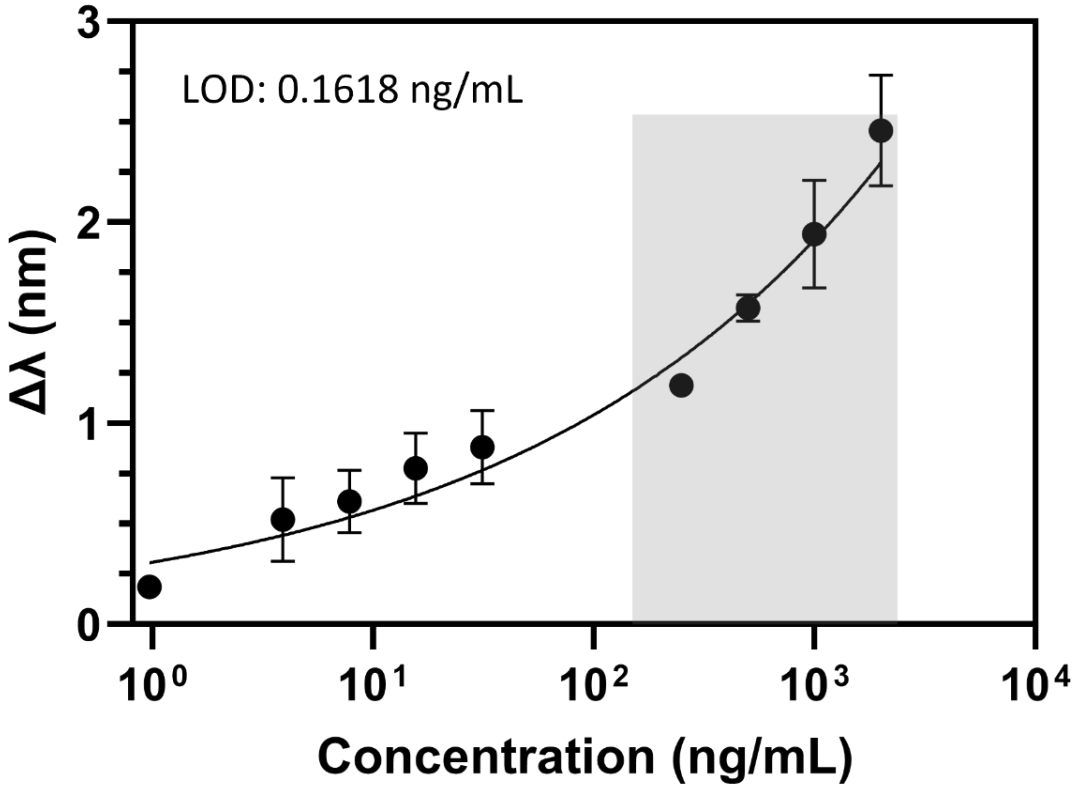


Figure 64. *Dose-response curve showing LSPR wavelength shift (Δλ, nm) against increasing concentrations of recombinant sC5b-9. Curve was fitted using a 4PL model. LOD was calculated as 0.1618 ng/mL.*

The resonance wavelength shift (Δλ, nm) increased with concentration, indicating a robust dose-response suitable for calibration. Precision was calculated as coefficient of variation (CV = 100 x σ/ Δλ), and it was higher in the extremes than in the mid-range.

At the lowest concentrations (0.97-31.25 ng/mL), Δλ was small and CV were large. In contrast, mid-range concentrations, i.e., 200-500 ng/mL yielded the lowest variability and at higher concentrations the response continued to grow but CV rose, consistent with the onset curvature as the surface approaches saturation.

Table 10*. Sensor response per concentration of sC5b-9.*

C (ng/mL)	Δλ (nm) ± SD (σ)	CV (%)
0.97	0.18625 ± 0.0274	14.72%
3.9	0.60375 ± 0.1401	24.88%
7.81	0.68395 ± 0.1037	16.03%

15.62	0.884 ± 0.1206	14.54%
31.25	0.96785 ± 0.1226	13.27%
250	1.1875 ± 0.0433	3.65%
500	1.5725 ± 0.0548	3.49%
1000	2.0025 ± 0.1903	9.65%
2000	2.45625 ± 0.2237	9.11%

** 250-500 show the lowest variability (CV< 3.5%)

It is important to note that concentrations between 250-500 ng/mL showed the lowest signal in variability (CV< 3.5%), representing a stable mid-linear range for quantification.

4.9.6.2 Calibration in Commercial Human Sera (CHS)

In contrast, calibration in 1:100 diluted CHS introduced complexity due to matrix effect (see Section 3.3.7). Initial linear regression yielded a poor $R^2 = 0.5469$, indicating that the biosensor's response to sC5b-9 in serum was nonlinear, likely due to saturation, steric hindrance, or competition from abundant serum proteins (**Figure 65**.

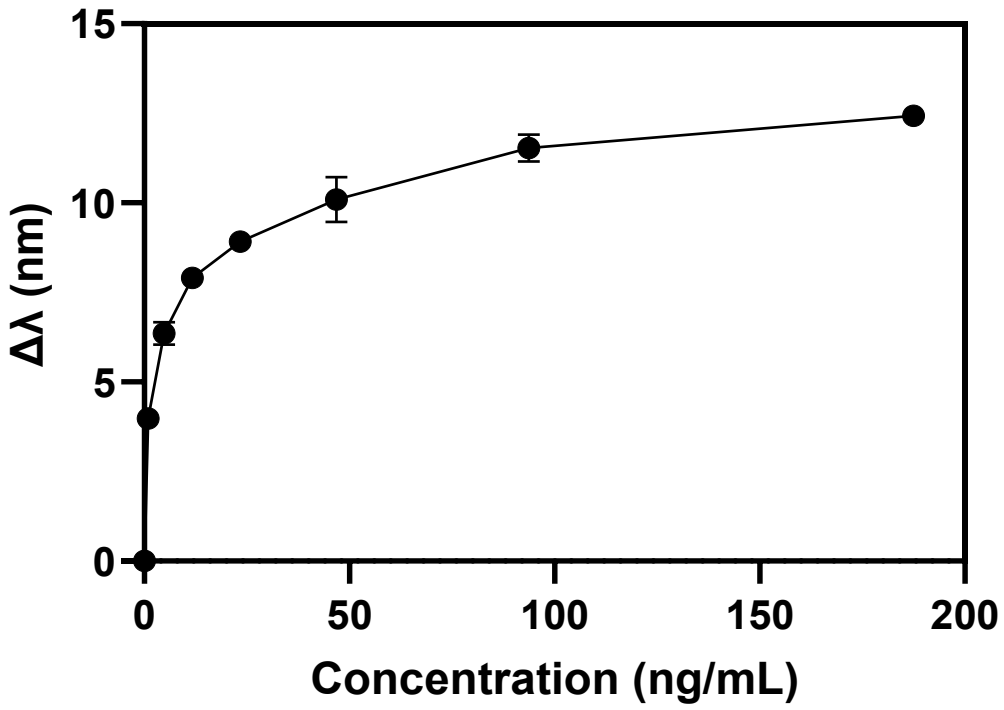


Figure 65. *Calibration curve fitted to a simple regression line.*

Furthermore, the data was fitted with a 4PL model, which is widely accepted for ligand-binding assays in biosensors where dose-response relationships follow a sigmoidal trend [119,140].

The optimized curve on

Figure 66 achieved a LOD of 0.015 ng/mL and an IC_{50} of 11.09 ng/mL, which supports the biosensor capability to function in complex and clinically relevant matrices. A Hill slope of 0.5173 indicates gradual but consistent change in the signal. The gradual slope is preferred in complex samples, such as serum, where variability is due to nonspecific adsorption and background matrix effects. All the analytical parameters can be found in **Table 11** and results of the sensor in **Table 12**.

Table 11. *Analytical parameters for the biosensor assay using 4PL fitting.*

Parameter	Value
LOD	0.011 ng/mL
IC_{50}	11.09 ng/mL
Hill slope	0.5173
R squared	0.9594

* All samples were measured in duplicate on the same biosensor chip.

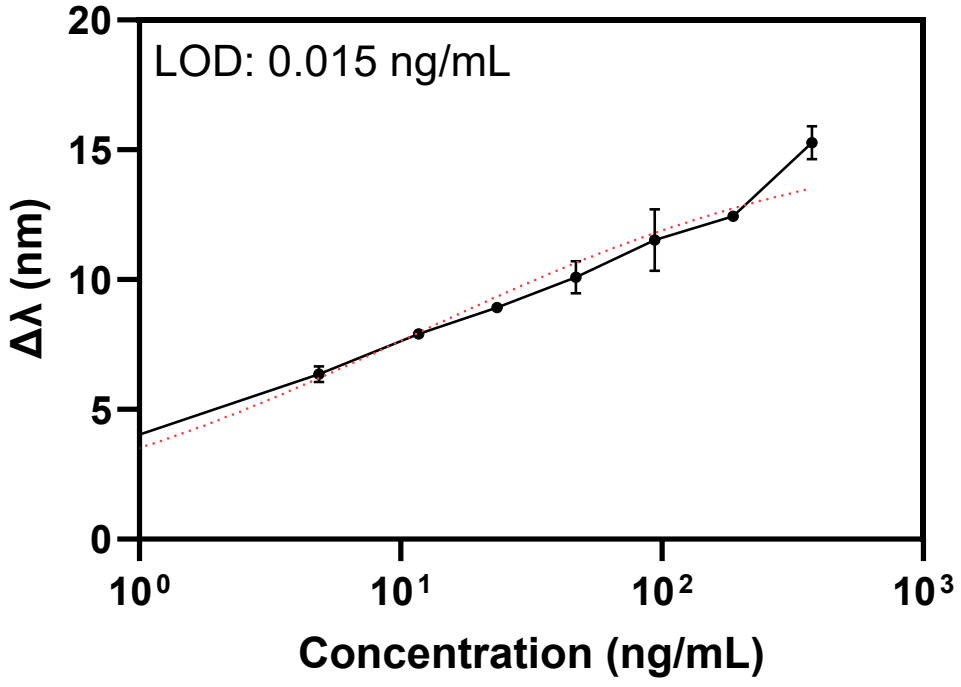


Figure 66*. Dose-response curve showing LSPR wavelength shift (Δλ, nm) against increasing concentrations of recombinant sC5b-9 in diluted CHS. Curve was fitted using a 4PL model. LOD was calculated as 0.015 ng/mL.*

Table 12. *Key parameters of the calibration curve for sC5b-9 conducted in diluted CHS*.*

C (ng/mL)	Δλ (nm) ± SD (σ)	CV (%)
0.97	3.951 ± 0.01267	0.32%
4.87	6.687 ± 0.01971	0.29%
11.71	7.91 ± 0.007278	0.09%
23.43	8.987 ± 0.08491	0.94%
46.87	10.42 ± 0.1328	1.27%
93.75	12.2 ± 0.2678	2.20%
187.5	12.5 ± 0.09177	0.73%
375	15.6 ± 0.08372	0.54%
750	40.98 ± 0.4027	0.98%
1500	62.74 ± 0.124	0.20%

*1:100 commercial human serum dilution in PBST 0.5% + CHAPS 25 mM Data was measured by duplicate in the same biosensor chip.

These results confirm that the biosensor maintains high analytical performance even in serum, with low coefficients of variation across the tested range. The 1:100 dilution strategy, combined with the optimized surface blocking, proved effective in balancing matrix suppression and analyte detectability.

4.9.6.3 Comparative performance and clinical implications

The GC-LSPR biosensor's LOD of 0.015 ng/mL in serum surpasses many conventional techniques. For example, enzyme-linked immunosorbent assay (ELISA) methods typically offer LODs in the 0.02-1 ng/mL range but require labeled reagents, multistep workflows, and hours to complete. The developed biosensor offers real-time, label-free detection with comparable sensitivity, presenting a powerful platform for future diagnostic tools or rapid monitoring of complement activation in AChR+ MG.

4.10 Evaluation of biosensor for real patients MG+ serum samples

This work presents the first reported LSPR-based biosensor for the detection of sC5b-9 in clinical serum samples. While SPR and SPRi platforms have been previously applied to detect AChR (Frykman et al., 2024) and MuSK antibodies (2020) [141,142], no prior study has focused on direct detection of sC5b-9 using label-free nanoplasmonic sensors. In this study, we developed a plasmonic biosensor capable of detecting and quantifying sC5b-9 in serum samples from patients with AChR+ MG. The biosensor demonstrated strong specificity and sensitivity, with a limit of detection (LOD) of 0.015 ng/mL. This result is comparable to or better than conventional immunoassays such as ELISA (typically >1 ng/mL) and RIPA (>1nmol/L) (See **Table A 4**) [33].

The ability to detect sC5b-9 is clinically relevant, as it reflects ongoing terminal complement activation, particularly in AChR+ MG where complement-mediated membrane damage contributes to neuromuscular junction (NMJ) pathology [17]. This biomarker could aid in monitoring the disease diagnosis, and treatment response, especially in the context of complement-targeting therapies like eculizumab [16].

4.10.1 Serum samples

An accuracy test was conducted to assess the sensor clinical applicability and precision to detect sC5b-9 in serum from patient's vs serum from healthy patients. A healthy serum sample produced no observable peak shift, whereas a positive patient sample generated a $\Delta\lambda$ of 0.8225 nm, indicating the presence of sC5b-9 and successful target recognition in complex biological media (**Figure 67**).

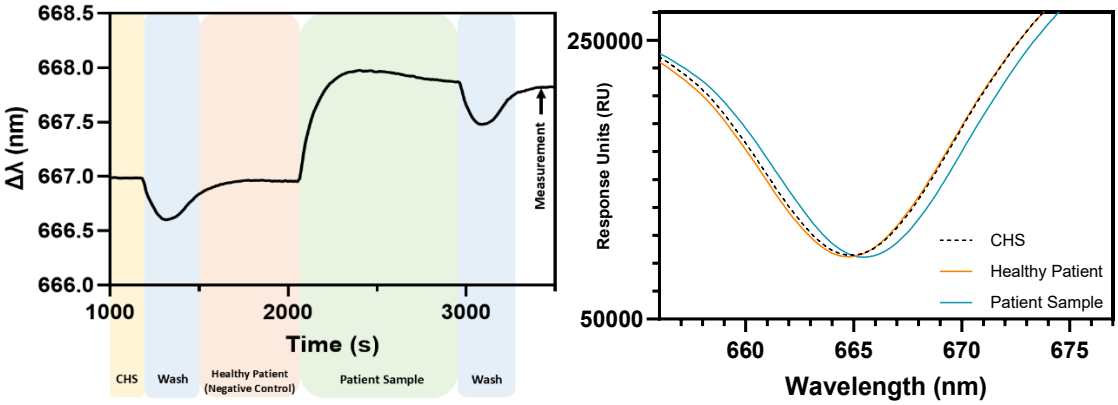


***Figure 67**. Real-time sensogram showing (a) CHS baseline, (b) PBST 1% wash, (c) healthy patient serum sample (1:100), (d) MG patient serum sample (1:100) and (e) PBST 1% wash. The shift in plasmon peak (Δλ, nm) confirms detection of sC5b-9 in the patient sample.*

The accuracy test demonstrates the biosensor's capability to differentiate between pathological and physiological serum conditions. As shown in **Figure 67**, healthy control serum did not produce a wavelength peak shift, consistent with the expected absence of elevated sC5b-9 in non-diseased individuals. In contrast, Myasthenia Gravis (MG) patient

serum produced a measurable wavelength displacement of $\Delta\lambda \approx 0.82$ nm, confirming that the biosensor can detect complement activation even within the complexity of diluted human serum. This result is particularly significant, as biological matrices such as serum are known to interfere with LSPR-based detection due to nonspecific adsorption, high protein content, and viscosity-induced mass transport limitations [81,143].

The observed signal shift validates that the immobilized anti-C5b-9 antibodies retain high specificity in complex matrices, enabling selective binding of the complement complex while minimizing interference. This capacity to distinguish between healthy and MG samples highlights the translational potential of the sensor for diagnostic and monitoring applications. In clinical diagnostics, accurate detection of complement activation markers such as sC5b-9 is crucial not only for confirming disease activity but also for monitoring therapeutic responses to complement-inhibiting drugs (e.g., eculizumab, ravulizumab) [144].

Finally, it is important to note that the biosensor's performance in diluted serum (1:100) suggests that appropriate pre-treatment of samples can mitigate matrix effects without compromising detectability.

4.10.2 Data Analysis and Curve Fitting

All 11 samples from patients were diluted 1:100 before testing. The results are summarized in **Figure 68** and **Table 13**. The results show there is a high response in patients 4 (P4) and patient 10 (P10) with concentrations exceeding 2 µg/mL and patients 7, 8 and 9 (P7, P8, and P9) show no measurable response. All other AChR+ patients (e.g., P1, P3, P5, P6) showed intermediate to low responses.

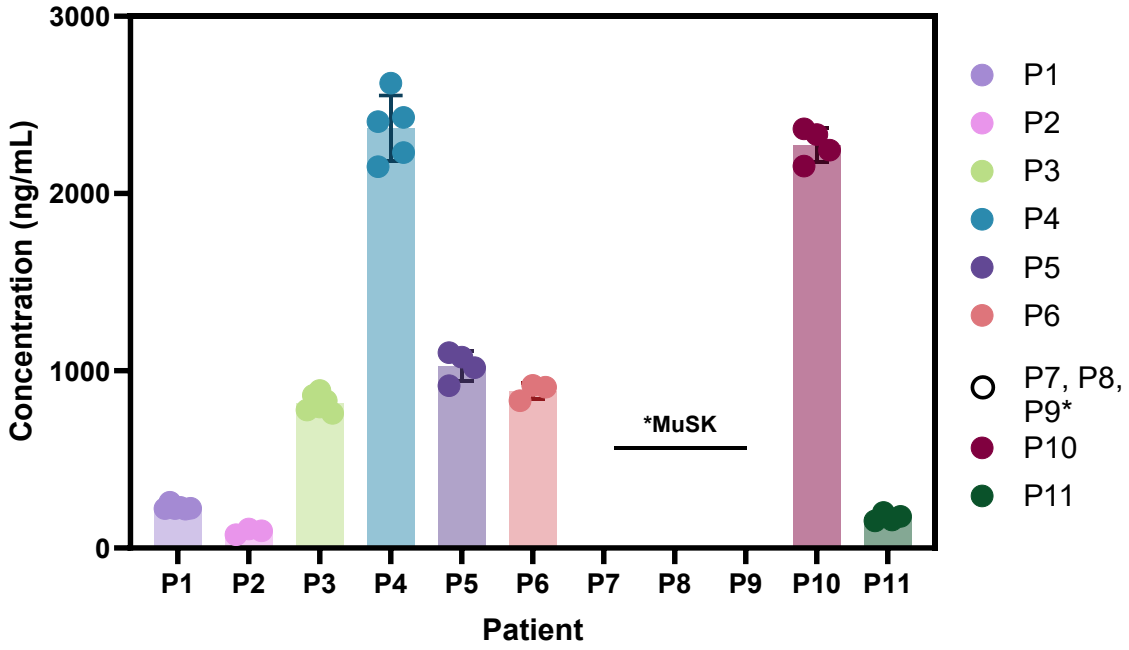


Figure 68. *Bar graph comparing calculated sC5b-9 concentrations in 11 patient serum samples. Patients P7, P8, and P9 are MuSK-positive; others are AChR+.*

We validated the biosensor using serum samples from 11 MG patients (AChR+ and MuSK-positive). Notably, P4 and P10, both AChR+, exhibited the highest sC5b-9 levels, suggesting active complement involvement. In contrast, all MuSK+ samples (P7, P8, P9) showed no detectable sC5b-9.

These findings align with existing literature indicating that MuSK antibodies (mostly IgG4) do not activate complement. This lack of response in MuSK+ MG samples supports the hypothesis that patients without C5b-9 exhibit alternative (non-complement) immunopathogenic mechanisms [27]. Therefore, this biosensor may be especially valuable for differentiating MG subtypes and monitoring treatment efficacy in complement-inhibitor therapies.

Detection of sC5b-9 in serum is crucial because it provides real-time information about ongoing complement activation, especially in AChR+ MG where complement plays a damaging role to the NMJ. It helps diagnose and monitor patients, making it a valuable biomarker since the complement activation is a result of the complement cascade, and there are therapeutic candidates such as Eculizumab, approved by the FDA for AChR+ MG treatment [47].

Complement inhibitors are highly promising therapies, but they can have a wide response depending on patient-specific factors or different complement activation degrees. Therefore, the identification of patients that may benefit from complement inhibition treatment is desired [47].

Table 13. *Key parameters of the diluted serum of 11 patients with myasthenia gravis* in the biosensor.*

	Mean (ng/mL) ± SD (σ)	**SE**	**CV**
P1♦	229.3 ± 14.28	5.83	6.227%
P2**	93.28 ± 16.26	9.388	17.43%
P3♦	819.7 ± 49.97	20.4	6.097%
P4♣	2368 ± 184.8	82.63	7.802%
P5***	1028 ± 82.84	41.42	8.059%
P6***	886.2 ± 47.17	27.23	5.323%
P7**	-	-	-

P8**	-	-	-
P9**	-	-	-
P10***	2274 ± 94.27	47.13	4.145%
P11***	172.4 ± 21.53	10.76	12.48%

**1:100 patient serum dilution in PBST 0.5% + CHAPS 25 mM*
*** Samples were measured by triplicate, two from the same biosensor chip and one from a different biosensor chip.*
**** Samples were measured by quadruplicate, two biosensor chips with two replicates.*
♣*Samples were measured by quintuplicate, two biosensor chips with two replicates and one from a different biosensor.*
♦*Samples were measured by sextuplicate, three biosensors with two replicates.*

4.11 COMPARATIVE STUDY OF ELISA AND GC-LSPR BIOSENSORS

ELISA is the gold standard for immunoassays and is widely used for its high sensitivity and specificity. The methodology is a plate-based assay that enables both quantitative and qualitative detection of specific antigens using labeled antibodies. Despite its sensitivity, ELISA is resource-intensive: it requires expensive reagents, long incubation times, multiple wash steps, and trained personnel, making it less suitable for near-patient or point-of-care applications. Additionally, ELISA performance in complex media such as serum can be compromised by nonspecific adsorption and matrix effects, while false positives may arise from cross-reactivity or non-specific interactions [145]. These limitations highlight the need for alternative detection methods that maintain sensitivity while offering faster, simpler workflows suitable for clinical diagnosis.

To validate the clinical performance of the GC-LSPR biosensor, patient serum samples were analyzed in parallel with ELISA. Samples were diluted at 1:100 to reach the manufacturer's recommended detection range (31.25-2000 ng/mL).

The ELISA calibration curve (**Figure 69**) showed a LOD of 2.54 ng/mL, in line with manufacturer-reported sensitivity (~18.75 ng/mL). By contrast, the GC-LSPR biosensor achieved a much lower LOD (0.015 ng/mL, Section 4.9.6.2), representing a >150-fold improvement in analytical sensitivity compared to ELISA.

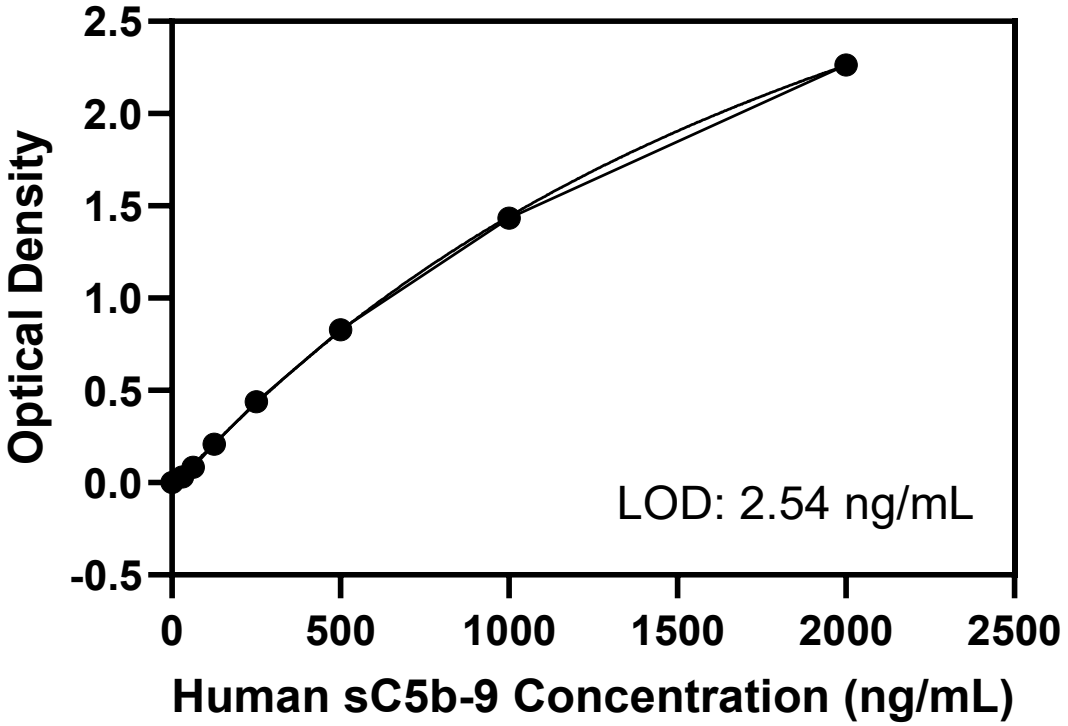


Figure 69. *Calibration curve of human sC5b-9 measured by ELISA. The limit of detection (LOD) was determined to be 2.54 ng/mL.*

Direct comparison of patient samples measured by both techniques (**Table 14**) revealed excellent correlation in the mid-to-high concentration range (Pearson r = 0.9564; R^2 = 0.9148), although some discrepancies were observed at lower concentrations where ELISA sensitivity is limited. For instance, samples P1 and P2 showed underestimation by LSPR relative to ELISA, which may reflect either cross-reactivity in ELISA or insufficient signal referencing in the biosensor at borderline concentrations. Importantly, at clinically relevant concentrations (>100 ng/mL), both platforms provided concordant results, supporting the reliability of LSPR for quantitative assessment of complement activation.

Table 14*. Comparison of sC5b-9 quantification by ELISA and GC-LSPR biosensor in patient serum samples (1:100 dilution).*

	ELISA (ng/mL)	**LSPR (ng/mL)**
P1	356.6932	229.3
P2	591.2504	93.28
P3	1027.463	819.7
P4	2250.305	2368
P5	945.4051	1028

P6	960.0328	886.2
P7	25.10995	-
P8	22.3408	-
P9	18.44639	-
P10	1621.2	1556.249
P11	485.6608	172.4

The correlation plot (**Figure 70**) demonstrates that the GC-LSPR biosensor can serve as a robust alternative to ELISA, with the added advantages of real-time monitoring, label-free detection, and reduced assay complexity.

Unlike ELISA, which requires multiple hours to complete, the biosensor delivers results within minutes, using smaller sample volumes and fewer reagents. This capability aligns with the increasing demand for decentralized testing and rapid diagnostic tools for immune-mediated diseases [40,60].

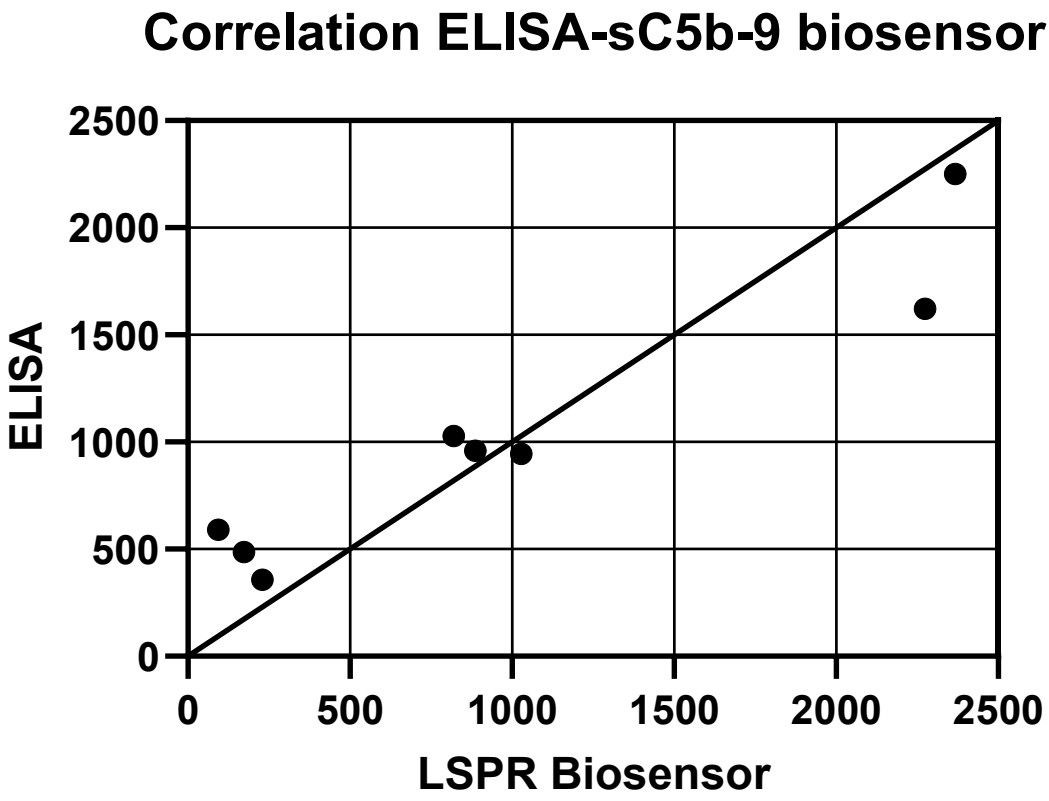


Figure 70. *Correlation of ELISA vs. GC-LSPR biosensor in patient serum samples. Each point represents an individual sample (n=11).*

The improved sensitivity of GC-LSPR is attributable to the enhanced local electromagnetic field around the BD-derived nanogratings, which amplifies RI changes caused by protein binding events. Furthermore, the oriented immobilization strategy using cys-Protein G ensures optimal antibody orientation, maximizing binding efficiency and reducing steric hindrance, which can otherwise limit sensitivity in antibody-based assays [126].

A comparison of both methods is presented in **Table 15**. ELISA remains advantageous for standardized, high-throughput applications but requires long incubation times, multiple washing steps, and relatively large sample volumes.

Table 15. *Comparison table of both ELISA and GC-LSPR biosensor detection techniques.*

Feature	ELISA	GC-LSPR Biosensor (this work)
Detection principle	Label-based, enzymatic colorimetric readout	Label-free, RI change at plasmonic surface
LOD	2.54 ng/mL (this study)	0.015 ng/mL (this study)
Dynamic range	31.25-2000 ng/mL	0.97-1500 ng/mL
Assay time	4-5 h (multiple incubation & washing steps)	<30 min (real-time, single-step injection)
Sample volume	50-100 µL per well	200 µL per biosensor
Matrix tolerance	Requires dilution	Requires dilution and blocking
Specificity	cross-reactivity may cause false positives	Extremely specific
Operational complexity	Multi-step protocol	Minimal handling
Throughput	High (96-384 well plates)	Moderate (dual-channel chip)
Clinical applicability	Standardized, regulatory accepted	Emerging

It is interesting to note that in three patient samples (P7-P9), all of which were MuSK-antibody-positive but AChR-negative, where ELISA reported measurable sC5b-9 concentrations (18-25 ng/mL) while the LSPR biosensor showed no detectable response.

MuSK-MG is primarily mediated by IgG4 antibodies and is considered non-complement activating, making the LSPR results biologically plausible and in line with current understanding of disease pathophysiology [18,146]. In contrast, ELISA assays, although extremely sensitive, may be prone to false positives due to cross-reactivity or pre-analytical complement activation during serum handling [147]. Furthermore, ELISA relies on long incubation times and a two-site capture system that can amplify weak or nonspecific binding events, whereas the LSPR biosensor detects only real-time surface interactions with oriented antibodies, thus offering higher specificity against artifactual signals.

These findings underscore a critical advantage of nanoplasmonic sensing: by directly monitoring binding kinetics in a label-free format, it discriminates true complement activation events from background or nonspecific signals. Therefore, while ELISA suggested residual sC5b-9 activity in MuSK-positive patients, the absence of signal in the biosensor more accurately reflects the expected biological profile, highlighting the potential of LSPR to serve as a clinically relevant and more specific tool for complement activation assessment in Myasthenia Gravis.

In summary, the GC-LSPR biosensor not only achieves comparable accuracy to ELISA but surpasses it in sensitivity and operational simplicity. This positions it as a promising candidate for clinical diagnostics, especially in scenarios where rapid assessment of complement activation could aid disease monitoring and therapeutic interventions in Myasthenia Gravis and other complement-mediated disorders. Future studies should expand the sample cohort, assess intra- and inter-assay variability, and evaluate performance in minimally processed clinical samples to further strengthen the clinical utility of this biosensing platform.

4.12 COMPARATIVE ANALYSIS

GC-LSPR biosensors demonstrate several advantages over traditional analytical techniques such as ELISA or RIPA. Unlike conventional assays, which require labels, secondary antibodies, or radioactive isotopes, LSPR sensors provide real-time visualization of biomolecular interaction events directly on the sensor surface. This eliminates additional detection steps, thereby reducing complexity, assay time, and potential sources of error [74,81].

A typical LSPR assay can be finalized in 20-30 minutes, whereas ELISA protocols often require several hours due to multiple incubation, washing, and amplification steps. RIPA, although sensitive, is highly restricted in routine clinical use because of its reliance on radioisotopes, specialized disposal, and safety regulations [148,149]. Thus, the biosensor

format offers both faster turnaround time and safer handling conditions, important parameters for integration into point-of-care or near-patient diagnostics.

From a cost perspective, LSPR platforms are relatively affordable compared to other high-resolution optical detection systems. A laboratory-scale LSPR platform can be assembled in the range of €50,000-€150,000, depending on optical complexity and multiplexing features. In contrast, ELISA readers typically cost €10,000-€30,000, but the recurring cost per assay is considerably higher due to the need for enzyme-conjugated antibodies, chromogenic substrates, and disposable plates [145]. RIPA infrastructure costs are comparable to ELISA, but the maintenance, safety requirements, and radiolabel-associated consumables make it substantially more expensive in long-term use [74].

Although this technology is still under development, we conducted a preliminary cost analysis per fabricated sensor chip. While we acknowledge that industrial-scale costs will fluctuate depending on large-scale manufacturing and integration with standardized microfluidic cartridges, our analysis provides an approximate estimate of the consumables required per sensor. The breakdown is shown in **Table 16**. These numbers highlight the potential of this technology to become an easy-to-use, rapid, and affordable diagnostic tool, particularly when compared with the per-test reagent costs of ELISA, which can range between €500-750 per kit.

***Table 16**. Cost per-sensor chip fabrication.*

Item or component	Cost per-sensor chip (€)
Coupler protein	0.03
Detection antibody	0.12
Polymer brushes	0.04
Gold deposition	7.40
Substrate material (Blu-ray) and CNC cutting	0.30
Total	7.90

This analysis suggests that, despite higher initial equipment costs, LSPR biosensors could achieve significantly lower per-test costs than ELISA once fabrication is standardized. Additionally, because the sensors are reusable to a limited extent after regeneration, the effective cost per analysis could be further reduced. This economic feasibility, combined with their rapid and label-free nature, supports their potential role as an alternative or

complementary platform to ELISA and RIPA in clinical and translational research environments.

4.13 Clinical Relevance of Biosensor Performance Compared to ELISA

Conventional ELISA remains the current gold standard for complement biomarker detection in clinical settings, offering high specificity and established clinical acceptance. However, ELISA requires lengthy incubation times, skilled personnel, and centralized laboratory facilities, which restrict its suitability for rapid decision-making in clinical practice. In contrast, the nanoplasmonic biosensor developed in this work demonstrated superior sensitivity, with a limit of detection as low as 0.015 ng/mL, while also achieving rapid and label-free analysis from minimal serum volumes. These features make the biosensor particularly advantageous for scenarios where timely information is critical, such as monitoring disease activity during outpatient visits or adjusting complement inhibitor therapy.

From a patient management perspective, the ability to perform near real-time monitoring of sC5b-9 could provide clinicians with actionable insights into complement activation status. In AChR+ MG, where complement activation drives pathology, this platform could help early detection of disease and enable more precise dosing strategies for complement-targeted treatments. Moreover, the absence of complement activation in MuSK+ patients, as confirmed by the biosensor, reinforces its potential role in guiding therapeutic stratification and avoiding unnecessary interventions.

Beyond its diagnostic performance, the biosensor also presents significant cost and workflow advantages. Its fabrication relies on low-cost, disposable nanograting substrates, offering scalability that contrasts with the batch-based, resource-intensive nature of ELISA. Minimal sample pretreatment and short assay times (<30 minutes) further reduce the burden on clinical staff and healthcare systems. Together, these attributes position the biosensor not as a replacement but as a complementary tool to ELISA: while ELISA may continue to serve in centralized confirmatory testing, the biosensor offers a unique opportunity to extend diagnostic capacity to POC environments, thereby supporting personalized and responsive patient care in MG.

4.14 Limitations and Future Directions

While this thesis demonstrates the feasibility and clinical relevance of a nanoplasmonic biosensor for complement activation monitoring in Myasthenia Gravis (MG), several limitations must be acknowledged. First, validation was performed on a limited number of patient samples, which restricts the generalizability of the findings. Larger, studies will be required to confirm the diagnostic accuracy, reproducibility, and robustness of this biosensor across diverse patient populations and disease severities. Second, the current assay relied on diluted serum samples to minimize matrix effects. Although effective, this step reduces clinical practicality, and further optimization of antifouling strategies and fluidic handling will be necessary to enable direct serum analysis. Third, variability in

sC5b-9 levels among individuals and across various stages of disease progression was not fully addressed, highlighting the need for longitudinal studies to establish the biomarker's prognostic and monitoring value. Finally, while comparisons with ELISA underscored the superior sensitivity and rapidity of the biosensor, more comprehensive benchmarking against current clinical assays would strengthen the case for translation.

Integration with microfluidic systems could allow automated sample handling, on-chip mixing, and real-time kinetic analysis, further simplify workflows, and reduce operator dependence. Expanding the biosensor platform to enable multiplex detection of MG-relevant biomarkers, such as AChR and MuSK autoantibodies alongside sC5b-9, would provide a more holistic diagnostic tool and enhance patient stratification. Beyond MG, the approach is readily adaptable to other complement-mediated autoimmune and inflammatory disorders, extending its potential clinical utility. Finally, miniaturization and coupling with portable readout systems could pave the way for point-of-care diagnostics, supporting precision medicine strategies and making advanced biosensing accessible in routine clinical practice.

CHAPTER 5 | CONCLUSIONS

In this thesis, we developed and validated an extremely sensitive, rapid, and label-free plasmonic biosensor based on nanograting technology for the detection and quantification of the soluble terminal complement complex (sC5b-9) in human serum. The platform demonstrated a remarkably low limit of detection of 0.015 ng/mL, surpassing the sensitivity of conventional assays such as ELISA and RIPA. Importantly, it requires only minimal sample volumes, simple dilution steps, and short assay times, significantly streamlining sample processing and reducing overall analysis time. The biosensor chip fabrication, derived from cost-effective and scalable nanostructured Blu-ray disc substrates, positions this technology as both accessible and disposable, facilitating translation into point-of-care diagnostics.

A critical contribution of this work is the establishment of a robust surface biofunctionalization strategy using cys-Protein G to ensure optimal antibody orientation and recognition capacity. Complemented by optimized antifouling coatings and dilution protocols, this approach enabled dependable biosensing in complex matrices such as human serum, overcoming a major barrier for label-free optical biosensors. While some background noise persisted, the results demonstrate that further refinement of antifouling techniques could eliminate this limitation, paving the way for even more robust performance.

The biosensor was clinically validated using real patient serum samples, demonstrating the ability to differentiate between AChR+ and MuSK+ Myasthenia Gravis subtypes. The sensor successfully identified complement activation in AChR+ MG patients, consistent with their known immunopathology, while showing no activation in MuSK-positive cases. These findings confirm the value of sC5b-9 as a biomarker for complement-driven pathology in MG and underline the diagnostic and monitoring potential of this biosensing approach. In the context of emerging complement-targeted therapies, the ability to rapidly monitor complement activity in serum provides an avenue for patient stratification, treatment optimization, and personalized therapeutic guidance.

Beyond MG, the methodological advances presented here, ranging from nanostructure-based plasmonic sensing to antibody immobilization strategies, establish a generalizable framework for the development of next-generation biosensors targeting other complement-mediated and autoimmune disorders. The convergence of high sensitivity, cost-efficient fabrication, and potential for miniaturization supports the vision of plasmonic biosensors as transformative tools in clinical diagnostics.

Nevertheless, this work also highlights future challenges and opportunities. Current assays relied on diluted serum samples; future iterations integrating microfluidic mixing and enhanced antifouling strategies could enable direct serum analysis, further increasing clinical utility. Additionally, large-scale clinical validation studies across diverse patient cohorts will be necessary to confirm diagnostic accuracy, reproducibility, and robustness under real-world conditions. The incorporation of multiplexing capabilities could further

expand the biosensor's scope, allowing simultaneous monitoring of multiple biomarkers relevant to MG and related conditions.

In summary, this thesis contributes to bridging a critical diagnostic gap in Myasthenia Gravis by presenting a novel, label-free nanoplasmonic biosensor for complement activation monitoring. By combining technological innovation with clinical validation, it lays the groundwork for implementing rapid, sensitive, and accessible tools to support personalized medicine in MG. Ultimately, the advancements reported here may serve not only to improve disease management in MG but also to catalyze broader applications in precision diagnostics for autoimmune and inflammatory diseases.

ANNEX

***Table A 1**. Chemicals and bioreagents used in this study*

Item	Specification / Notes	Supplier (Location)
Hydrochloric acid (HCl), 37%	Substrate cleaning (protective/reflective layer removal)	VWR International Eurolab
Hellmanex® III	Detergent	Sigma-Aldrich
Glacial acetic acid (CH_3COOH)	20% (ultrasonication step)	Panreac AppliChem
2-propanol	Substrate cleaning	ITW Reagents
PBS tablets (pH 7.4)	0.01 M phosphate; 0.0027 M KCl; 0.137 M NaCl	Sigma-Aldrich
Sodium acetate buffer (SAB)	pH 4-6 (used at pH 4 for immobilization)	Sigma-Aldrich
Tween®-20	Surfactant	Sigma-Aldrich
CHAPS	3-[(3-Cholamidopropyl)dimethylammonio]-1-propanesulfonate hydrate	Sigma-Aldrich
Glycine buffer	pH 2.2	Sigma-Aldrich
BSA (bovine serum albumin)	1% (blocking)	Sigma-Aldrich
PLL20-g(30)-MPEG45 (PLL-PEG)	0.75 mg/mL	NanoSoft Biotechnology
Recombinant cys-Protein G		ProSpec
Mouse anti-human SC5b-9 antibody	—	Bio-Rad Laboratories
Human complement sC5b-9 complex	—	Novus Biologicals

Purified rat anti-mouse IL-6 antibody	—	BD Pharmingen™
Recombinant mouse IL-6	—	BD Pharmingen™
Commercial human serum (CHS)	—	Merck Life Science

***Table A 2**. Substrates and microfluidic/optical consumables*

Item	**Specification / Notes**	**Supplier**	**Catalog / Model**	**Use in study**
Blu-ray discs (BD-R SL 25 GB)	Polycarbonate (PC) nanogratings	Verbatim	43742	Nanostructured substrate
Matte removable vinyl	Deposition mask	Silhouette	V12-BMR-DKGRN	Define sensing area
Double-sided adhesive tape	140 µm thickness	Adhesive Research	ARcare® 90106NB	Microfluidic spacer
PMMA sheet	2 mm thickness	Servei Estació	37.60 mm x 16 mm rectangles	Optical lid
PTFE tubing	I.D.×O.D. 0.8×1.58 mm	Sigma-Aldrich	Z609714	Fluidic connections
Mini Luer tube tuck connectors	For 1/16″ tubing	ChipShop	Fluidic 1579	Chip-tubing interface
Custom 3D-printed holders/lids	—	In-house	—	Chip fixation and alignment

***Table A 3.** Instruments, software, and key equipment.*

System / Instrument	Specification / Notes	Manufacturer	Model / Software

CNC router	Chip cutting	Genmitsu	3020-PRO MAX V2
Thermal evaporator	Au deposition, 10^{-7} mbar, 1 Å/s	Oerlikon Leybold	Univex 450B
SEM	Surface/nanostructure imaging	FEI Company	Nova NanoSEM
CO_2 laser cutter	PMMA lid machining	Omtech	K40+
Plotter	Vinyl/tape cutting	Silhouette	Cameo 4
Light source	360-2400 nm	Ocean Optics	HL-2000
Spectrometer	480-995 nm	Avantes	AvaSpec-NEXOS™
Syringe pump	Fluid delivery	KD Scientific	KDS 101-CE
Injection valve	Manual, 6-port, 200 µL loop	Valco Instruments Co.	Cheminert C22-3186
Bubble trap	—	Elveflow	—
Vacuum pump	Bubble management	SparkFun Electronics	—
Motorized linear stage	Opto-mechanical alignment	Zaber Technologies	T-LSM025A
Translation/rotation stage	Fine alignment	Thorlabs	XYR1/M
CAD / CAM	Design and cutting control	Autodesk / Silhouette / LightBurn / Candle	Inventor / Fusion 360 / LightBurn / Silhouette Studio / Candle
Simulation	Flow simulation	COMSOL	Multiphysics® (Laminar Flow)
Control & DAQ	Sensing control	National Instruments	LabVIEW (custom UI)

Data analysis	Curves and stats	GraphPad / Origin / Microsoft	Prism 10 / Origin 8.0 / Excel

Table A 4. *Comparison table of commercially available detection kits for sC5b-9.*

Detection Method for sC5b-9	Detection range	LOD	Sensitivity	Source
ELISA	31.25 - 2000 ng/mL	31.25 ng/mL	18.75 ng/mL	Novus Biologicals, NBP2-66708
ELISA	12.5-800 ng/ml	12.5 ng/mL	7.5 ng/ml	Fine Biotech Co., Ltd., EH4763
ELISA	N/A	3.7 ng/mL	N/A	MicroVue™, A020
ELISA	1.25 - 80 ng/ml	1.25 ng/mL	0.51 ng/ml	Krishgen Biosystems, KBH4499
ELISA	72.0 - 244.0 ng/mL	72.0 ng/mL	N/A	Advanced Diagnostic Laboratories, SC5B9
ELISA	6.25 - 200 ng/ml	6.25 ng/mL	1.0 ng/mL	MyBioSource, MBS9369739
RIPA (can be modified for sC5b-9)	0.5 - 5 nmol/L	0.02 nmol/L	N/A	DLD Diagnostika GmbH
CBA (HEK293T)	Cutoff for positivity: 156 ± 14 MFI	N/A	N/A	Obaid, et al. (2022) [150]

Table A 5. *Affinity of Protein G for IgG Types from Different Species. Adapted from New England Biolabs, 2025.*

Species	Immunoglobulin	Binding to Protein G
Human	lgG (normal)	++++
	lgG1	++++
	lgG2	++++
	lgG3	++++
	lgG4	++++

	lgM	-
	lgA	-
	lgE	-
Mouse	lgG1	++++
	lgG2a	++++
	lgG2b	+++
	lgG3	+++
Rat	lgG1	+
	lgG2a	++++
	lgG2b	++
	lgG2c	++
Goat	lgG	++
Rabbit	lgG	+++
Sheep	lgG	++

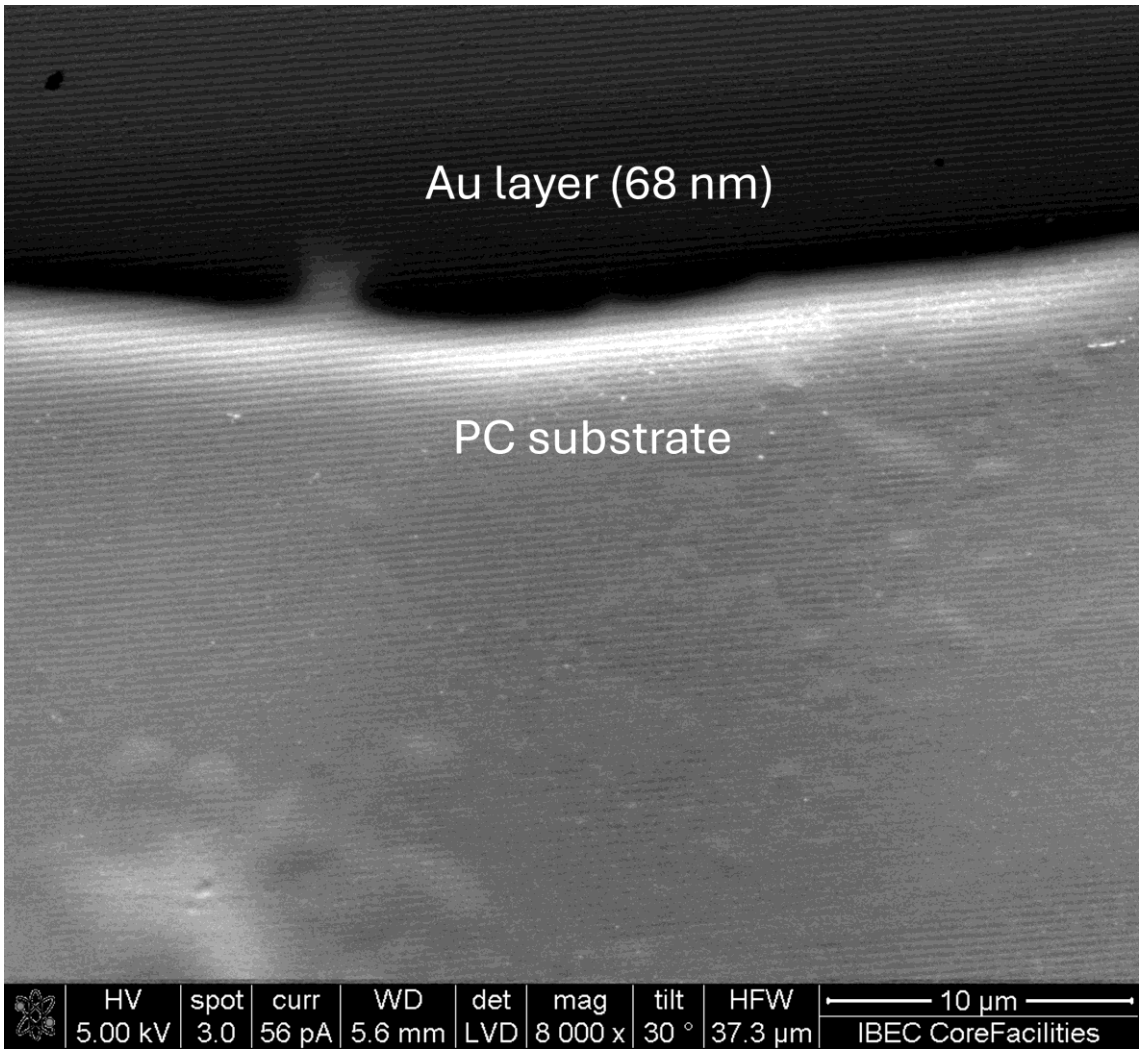


Figure A1. SEM image of a chip with Au layer (68 nm) taken at the border where the PC substrate can also be observed. Nanoslits are visible in the Au layer and the PC substrate.

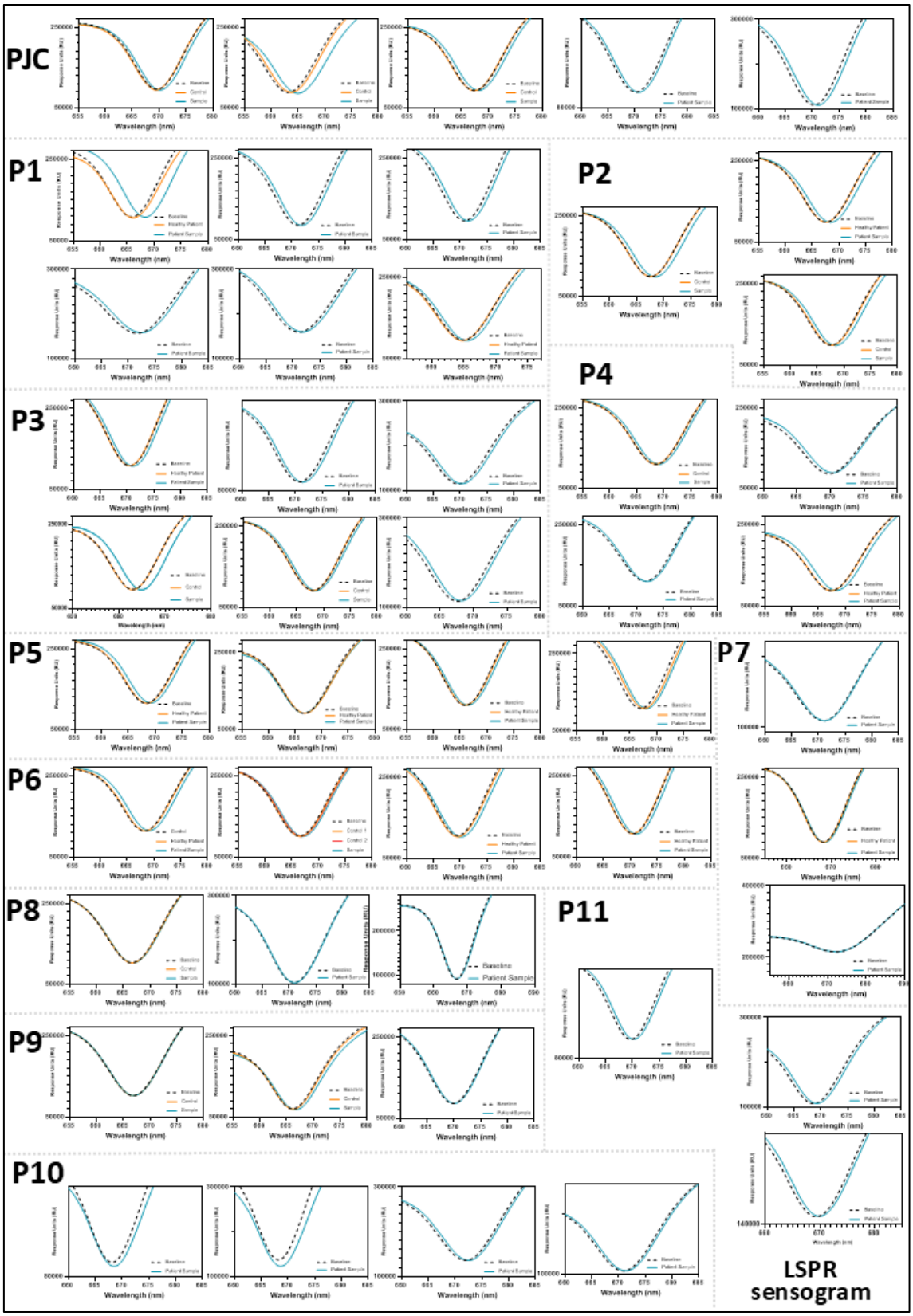


Figure A2. Plasmon peak shift of the diluted serum of 11 patients with myasthenia gravis in the biosensor.

LIST OF PUBLICATIONS

Ugarte-Orozco, M. J., López-Muñoz, G. A., Antonio-Pérez, A., Esquivel-Ortiz, K. M., & Ramón-Azcón, J. (2023). **High-throughput biointerfaces for direct, label-free, and multiplexed metaplasmonic biosensing**. *Current Research in Biotechnology*, *5*, 100119. https://doi.org/10.1016/J.CRBIOT.2023.100119

LIST OF TABLES

Table 1. Summary different systematic reviews statistics for estimated MG prevalence and incidence. 1

Table 2. Comparison between MG diagnostic methods and some of their advantages and limitations. 13

Table 3. Comparison of sensitivity in GC biosensors. 20

Table 4. Comparison between main plasmonic sensing modalities. 22

Table 5. Refractive Index values of the HCl solutions used in the bulk calibration of the sensor chips. 53

Table 6. Refractive index (RI) of HCl solutions used for bulk calibration (reference η_0 = 1.3325). 84

Table 7. Comparison of bulk refractive index detection limits of grating-coupled plasmonic sensors. 86

Table 8. Summary of biosensor response shifts ($\Delta\lambda$, nm) at different serum dilutions, comparing commercial serum alone and commercial serum spiked with protein sC5b-9. 95

Table 9. Analytical parameters for the calibration curve in cell culture media using 5PL fitting. 98

Table 10. Sensor response per concentration of sC5b-9. 99

Table 11. Analytical parameters for the biosensor assay using 4PL fitting. 101

Table 12. Key parameters of the calibration curve for sC5b-9 conducted in diluted CHS*. 102

Table 13. Key parameters of the diluted serum of 11 patients with myasthenia gravis* in the biosensor. 105

Table 14. Comparison of sC5b-9 quantification by ELISA and GC-LSPR biosensor in patient serum samples (1:100 dilution). 107

Table 15. Comparison table of both ELISA and GC-LSPR biosensor detection techniques. 109

Table 16. Cost per-sensor chip fabrication. 111

Table A 1. Chemicals and bioreagents used in this study 118

Table A 2. Substrates and microfluidic/optical consumables 119

Table A 3. Instruments, software, and key equipment. 119

Table A 4. Comparison table of commercially available detection kits for sC5b-9. 121

Table A 5. Affinity of Protein G for IgG Types from Different Species. Adapted from New England Biolabs, 2025. 121

LIST OF FIGURES

Figure 1. Schematic overview of normal neural neuromuscular junction (NMJ) and immunopathogenesis of myasthenia gravis (MG). 4

Figure 2.Schematic representation of the complement cascade. 6

Figure 3. Testing algorithm for AChR antibody detection. 10

Figure 4. Schematic representation of the basic components of a biosensor including the sample, the bioreceptor, the transducer, and the data processing for signal monitoring. 14

Figure 5. Examples of biorecognition mechanisms. (a) catalytic biosensor (enzyme-based), (b) affinity biosensor (antibody, DNA, receptor). 16

Figure 6. Schematic representation of wavelength shift (Δλ, nm); (a) plasmon shift in surface plasmon resonance, (b) real-time sensogram of wavelength shift. 19

Figure 7. Schematic representation of sensing principle for (a) bulk sensitivity and (b) surface sensitivity. 19

Figure 8. Representation of the main types of biofunctionalization methods: (a) direct immobilization;(b) covalent binding to a self-assembled monolayer (SAM); (c) polymer matrix entrapment; (d) affinity immobilization through protein-antibody binding. 24

Figure 9. Schematic representation of SPR coupling methods: (a) prism coupling; (b) grating coupling; (c) waveguide coupling. 26

Figure 10. Schematics representation of a GC-SPR biosensing configuration when TM polarized light is used. 27

Figure 11. Different immunoassay configurations: (a) direct competitive, (b) indirect competitive, (c) direct non-competitive, and (d) indirect non-competitive. 29

Figure 12. Antibody different possible orientations on a surface. Tail-on, flat-on, head-on and side-on orientations. 30

Figure 13. Schematic representation of a basic structure of an antibody. 31

Figure 14. Schematic representation of the structure of commercial optical discs, including the optical and physical parameters. Indicated dimensions are track pitch (p) and groove height (h). 33

Figure 15. Scheme of the BD disc structure: (i) disc label; (ii) polycarbonate layer (1.1 mm thick disc); (iii) reflective layer; (iv) protective layer; (v) cover layer. 34

Figure 16. Schematic representation of the experimental pipeline of the biosensor. 41

Figure 17. CAD design of the 3D-printed support used for the CNC router cutting of Blu-ray chips. (a) Cutting pattern, (b) Top view, (c) Side view, and (d) Mounted on the CNC machine. Candle Software user interface. 42

Figure 18. Vinyl-masked chip before and after gold deposition. 43

Figure 19. CAD design of the microfluidic channel architecture created in Autodesk Inventor Professional®. 44

Figure 20. COMSOL Multiphysics® interface showing flow simulations within the microfluidic layout. 45

Figure 21. Silhouette Studio interface for configuring plotter parameters and visualizing the cutting path. 45

Figure 22. LightBurn software user interfaces with the preview of the patterned lid and the parameter selection and on the bottom the laser cutter setup. 46

Figure 23. Expanded view of the sensor assembly: a) PMMA Lid, b) Double-sided tape microfluidics (140 µm), c) Au-coated PC substrate (68 nm), d) Final assembled sensor. 47

Figure 24. Overview of the fabrication and assembly workflow: a) PC substrate, b) Vinyl masking, c) Gold deposition, d) Adhesive layer integration, and e) Final chip. 48

Figure 25. A schematic representation of the optical sensing platform. 49

Figure 26. General overview of the experimental LSPR sensor setup with the microfluidic system and opto-mechanical system. 50

Figure 27. Schematic representation of the fixation lid and the microfluidic connected chip on the platform holder. A) chip with luer connectors on the platform holder, b) positioning of the lid and the connected chip, c) side view of the lid chip connecting sequence. 51

Figure 28. LabView software user interface. A) Spectrometer and Fitting tab to allow parameter selection and customization and b) Sensing tab to visualize real-time data point collection. 52

Figure 29. Schematic representation of the biofunctionalization technique ex situ of the sensor surface. Created in BioRender. Ugarte Orozco, M. (2025) https://BioRender.com/orlbaea 57

Figure 30. First design of the nanoplasmonic chip with two sensing spots in one single microfluidic channel. 64

Figure 31. Design of the sensing flow with continuous sensing spots ("Zone 1" and "Zone 2") in a single microfluidic channel. 65

Figure 32. Result from sensograms (n=5) measurement of concentration curve of IL-6. 65

Figure 33. Panels (a-c) show SEM imaging of polycarbonate substrate after protective-layer removal using protocol v1.0 (1 M HCl, 24 h at 40 °C; brief sonication). Panels (d-f) show SEM imaging of sensors after Au film deposition (68 nm). Panels (g-i) show Au surface in microscopy. Scale bars as indicated. 67

Figure 34. Photograph of 'Scoth tape test' after the Au film deposition (68 nm) on PC substrate with cleaning protocol v1.0. 68

Figure 35. Panels (a-c) show SEM imaging of Blu-ray-derived polycarbonate after improved protective-layer removal (protocol v2.0: 37% HCl, 1 h, 40 °C → 1 M HCl, 48 h, 40 °C; sequential ultrasonication in 20% acetic acid, water, 1% Hellmanex®, isopropanol; N_2 dry). Scale bars as indicated. 68

Figure 36. Photographs of lot-dependent Au film failure and loss of plasmonic response. Left, top: assembled chip showing particulate contamination and label flaking. Left, bottom: two substrates after Au evaporation; the upper chip exhibits a rough, matte, non-uniform film, and the lower chip shows partial delamination—both incompatible with reliable optics. Right: reflected spectrum acquired under standard conditions; the trace lacks a distinct LSPR plasmon, consistent with poor coupling caused by the rough/flaking Au layer. 69

Figure 37. Catalog consistency issue and lot effects on substrate quality. Left: example listing for Verbatim BD-R SL 6 x 25 GB (cat. 43743) "Wide White Thermal Printable, no ID." Right: packaging from the received lot labeled BD-R DL 6 x 25 GB but bearing the same catalog number (43743). The DL construction adds extra functional and protective layers that hinder complete removal by the established acid protocol and, together with label flaking, lead to roughened PC surfaces and poor Au deposition..... 70

Figure 38. Photograph of 'Scoth tape test' after the Au film deposition (68 nm) on PC substrate with cleaning protocol v2.0 in BD-R DL derived substrates. 70

Figure 39. Panels (a-c) show SEM imaging of polycarbonate substrate after protective-layer removal using protocol v2.0 (37% HCl, 1 h, 40 °C → 1 M HCl, 48 h, 40 °C; sequential ultrasonication in 20% acetic acid, water, 1% Hellmanex®, isopropanol; N_2 dry). Panels (d-f) show SEM imaging of sensors after Au film deposition (68 nm). Panels (g-i) show Au surface in microscopy. Scale bars as indicated. 71

Figure 40. Cleaning protocol v2.0 applied to BD-R SL (Verbatim 43742). Left: PC substrate after stripping shows micro-roughness/pitting. Right: Au-coated chips also has roughness/pitting. 72

Figure 41. Panels (a-c) show SEM imaging of polycarbonate substrate after protective-layer removal using protocol v3.0 (0.75 M HCl for 24 h at 40 °C; sequential ultrasonication in 20% acetic acid, water, 1% Hellmanex®, isopropanol; N_2 dry). Panels (d-f) show SEM imaging of sensor after Au film deposition (68 nm). Panels (g-i) show Au surface in microscopy. Scale bars as indicated..... 73

Figure 42. Periodicity (P=320 nm) calculated from the SEM imaging of the nanoslits. 74

Figure 43. Comparative characterization of three cleaning protocols and their impact on substrate and optical performance. **(a)** Protocol v1.0 (1 M HCl, 24 h, 40 °C) on printable BD-R SL (cat. 43743): lower LSPR reflectance peak; SEM (PC pre-Au) shows Ag-alloy/label residues; SEM (post-Au) shows roughness and particles; Microscopy shows scratches on the gold surface and debris. **(b)** Protocol v2.0 (37% HCl, 1 h → 1 M HCl, 48 h; 40 °C) on BD-R DL (43743): reflectance peak is not present; SEM (PC pre-Au) shows over-etched texture; SEM (post-Au) shows roughness, not clear deposition; Microscopy shows damaged surface and indicates poor film quality. **(c)** Protocol v3.0 (0.75 M HCl, 24 h, 40 °C) on BD-R SL (43742): strong, well-defined LSPR reflectance peak; SEM (PC pre-Au) shows clean nanoslit grating with minimal debris; SEM (post-Au) shows smooth, continuous film; Microscopy uniform, mirror-like Au. Scale bars as indicated. 75

Figure 44. Photograph of 'Scoth tape test' after the Au film deposition (68 nm)..... 76

Figure 45. Reproducibility evaluation of the fabrication process. Sensograms of n=9 different sensors with a 68 nm Au layer from three different fabrication batches. 77

Figure 46. COMSOL velocity magnitude (m/s) and streamline profile: velocity field of the single channel microfluidic design. 78

Figure 47. COMSOL velocity magnitude (m/s) and streamline profile. A) 1 mm parallel-channel split at 40º, b) 1 mm parallel-channel split at 90º, c) 1 mm parallel-channel split at 60 º, d) 1 mm parallel-channel split at 60º with straight channel for inlet/outlet. 80

Figure 48. Velocity field magnitude (mm/s) of the cross-sections. A) The velocity field at the inlet, b) the velocity field of both channels, c) the velocity field of the sensing chamber. 81

Figure 49. Photograph of the initial sensing platform (v1). Left: low-flow peristaltic pump (LabV1). Right: fixed-angle opto-mechanical stage with chip holder; labeled "Injection" indicates the sample inlet; "Waste" indicates the outlet. In this configuration, spectra were acquired at discrete timepoints via BW-Spec software, which allowed Δλ tracking but not continuous, synchronized, real-time acquisition. 82

Figure 50. Photograph of the real-time sensing platform (v2). In this configuration, spectra were acquired via LabVIEW software, which allowed Δλ tracking real-time acquisition. 83

Figure 51. Bulk calibration sensogram. (a) Real-time measurement of wavelength shifts (Δλ, nm) caused by subsequent injections of decreasing HCl concentrations in time (s). (b) wavelength displacement shifts (Δλ, nm) of decreasing HCl concentrations. 83

Figure 52. Bulk sensitivity of the GC-LSPR sensor. (a) Calibration curves from 10 bulk calibrations $\Delta\lambda \; vs \; \Delta n$; (b) mean calibration curve, the slope corresponds to $SB = 328.6 \; nm/RIU$. Each measurement corresponds to the mean ± σ of the measurements. 84

Figure 53. Noise level estimation from the baseline sensor response. 85

Figure 54. Schematic illustration of the immobilization mechanism of cys-Protein G onto the gold surface. (Left) The protein tagged with the cysteine and its terminal thiol group (-CH_2-SH) into proximity of the gold surface. (Right) The oxidative addition drives the cleavage of the S-H bond, resulting in the loss of a proton (H^+) and the formation of covalent bond of Au-S-Protein. 88

Figure 55. Effect of the pH and concentration in the immobilization-response of the biosensor (a) Plot demonstrates cys-Protein G attachment efficiency to the surface with different pH values. (b) Plot demonstrating different concentrations of cys-Protein G and IgG antibody to determine most efficient working conditions. (c) Curve displacements of different antibody concentrations by monitoring the shifts in the plasmonic band position (Δλ, nm). 89

Figure 56. Real-time sensogram showing the response of a biosensor surface treated with 0.75 mg/mL PLL-PEG after the injection of 1% BSA. A residual shift (Δλ = 0.23 nm) indicates partial non-specific adsorption. 90

Figure 57. Sensogram showing the biosensor response with anti-C5b-9 after anti-fouling treatment with 0.75 mg/mL PLL-PEG + 1% BSA. No shift was observed after injecting IL-6 (100 ng/mL), while a specific signal was recorded after serial injection of sC5b-9. 91

Figure 58. Sensogram peak shift response in wavelength (Δλ, nm) of the biosensor when performing the biofunctionalization of cys-Protein G and Ab C5b-9 onto the surface and its response to sC5b-9 (250 ng/mL). 91

Figure 59. Comparison of real-time biosensor response to 100 ng/mL of recombinant sC5b-9 after storage at 4 °C for 48 hours, 22 days, and 30 days under two different conditions. Left panel: biosensors stored dry. Right panel: biosensors stored submerged in PBS buffer. Sensor performance is evaluated based on peak response intensity and dissociation stability. 93

Figure 60. Baseline response of different dilutions of commercial human sera (1:100, 1:50, 1:10, and 1:1) attachment before and after regeneration with Glycine. Showing the highest signal Δλ = 2.75 nm for 1:1. 94

Figure 61. Biosensor response to different serum dilutions comparing commercial serum alone and commercial serum spiked with recombinant protein sC5b-9 = (250 ng/mL). 95

Figure 62. Schematic representation of one spot functionalized with cys-Protein G + BRE (Ab C5b-9); while the control spot was only functionalized with cys-Protein G. 96

Figure 63. Real-time sensogram response of the biosensor with two channels. Blue line: Spot functionalized with cys-Protein G + BRE (Ab C5b-9). Orange line: Spot functionalized only with cys-Protein G (control). 97

Figure 64. Dose-response curve showing LSPR wavelength shift (Δλ, nm) against increasing concentrations of recombinant sC5b-9. Curve was fitted using a 4PL model. LOD was calculated as 0.1618 ng/mL. 99

Figure 65. Calibration curve fitted to a simple regression line..... 100

Figure 66. Dose-response curve showing LSPR wavelength shift (Δλ, nm) against increasing concentrations of recombinant sC5b-9 in diluted CHS. Curve was fitted using a 4PL model. LOD was calculated as 0.015 ng/mL. 101

Figure 67. Real-time sensogram showing (a) CHS baseline, (b) PBST 1% wash, (c) healthy patient serum sample (1:100), (d) MG patient serum sample (1:100) and (e) PBST 1% wash. The shift in plasmon peak (Δλ, nm) confirms detection of sC5b-9 in the patient sample. 103

Figure 68. Bar graph comparing calculated sC5b-9 concentrations in 11 patient serum samples. Patients P7, P8, and P9 are MuSK-positive; others are AChR+. 105

Figure 69. Calibration curve of human sC5b-9 measured by ELISA. The limit of detection (LOD) was determined to be 2.54 ng/mL. 107

Figure 70. Correlation of ELISA vs. GC-LSPR biosensor in patient serum samples. Each point represents an individual sample (n=11). 108

BIBLIOGRAPHY

1. Sciancalepore F, Lombardi N, Valdiserra G, Bonaso M, Cappello E, Hyeraci G, et al. Prevalence, Incidence, and Mortality of Myasthenia Gravis and Myasthenic Syndromes: A Systematic Review. Neuroepidemiology. 2024;1–14. doi:10.1159/000539577 PubMed PMID: 39380477.

2. Bubuioc AM, Kudebayeva A, Turuspekova S, Lisnic V, Leone MA. The epidemiology of myasthenia gravis. J Med Life. 2021;14(1):7–16. doi:10.25122/JML-2020-0145, PubMed PMID: 33767779.

3. García-Estévez DA, Fraga-Bau A, García-Sobrino T, Mederer-Hengstl S, Pardo-Fernández J. Epidemiología de la miastenia grave en la península ibérica y Latinoamérica. Rev Neurol. 2023;76(2):59. doi:10.33588/RN.7602.2021201 PubMed PMID: 36631965.

4. Wartmann H, Hoffmann S, Ruck T, Nelke C, Deiters B, Volmer T. Incidence, Prevalence, Hospitalization Rates, and Treatment Patterns in Myasthenia Gravis: A 10-Year Real-World Data Analysis of German Claims Data. Neuroepidemiology. 2023 May 1;57(2):121. doi:10.1159/000529583 PubMed PMID: 36807212.

5. Santos E, Coutinho E, Moreira I, Silva AM, Lopes D, Costa H, et al. Epidemiology of myasthenia gravis in Northern Portugal: Frequency estimates and clinical epidemiological distribution of cases. Muscle Nerve. 2016 Sep 1;54(3):413–21. doi:10.1002/MUS.25068;PAGEGROUP:STRING:PUBLICATION PubMed PMID: 26851892.

6. Rodrigues E, Umeh E, Aishwarya, Navaratnarajah N, Cole A, Moy K. Incidence and prevalence of myasthenia gravis in the United States: A claims-based analysis. Muscle Nerve. 2024 Feb 1;69(2):166–71. doi:10.1002/MUS.28006 PubMed PMID: 38040629.

7. Dresser L, Wlodarski R, Rezania K, Soliven B. Myasthenia Gravis: Epidemiology, Pathophysiology and Clinical Manifestations. Journal of Clinical Medicine 2021, Vol 10, Page 2235. 2021 May 21;10(11):2235. doi:10.3390/JCM10112235 PubMed PMID: 34064035.

8. Jaretzki A, Barohn RJ, Ernstoff RM, Kaminski HJ, Keesey JC, Penn AS, et al. Myasthenia gravis: Recommendations for clinical research standards. Neurology. 2000 Jul 12;55(1):16–23. doi:10.1212/WNL.55.1.16, PubMed PMID: 10891897.

9. Lucchi M, Ricciardi R, Melfi F, Duranti L, Basolo F, Palmiero G, et al. Association of thymoma and myasthenia gravis: oncological and neurological results of the surgical treatment. European Journal of Cardio-Thoracic Surgery. 2009 May 1;35(5):812–6. doi:10.1016/J.EJCTS.2009.01.014 PubMed PMID: 19237289.

10. Sanders DB, Wolfe GI, Benatar M, Evoli A, Gilhus NE, Illa I, et al. International consensus guidance for management of myasthenia gravis: Executive summary. Neurology. 2016 Jul 26;87(4):419–25. doi:10.1212/WNL.0000000000002790 PubMed PMID: 27358333.

11. Sheikh S, Alvi U, Soliven B, Rezania K. Drugs That Induce or Cause Deterioration of Myasthenia Gravis: An Update. J Clin Med. 2021 Apr 1;10(7):1537. doi:10.3390/JCM10071537 PubMed PMID: 33917535.

12. Wu N, Tüzün E, Cheng Y, Yan L, Wu Y, Rao J, et al. Central Role of T Follicular Helper Cells in Myasthenia Gravis. Archives of Neuropsychiatry. 2021;58(1):68. doi:10.29399/NPA.27193 PubMed PMID: 33795956.

13. Yi JS, Guptill JT, Stathopoulos P, Nowak RJ, O'Connor KC. B cells in the pathophysiology of myasthenia gravis. Muscle Nerve. 2018 Feb 1;57(2):172–84. doi:10.1002/MUS.25973 PubMed PMID: 28940642.

14. Bubuioc AM, Kudebayeva A, Turuspekova S, Lisnic V, Leone MA. The epidemiology of myasthenia gravis. J Med Life. 2021;14(1):7. doi:10.25122/JML-2020-0145 PubMed PMID: 33767779.

15. Lazaridis K, Tzartos SJ. Myasthenia Gravis: Autoantibody Specificities and Their Role in MG Management. Front Neurol. 2020 Nov 30;11:596981. doi:10.3389/FNEUR.2020.596981/XML/NLM PubMed PMID: 33329350.

16. Mantegazza R, Vanoli F, Frangiamore R, Cavalcante P. Complement Inhibition for the Treatment of Myasthenia Gravis [Internet]. 2020. doi:10.2147/ITT.S261414

17. San PP, Jacob S. Role of complement in myasthenia gravis. Front Neurol. 2023 Oct 5;14:1277596. doi:10.3389/FNEUR.2023.1277596/BIBTEX

18. Vakrakou AG, Karachaliou E, Chroni E, Zouvelou V, Tzanetakos D, Salakou S, et al. Immunotherapies in MuSK-positive Myasthenia Gravis; an IgG4 antibody-mediated disease. Front Immunol. 2023;14:1212757. doi:10.3389/FIMMU.2023.1212757 PubMed PMID: 37564637.

19. Masi G, O'Connor KC. Novel pathophysiological insights in autoimmune myasthenia gravis. Curr Opin Neurol. 2022 Oct 1;35(5):586. doi:10.1097/WCO.0000000000001088 PubMed PMID: 35942663.

20. Lazaridis K, Tzartos SJ. Autoantibody Specificities in Myasthenia Gravis; Implications for Improved Diagnostics and Therapeutics. Front Immunol. 2020 Feb 14;11:511152. doi:10.3389/FIMMU.2020.00212/XML PubMed PMID: 32117321.

21. Koneczny I, Herbst R. Myasthenia Gravis: Pathogenic Effects of Autoantibodies on Neuromuscular Architecture. Cells 2019, Vol 8, Page 671. 2019 Jul 2;8(7):671. doi:10.3390/CELLS8070671

22. Masi G, Li Y, Karatz T, Pham MC, Oxendine SR, Nowak RJ, et al. The clinical need for clustered AChR cell-based assay testing of seronegative MG. J

Neuroimmunol. 2022 Jun 15;367:577850. doi:10.1016/J.JNEUROIM.2022.577850 PubMed PMID: 35366559.

23. Spagni G, Gastaldi M, Businaro P, Chemkhi Z, Carrozza C, Mascagna G, et al. Comparison of Fixed and Live Cell-Based Assay for the Detection of AChR and MuSK Antibodies in Myasthenia Gravis. Neurol Neuroimmunol Neuroinflamm. 2023 Jan 21;10(1):e200038. doi:doi.org/10.1212/NXI.0000000000020003 PubMed PMID: 36270951.

24. Howard JF. Myasthenia gravis: the role of complement at the neuromuscular junction. Ann N Y Acad Sci. 2018 Jan 1;1412(1):113–28. doi:10.1111/NYAS.13522;PAGEGROUP:STRING:PUBLICATION PubMed PMID: 29266249.

25. Barnum SR, Bubeck D, Schein TN. Soluble Membrane Attack Complex: Biochemistry and Immunobiology. Front Immunol. 2020 Nov 10;11:585108. doi:10.3389/FIMMU.2020.585108/XML PubMed PMID: 33240274.

26. Huang YF, Sandholm K, Persson B, Nilsson B, Punga AR. Visualization and characterization of complement activation in acetylcholine receptor antibody seropositive myasthenia gravis. Muscle Nerve. 2024 Oct 1;70(4):851–61. doi:10.1002/mus.28227 PubMed PMID: 39115039.

27. Albazli K, Kaminski HJ, Howard JF. Complement Inhibitor Therapy for Myasthenia Gravis. Front Immunol. 2020 Jun 3;11:522416. doi:10.3389/FIMMU.2020.00917/BIBTEX PubMed PMID: 32582144.

28. Menny A, Lukassen M V., Couves EC, Franc V, Heck AJR, Bubeck D. Structural basis of soluble membrane attack complex packaging for clearance. Nat Commun. 2021 Dec 1;12(1):1–11. doi:10.1038/S41467-021-26366-W;TECHMETA PubMed PMID: 34667172.

29. Mollnes TE, Tschopp J. A unique epitope exposed in native complement component C9 and hidden in the terminal SC5b-9 complex enables selective detection and quantification of non-activated C9. J Immunol Methods. 1987;100(1):215–21. doi:https://doi.org/10.1016/0022-1759(87)90192-X

30. Takamori M. Structure and function of neuromuscular junction, centered on muscle-specific tyrosine kinase and related proteins. Clin Exp Neuroimmunol. 2016 Aug 1;7(3):215–25. doi:10.1111/CEN3.12314

31. Phillips WD, Vincent A. Pathogenesis of myasthenia gravis: update on disease types, models, and mechanisms. F1000Research 2016 5:1513. 2016 Jun 27;5:1513. doi:10.12688/f1000research.8206.1

32. Plomp JJ, Huijbers MGM, Verschuuren JJGM. Neuromuscular synapse electrophysiology in myasthenia gravis animal models. Ann N Y Acad Sci. 2018 Jan 1;1412(1):146–53. doi:10.1111/NYAS.13507 PubMed PMID: 29068559.

33. Diogenes L, Dellavance A, Baldo DC, Gozzi-Silva SC, Gomes K, Prado MS, et al. Detection of Autoantibodies Against the Acetylcholine Receptor, Evaluation

of Commercially Available Methodologies: Fixed Cell-Based Assay, Radioimmunoprecipitation Assay and Enzyme-Linked Immunosorbent Assay. J Neuromuscul Dis. 2024 Apr 30;11(3):613–23. doi:10.3233/JND-230210 PubMed PMID: 38578899.

34. Bu F, Zhang Y, Thomas C, Smith RJH. Soluble C5b-9 as a biomarker for complement activation in atypical hemolytic uremic syndrome. American Journal of Kidney Diseases. 2015 Jun 1;65(6):968–9. doi:10.1053/j.ajkd.2015.02.326 PubMed PMID: 25818678.

35. Evoli A, Palace J, Spagni G, Cheli M, Ruiter A, Verschuuren J, et al. Seronegative myasthenia gravis: An update paradigm for diagnosis and management. Neuromuscular Disorders. 2024 Nov 1;44:104468. doi:10.1016/J.NMD.2024.104468 PubMed PMID: 39427494.

36. Falso S, Marini S, Carrozza C, Sabatelli E, Mascagna G, Marini M, et al. Concordance between radioimmunoassay and fixed cell-based assay in subjects without myasthenia gravis: optimizing the diagnostic approach. Eur J Neurol. 2024 Dec 1;31(12). doi:10.1111/ENE.16435, PubMed PMID: 39118440.

37. Myasthenia Gravis - BC Neuroimmunology [Internet]. [cited 2025 Sep 1]. Available from: https://bcneuro.ca/tests/myasthenia_gravis/

38. Sahu S, Côté K, Lachize Neanne L, Badie A, Mathieu H, Leenhardt D, et al. Unraveling the Lectin Complement Pathway Dynamics in Childhood IgAN: SA-OR065. Journal of the American Society of Nephrology [Internet]. 2025;36(10S). Available from: https://journals.lww.com/jasn/fulltext/2025/10001/unraveling_the_lectin_complement_pathway_dynamics.227.aspx

39. Chen T, Liu Y, Liu Y, Hu N, Dai Y, Zhu C, et al. Clinical Value of Complement C3a, C5a, and sC5b-9 in Evaluating the Severity of Patients with Severe Fever with Thrombocytopenia Syndrome. J Inflamm Res. 2025;9001–14.

40. Soler M, Huertas CS, Lechuga LM. Label-free plasmonic biosensors for point-of-care diagnostics: a review. Expert Rev Mol Diagn. 2019 Jan 2;19(1):71–81. doi:10.1080/14737159.2019.1554435 PubMed PMID: 30513011.

41. Soler M, Lechuga LM. Biochemistry strategies for label-free optical sensor biofunctionalization: advances towards real applicability. Anal Bioanal Chem. 2022 Jul 1;414(18):5071–85. doi:10.1007/S00216-021-03751-4 PubMed PMID: 34735605.

42. Hoffmann S, Harms L, Schuelke M, Rückert JC, Goebel HH, Stenzel W, et al. Complement deposition at the neuromuscular junction in seronegative myasthenia gravis. Acta Neuropathol. 2020 Jun 1;139(6):1119–22. doi:10.1007/S00401-020-02147-5/FIGURES/1 PubMed PMID: 32157386.

43. Fichtner ML, Hoarty MD, Vadysirisack DD, Munro-Sheldon B, Nowak RJ, O'Connor KC. Myasthenia gravis complement activity is independent of

autoantibody titer and disease severity. PLoS One. 2022 Mar 1;17(3):e0264489. doi:10.1371/JOURNAL.PONE.0264489 PubMed PMID: 35290370.

44. Preston DC, Shapiro BE. Repetitive Nerve Stimulation. Electromyography and Neuromuscular Disorders. 2023 Jul 15;52–61. doi:10.1016/b978-1-4557-2672-1.00006-4 PubMed PMID: 37603640.

45. Giannoccaro MP, Paolucci M, Zenesini C, Di Stasi V, Donadio V, Avoni P, et al. Comparison of ice pack test and single-fiber EMG diagnostic accuracy in patients referred for myasthenic ptosis. Neurology. 2020 Sep 29;95(13):E1800–6. doi:10.1212/WNL.0000000000010619, PubMed PMID: 32788239.

46. Yoganathan K, Stevenson A, Tahir A, Sadler R, Radunovic A, Malek N. Bedside and laboratory diagnostic testing in myasthenia. J Neurol. 2022 Jun 1;269(6):3372. doi:10.1007/S00415-022-10986-3 PubMed PMID: 35142871.

47. Iacomino N, Vanoli F, Frangiamore R, Ballardini M, Scandiffio L, Bortone F, et al. Complement Activation Profile in Myasthenia Gravis Patients: Perspectives for Tailoring Anti-Complement Therapy. Biomedicines. 2022 Jun 1;10(6):1360. doi:10.3390/BIOMEDICINES10061360/S1

48. Ramesh M, Janani R, Deepa C, Rajeshkumar L. Nanotechnology-Enabled Biosensors: A Review of Fundamentals, Design Principles, Materials, and Applications. Biosensors 2023, Vol 13, Page 40. 2022 Dec 27;13(1):40. doi:10.3390/BIOS13010040 PubMed PMID: 36671875.

49. Bhalla N, Jolly P, Formisano N, Estrela P. Introduction to biosensors. Essays Biochem. 2016 Jun 30;60(1):1. doi:10.1042/EBC20150001 PubMed PMID: 27365030.

50. Morales MA, Halpern JM. Guide to Selecting a Biorecognition Element for Biosensors. Bioconjug Chem. 2018 Oct 17;29(10):3231. doi:10.1021/ACS.BIOCONJCHEM.8B00592 PubMed PMID: 30216055.

51. Qin J, Wang W, Gao L, Yao SQ. Emerging biosensing and transducing techniques for potential applications in point-of-care diagnostics. 2022. doi:10.1039/d1sc06269g

52. Bazin I, Tria SA, Hayat A, Marty JL. New biorecognition molecules in biosensors for the detection of toxins. Biosens Bioelectron. 2017 Jan 15;87:285–98. doi:10.1016/j.bios.2016.06.083 PubMed PMID: 27568847.

53. Leech D. Affinity biosensors. Chem Soc Rev. 1994 Jan 1;23(3):205–13. doi:10.1039/CS9942300205

54. Zhang L, Guo W, Lv C, Liu X, Yang M, Guo M, et al. Electrochemical biosensors represent promising detection tools in medical field. Advanced Sensor and Energy Materials. 2023 Dec 1;2(4):100081. doi:10.1016/J.ASEMS.2023.100081

55. Arlett JL, Myers EB, Roukes ML. Comparative advantages of mechanical biosensors. Nat Nanotechnol. 2011;6(4):203–15. doi:10.1038/NNANO.2011.44, PubMed PMID: 21441911.

56. Akgönüllü S, Denizli A. Recent advances in optical biosensing approaches for biomarkers detection. Biosens Bioelectron X. 2022 Dec 1;12:100269. doi:10.1016/J.BIOSX.2022.100269

57. Huertas CS, Calvo-Lozano O, Mitchell A, Lechuga LM. Advanced Evanescent-Wave Optical Biosensors for the Detection of Nucleic Acids: An Analytic Perspective. Front Chem. 2019 Oct 25;7. doi:10.3389/FCHEM.2019.00724/PDF

58. Wang H, Wang T, Yuan X, Wang Y, Yue X, Wang L, et al. Plasmonic Nanostructure Biosensors: A Review. Sensors 2023, Vol 23, Page 8156. 2023 Sep 28;23(19):8156. doi:10.3390/S23198156 PubMed PMID: 37836985.

59. Islam MA, Masson JFO. Plasmonic Biosensors for Health Monitoring: Inflammation Biomarker Detection [Internet]. Vol. 10. 2025;10:601. doi:10.1021/acssensors.4c03562

60. Ramirez-Priego P, Mauriz E, Giarola JF, Lechuga LM. Overcoming challenges in plasmonic biosensors deployment for clinical and biomedical applications: A systematic review and meta-analysis. Sens Biosensing Res. 2024 Dec 1;46:100717. doi:10.1016/J.SBSR.2024.100717

61. Ramirez Priego. Low-cost point-of-care biosensor device for clinical diagnosis in developing countries. 2021.

62. Nanda BP, Rani P, Paul P, Aman, Subrahmanya S G, Bhatia R. Recent trends and impact of localized surface plasmon resonance (LSPR) and surface-enhanced Raman spectroscopy (SERS) in modern analysis. J Pharm Anal. 2024 Nov 1;14(11):100959. doi:10.1016/J.JPHA.2024.02.013

63. Homola J, Piliarik M. Surface Plasmon Resonance (SPR) Sensors [Internet]. 2006;45–67. doi:10.1007/5346_014

64. Armbruster DA, Pry T. Limit of Blank, Limit of Detection and Limit of Quantitation. Clin Biochem Rev. 2008 Aug;29(Suppl 1):S49. PubMed PMID: 18852857.

65. Little T. Method Validation Essentials, Limit of Blank, Limit of Detection, and Limit of Quantitation [Internet]. Vol. 28. MJH Life Sciences; 2015 [cited 2025 Aug 15]. Available from: https://www.biopharminternational.com/view/method-validation-essentials-limit-blank-limit-detection-and-limit-quantitation

66. López-Muñoz GA, Estevez MC, Peláez-Gutierrez EC, Homs-Corbera A, García-Hernandez MC, Imbaud JI, et al. A label-free nanostructured plasmonic biosensor based on Blu-ray discs with integrated microfluidics for sensitive biodetection. Biosens Bioelectron. 2017 Oct 15;96:260–7. doi:10.1016/j.bios.2017.05.020 PubMed PMID: 28501746.

67. Hu C, Liu D. High-performance Grating Coupled Surface Plasmon Resonance Sensor Based on Al-Au Bimetallic Layer [Internet]. [cited 2025 Sep 1]. Available from: www.ccsenet.org/mas

68. Nair S, Escobedo C, Sabat RG. Crossed Surface Relief Gratings as Nanoplasmonic Biosensors. ACS Sens. 2017 Mar 24;2(3):379–85. doi:10.1021/ACSSENSORS.6B00696/ PubMed PMID: 28723204.

69. Kumari S, Mohapatra S, Moirangthem RS. Development of flexible plasmonic plastic sensor using nanograting textured laminating film. Mater Res Express. 2017 Feb 14;4(2):025008. doi:10.1088/2053-1591/AA5B5E

70. Long S, Cao J, Wang Y, Gao S, Xu N, Gao J, et al. Grating coupled SPR sensors using off the shelf compact discs and sensitivity dependence on grating period. Sensors and Actuators Reports. 2020 Nov 1;2(1):100016. doi:10.1016/J.SNR.2020.100016

71. Hill RT. Plasmonic biosensors. Wiley Interdiscip Rev Nanomed Nanobiotechnol. 2015 Mar 1;7(2):152–68. doi:10.1002/WNAN.1314 PubMed PMID: 25377594.

72. Soler M, Lechuga LM. Principles, technologies, and applications of plasmonic biosensors. J Appl Phys. 2021 Mar 21;129(11). doi:10.1063/5.0042811/1025364

73. Topor CV, Puiu M, Bala C. Strategies for Surface Design in Surface Plasmon Resonance (SPR) Sensing. Biosensors 2023, Vol 13, Page 465. 2023 Apr 7;13(4):465. doi:10.3390/BIOS13040465 PubMed PMID: 37185540.

74. Butt MA. Surface Plasmon Resonance-Based Biodetection Systems: Principles, Progress and Applications—A Comprehensive Review. Biosensors 2025, Vol 15, Page 35. 2025 Jan 9;15(1):35. doi:10.3390/BIOS15010035

75. Duan Q, Liu Y, Chang S, Chen H, Chen JH. Surface Plasmonic Sensors: Sensing Mechanism and Recent Applications. Sensors 2021, Vol 21, Page 5262. 2021 Aug 4;21(16):5262. doi:10.3390/S21165262 PubMed PMID: 34450704.

76. Homola J. Present and future of surface plasmon resonance biosensors. Anal Bioanal Chem. 2003 Oct;377(3):528–39. doi:10.1007/S00216-003-2101-0, PubMed PMID: 12879189.

77. Piliarik M, Vaisocherová H, Homola J. Surface plasmon resonance biosensing. Methods Mol Biol. 2009;503:65–88. doi:10.1007/978-1-60327-567-5_5 PubMed PMID: 19151937.

78. Aftab M, Mansha MS, Iqbal T, Farooq M. Surface Plasmon Excitation: Theory, Configurations, and Applications. Plasmonics. 2024 Aug 1;19(4):1701–19. doi:10.1007/S11468-023-02095-2/

79. Suárez I, Ferrando A, Marques-Hueso J, DIéz A, Abargues R, Rodríguez-Cantó PJ, et al. Propagation length enhancement of surface plasmon polaritons in gold nano-/micro-waveguides by the interference with photonic modes in the surrounding active dielectrics. Nanophotonics. 2017 Aug 28;6(5):1109–20. doi:10.1515/NANOPH-2016-0166/

80. Kashyap R, Nemova G. Surface Plasmon Resonance-Based Fiber and Planar Waveguide Sensors. J Sens. 2009 Jan 1;2009(1):645162. doi:10.1155/2009/645162

81. Homola J. Surface plasmon resonance sensors for detection of chemical and biological species. Chem Rev. 2008 Feb;108(2):462–93. doi:10.1021/CR068107D/ASSET/IMAGES/LARGE/CR068107DF00008.JPEG PubMed PMID: 18229953.

82. Long GL, Winefordner JD. Limit of Detection: A Closer Look at the IUPAC Definition. Anal Chem. 1983;55(7):712A-724A. doi:10.1021/AC00258A001

83. Rossi S, Gazzola E, Capaldo P, Borile G, Romanato F. Grating-Coupled Surface Plasmon Resonance (GC-SPR) Optimization for Phase-Interrogation Biosensing in a Microfluidic Chamber. Sensors 2018, Vol 18, Page 1621. 2018 May 18;18(5):1621. doi:10.3390/S18051621 PubMed PMID: 29783711.

84. Willets KA, Van Duyne RP. Localized surface plasmon resonance spectroscopy and sensing. Annu Rev Phys Chem. 2007 May 5;58(Volume 58, 2007):267–97. doi:10.1146/ANNUREV.PHYSCHEM.58.032806.104607/1 PubMed PMID: 17067281.

85. Osaki T, Takeuchi S. Artificial Cell Membrane Systems for Biosensing Applications. Anal Chem. 2017 Jan 3;89(1):216–31. doi:10.1021/ACS.ANALCHEM.6B04744/ PubMed PMID: 27959515.

86. Lim SA, Ahmed MU. Introduction to Immunosensors. RSC Detection Science. 2019;2019-January(14):1–20. doi:10.1039/9781788016162-00001

87. Hu WG, Nagata LP. Human Vaccines Antibody gene-based prophylaxis and therapy for biodefence [Internet]. 2008. doi:10.4161/hv.4.1.4778

88. Aziz M, Iheanacho F, Hashmi MF. Physiology, Antibody. StatPearls. 2023 May 1. PubMed PMID: 31536276.

89. Hirsh SL, Bilek MMM, Nosworthy NJ, Kondyurin A, Dos Remedios CG, McKenzie DR. A Comparison of covalent immobilization and physical adsorption of a cellulase enzyme mixture. Langmuir. 2010 Sep 7;26(17):14380–8. doi:10.1021/LA1019845/ PubMed PMID: 20704318.

90. Lee JM, Park HK, Jung Y, Kim JK, Jung SO, Chung BH. Direct Immobilization of Protein G Variants with Various Numbers of Cysteine Residues on a Gold Surface [Internet]. 2007. doi:10.1021/ac0619231

91. Verbatim [Internet]. [cited 2025 Sep 8]. Blu-ray Technology. Available from: https://www.bigpockets.co.uk/site/pdf/CC-50704.pdf

92. Guner H, Ozgur E, Kokturk G, Celik M, Esen E, Topal AE, et al. A smartphone based surface plasmon resonance imaging (SPRi) platform for on-site biodetection. Sens Actuators B Chem. 2017;239:571–7. doi:10.1016/j.snb.2016.08.061

93. Chen C, Singh R, Huo S, Song Y, Wang K, Chiavaioli F, et al. Evanescent wave-based optical biosensors for innovations, medical application and future perspectives. J Adv Res. 2025 Jul 7. doi:10.1016/J.JARE.2025.07.007

94. Slabý J, Homola J. Performance of label-free optical biosensors: What is figure of merit (not) telling us? Biosens Bioelectron. 2022 Sep 15;212:114426. doi:10.1016/J.BIOS.2022.114426 PubMed PMID: 35671697.

95. Chaki NK, Vijayamohanan K. Self-assembled monolayers as a tunable platform for biosensor applications. Biosens Bioelectron. 2002 Jan 1;17(1–2):1–12. doi:10.1016/S0956-5663(01)00277-9 PubMed PMID: 11742729.

96. Wadu-Mesthrige K, Amro NA, Liu GY. Immobilization of proteins on self-assembled monolayers. Scanning. 2000 Nov 1;22(6):380–8. doi:10.1002/SCA.4950220607;PAGE:STRING:ARTICLE/CHAPTER PubMed PMID: 11145264.

97. Sonato A, Ruffato G, Zacco G, Silvestri D, Natali M, Carli M, et al. Enhanced sensitivity azimuthally controlled grating-coupled surface plasmon resonance applied to the calibration of thiol-poly(ethylene oxide) grafting. Sens Actuators B Chem. 2013 May 1;181:559–66. doi:10.1016/J.SNB.2013.02.022

98. Young MB, Oh BK, Lee W, Won HL, Choi JW. Study on orientation of immunoglobulin G on protein G layer. Biosens Bioelectron. 2005 Jul 15;21(1):103–10. doi:10.1016/J.BIOS.2004.09.003 PubMed PMID: 15967357.

99. Ngo BKD, Grunlan MA. Protein Resistant Polymeric Biomaterials. ACS Macro Lett. 2017 Sep 19;6(9):992–1000. doi:10.1021/ACSMACROLETT.7B00448/ASSET/IMAGES/LARGE/MZ-2017-004485_0007.JPEG PubMed PMID: 35650885.

100. Tao S, Jia TW, Yang Y, Chu LQ. BSA-Sugar Conjugates as Ideal Building Blocks for SPR-Based Glycan Biosensors. ACS Sens. 2017 Jan 27;2(1):57–60. doi:doi/10.1021/acssensors.6b00679 PubMed PMID: 28722428.

101. GE Healthcare. Biacore™ Assay Handbook. 2015.

102. Mariani S, Minunni M. Surface plasmon resonance applications in clinical analysis. Anal Bioanal Chem. 2014 Apr 1;406(9):2303. doi:10.1007/S00216-014-7647-5 PubMed PMID: 24566759.

103. Masdor NA, Masdor A. Detection Limit of the Four-Parameter Logistic Model for the Quantitative Detection of Serum Squamous Cell Carcinoma Antigenin Cervical Cancer Based on Surface Plasmon Resonance Biosensor. Journal of Environmental Microbiology and Toxicology. 2021 Dec 31;9(2):30–2. doi:10.54987/JEMAT.V9I2.644

104. Lee KS, El-Sayed MA. Dependence of the enhanced optical scattering efficiency relative to that of absorption for gold metal nanorods on aspect ratio, size, end-cap shape, and medium refractive index. Journal of Physical Chemistry B. 2005 Nov 3;109(43):20331–8. doi:10.1021/JP054385P PubMed PMID: 16853630.

105. Byun I, Coleman AW, Kim B. Transfer of thin Au films to polydimethylsiloxane (PDMS) with reliable bonding using (3-mercaptopropyl)trimethoxysilane (MPTMS) as a molecular adhesive. Journal of Micromechanics and Microengineering. 2013 Aug;23(8). doi:10.1088/0960-1317/23/8/085016

106. Lim KS, Chang WJ, Koo YM, Bashir R. Reliable fabrication method of transferable micron scale metal pattern for poly(dimethylsiloxane) metallization. Lab Chip. 2006 Mar 29;6(4):578–80. doi:10.1039/B514755G PubMed PMID: 16572223.

107. Piliarik M, Homola J, Karlsson R, Fält A, Hastings JT, Guo J, et al. Surface plasmon resonance (SPR) sensors: approaching their limits? Optics Express, Vol 17, Issue 19, pp 16505-16517. 2009 Sep 14;17(19):16505–17. doi:10.1364/OE.17.016505 PubMed PMID: 19770865.

108. Escobedo C. On-chip nanohole array based sensing: a review. Lab Chip. 2013 Jun 4;13(13):2445–63. doi:10.1039/C3LC50107H

109. Lee SA, Link S. Chemical Interface Damping of Surface Plasmon Resonances. Acc Chem Res. 2021 Apr 20;54(8):1950–60. doi:10.1021/ACS.ACCOUNTS.0C00872/ PubMed PMID: 33788547.

110. Sepúlveda B, Angelomé PC, Lechuga LM, Liz-Marzán LM. LSPR-based nanobiosensors. Nano Today. 2009 Jun 1;4(3):244–51. doi:10.1016/J.NANTOD.2009.04.001

111. Jung LS, Campbell CT, Chinowsky TM, Mar MN, Yee SS. Quantitative Interpretation of the Response of Surface Plasmon Resonance Sensors to Adsorbed Films. 1998.

112. Velinov T, Ahtapodov L, Nelson A, Gateshki M, Bivolarska M. Influence of the surface roughness on the properties of Au films measured by surface plasmon resonance and X-ray reflectometry. Thin Solid Films. 2011 Jan 31;519(7):2093–7. doi:10.1016/J.TSF.2010.10.059

113. Mutalik C, Sharma S, Yougbaré S, Chen CY, Kuo TR. Nanoplasmonic Biosensors: A Comprehensive Overview and Future Prospects. Int J Nanomedicine. 2025 May 7;20:5817–36. doi:10.2147/IJN.S521442 PubMed PMID: 40356858.

114. Ahmed R, Ozen MO, Inci F, Karaaslan MG, Henrich TJ, Demirci U. Real-time biosensing of proteins on a DVD nanoplasmonic grating. https://doi.org/101117/122508624. 2019 Mar 7;10894:81–6. doi:10.1117/12.2508624

115. Pierson-Perry JF, Vaks JE, Durham AP, Fischer C, Gutenbrunner C, Hillyard D, et al. Evaluation of Detection Capability for Clinical Laboratory Measurement Procedures; Approved Guideline-Second Edition [Internet]. Vol. 24. CLSI; 2012 [cited 2025 Aug 14]. Available from: www.clsi.org.

116. Laffont E, Crespo-Monteiro N, Valour A, Berini P, Jourlin Y. Differential Sensing with Replicated Plasmonic Gratings Interrogated in the Optical Switch Configuration. Sensors 2023, Vol 23, Page 1188. 2023 Jan 20;23(3):1188. doi:10.3390/S23031188 PubMed PMID: 36772228.

117. Chakraborty K, Kumawat N, Sultana S, Varma MM. Enhancing the quality factor of grating coupled plasmon resonance in optical recording media. Sens Actuators A Phys. 2016 Jun 15;244:50–5. doi:10.1016/j.sna.2016.04.025

118. Oliverio M, Perotto S, Messina GC, Lovato L, De Angelis F. Chemical Functionalization of Plasmonic Surface Biosensors: A Tutorial Review on Issues, Strategies, and Costs. ACS Appl Mater Interfaces. 2017 Sep 6;9(35):29394–411. doi:10.1021/ACSAMI.7B01583/ASSET/IMAGES/LARGE/AM-2017-01583F_0005.JPEG PubMed PMID: 28796479.

119. Welch NG, Scoble JA, Muir BW, Pigram PJ. Orientation and characterization of immobilized antibodies for improved immunoassays (Review). Biointerphases. 2017 Jun 1;12(2):2–301. doi:10.1116/1.4978435/237594 PubMed PMID: 28301944.

120. Shen M, Rusling JF, Dixit CK. Site-Selective Orientated Immobilization of Antibodies and Conjugates for Immunodiagnostics Development. Methods. 2016 Mar 1;116:95. doi:10.1016/J.YMETH.2016.11.010 PubMed PMID: 27876681.

121. Kim H, Kang DY, Goh HJ, Oh BK, Singh RP, Oh SM, et al. Analysis of direct immobilized recombinant protein G on a gold surface. Ultramicroscopy. 2008 Sep 1;108(10):1152–6. doi:10.1016/J.ULTRAMIC.2008.04.049 PubMed PMID: 18565661.

122. Nicoya Lifesciences Inc. How Preconcentration can save your Protein Samples in SPR Experiments | Nicoya [Internet]. [cited 2025 Aug 7]. Available from: https://nicoyalife.com/blog/spr-tips/save-protein-samples-preconcentration-surface-plasmon-resonance/

123. Masson JF, Battaglia TM, Khairallah P, Beaudoin S, Booksh KS. Quantitative measurement of cardiac markers in undiluted serum. Anal Chem. 2007 Jan 15;79(2):612–9. doi:10.1021/AC061089F/ASSET/IMAGES/LARGE/AC061089FF00006.JPEG PubMed PMID: 17222027.

124. Hall TG, Smukste I, Bresciano KR, Wang Y, McKearn D, Savage RE, et al. Identifying and Overcoming Matrix Effects in Drug Discovery and Development. Tandem Mass Spectrometry - Applications and Principles. 2012 Feb 29. doi:10.5772/32108

125. Luan J, Xu T, Cashin J, Morrissey JJ, Kharasch ED, Singamaneni S. Environmental Stability of Plasmonic Biosensors Based on Natural versus Artificial Antibody. Anal Chem. 2018 Jul 3;90(13):7880–7. doi:10.1021/ACS.ANALCHEM.7B05470/ASSET/IMAGES/LARGE/AC-2017-05470A_0005.JPEG PubMed PMID: 29790737.

126. Gao S, Guisán JM, Rocha-Martin J. Oriented immobilization of antibodies onto sensing platforms - A critical review. Anal Chim Acta. 2022 Jan 2;1189:338907. doi:10.1016/J.ACA.2021.338907 PubMed PMID: 34815045.

127. Park J, Kim M. Strategies in Protein Immobilization on a Gold Surface. Applied Science and Convergence Technology. 2015 Jan 30;24(1):1–8. doi:10.5757/ASCT.2015.24.1.1

128. Zhu H, Lin M, Li Y, Duan K, Hu J, Chen C, et al. LSPR sensing for in situ monitoring the Ag dissolution of Au@Ag core-shell nanoparticles in biological environments. Spectrochim Acta A Mol Biomol Spectrosc. 2024 Apr 5;310:123885. doi:10.1016/J.SAA.2024.123885 PubMed PMID: 38245969.

129. Zäh M, Brandenbusch C, Groël S, Winter G, Sadowski G. Water Activity as an Indicator for Antibody Storage Stability in Lyophilized Formulations. Mol Pharm. 2025 Feb 3;22(2):918–26. doi:10.1021/ACS.MOLPHARMACEUT.4C01106/SUPPL_FILE/MP4C01106_SI_001.PDF PubMed PMID: 39809457.

130. Downey JD, Crean AM, Ryan KB. Impact of protein adsorption during biopharmaceutical manufacture & storage. European Journal of Pharmaceutical Sciences. 2025 Jun 1;209:107071. doi:10.1016/J.EJPS.2025.107071 PubMed PMID: 40097023.

131. Zhang J, Wang Y, Wong TI, Liu X, Zhou X, Liedberg B. Electrofocusing-enhanced localized surface plasmon resonance biosensors. Nanoscale. 2015 Oct 15;7(41):17244–8. doi:10.1039/C5NR03373J PubMed PMID: 26370057.

132. Barbosa AI, Edwards AD, Reis NM. Antibody Surface Coverage Drives Matrix Interference in Microfluidic Capillary Immunoassays. ACS Sens. 2021 Jul 23;6(7):2682–90. doi:10.1021/ACSSENSORS.1C00704 PubMed PMID: 34138534.

133. Mrksich M. Using self-assembled monolayers to model the extracellular matrix. Acta Biomater. 2009;5(3):832. doi:10.1016/J.ACTBIO.2009.01.016 PubMed PMID: 19249721.

134. Primer KL. Adsorption of Proteins Oligo(ethylene oxide): Monolayers onto Surfaces Containing End-Attached A Model System Using Self-Assembled. 1993;715.

135. He M, Gao K, Zhou L, Jiao Z, Wu M, Cao J, et al. Zwitterionic materials for antifouling membrane surface construction. Acta Biomater. 2016 Aug 1;40:142–52. doi:10.1016/J.ACTBIO.2016.03.038 PubMed PMID: 27025359.

136. Lau SK, Yong WF. Recent Progress of Zwitterionic Materials as Antifouling Membranes for Ultrafiltration, Nanofiltration, and Reverse Osmosis. ACS Appl Polym Mater. 2021 Sep 10;3(9):4390–412. doi:10.1021/ACSAPM.1C00779

137. Zhang Y, Ma M, Aisa HA, Chen L. Oriented Immobilization of IgG for Immunosensor Development. Chemosensors 2025, Vol 13, Page 50. 2025 Feb 3;13(2):50. doi:10.3390/CHEMOSENSORS13020050

138. Hao N, Zhang Y, Zhong H, Zhou Z, Hua R, Qian J, et al. Design of a Dual Channel Self-Reference Photoelectrochemical Biosensor. Anal Chem. 2017 Oct 3;89(19):10133–6. doi:10.1021/acs.analchem.7b03132

139. Findlay JWA, Dillard RF. Appropriate calibration curve fitting in ligand binding assays. AAPS Journal. 2007 Jun 29;9(2):E260–7. doi:10.1208/AAPSJ0902029/METRICS PubMed PMID: 17907767.

140. Hugo F, Krämer S, Bhakdi S. Sensitive ELISA for quantitating the terminal membrane C5b-9 and fluid-phase SC5b-9 complex of human complement. J Immunol Methods. 1987 May 20;99(2):243–51. doi:https://doi.org/10.1016/0022-1759(87)90134-7

141. Frykman H, Gibbs E, Ismael S. Surface Plasmon Resonance Imaging (SPRi)-based Immunobiosensor for the Detection and Comprehensive Analysis of Acetylcholine Receptor (AChR) Antibodies in Myathenia Gravis. Neurology. 2024 Oct 8;103(7_Supplement_1):S141–2. doi:10.1212/01.WNL.0001051996.48467.F5

142. Gibbs E, Aziz T, Frykman H. Validation of a Surface Plasmon Resonance Assay for the Diagnostic Detection and Characterization of Muscle-specific Kinase (MuSK) Antibodies in Myasthenia Gravis (MG) Patients (4753). Neurology. 2020 Apr 14;94(15_supplement):4753. doi:10.1212/WNL.94.15_SUPPLEMENT.4753

143. Mauriz E. Low-Fouling Substrates for Plasmonic Sensing of Circulating Biomarkers in Biological Fluids. Biosensors (Basel). 2020 Jun 10;10(6):63. doi:10.3390/BIOS10060063 PubMed PMID: 32531908.

144. Howard JF, Utsugisawa K, Benatar M, Murai H, Barohn RJ, Illa I, et al. Safety and efficacy of eculizumab in anti-acetylcholine receptor antibody-positive refractory generalised myasthenia gravis (REGAIN): a phase 3, randomised, double-blind, placebo-controlled, multicentre study. Lancet Neurol. 2017 Dec 1;16(12):976–86. doi:10.1016/S1474-4422(17)30369-1, PubMed PMID: 29066163.

145. Hnasko R. ELISA: Methods and Protocols. ELISA: Methods and Protocols. 2015 Jan 1;1–216. doi:10.1007/978-1-4939-2742-5/COVER

146. Martinez Salazar A, Mokhtari S, Peguero E, Jaffer M. The Role of Complement in the Pathogenesis and Treatment of Myasthenia Gravis. Cells. 2025 May 1;14(10). doi:10.3390/CELLS14100739, PubMed PMID: 40422242.

147. Grebenchtchikov N, Sweep CGJ, Geurts-Moespot A, Piffanelli A, Foekens JA, Benraad TJ. An ELISA avoiding interference by heterophilic antibodies in the measurement of components of the plasminogen activation system in blood. J

Immunol Methods. 2002 Oct 15;268(2):219–31. doi:10.1016/S0022-1759(02)00213-2 PubMed PMID: 12215390.

148. Monnier VM, Fulpius BW. A radioimmunoassay for the quantitative evaluation of anti-human acetylcholine receptor antibodies in myasthenia gravis. Clin Exp Immunol. 1977 Jul;29(1):16. PubMed PMID: 891031.

149. Mariscal A, Martínez C, Goethals L, Cortés-Vicente E, Moltó E, Juárez C, et al. Modified radioimmunoassay versus ELISA to quantify anti-acetylcholine receptor antibodies in a mouse model of myasthenia gravis. J Immunol Methods. 2024 Nov 1;534:113748. doi:10.1016/J.JIM.2024.113748 PubMed PMID: 39241980.

150. Obaid AH, Zografou C, Vadysirisack DD, Munro-Sheldon B, Fichtner ML, Roy B, et al. Heterogeneity of Acetylcholine Receptor Autoantibody-Mediated Complement Activity in Patients With Myasthenia Gravis. Neurol Neuroimmunol Neuroinflamm. 2022 Jul 26;9(4):e1169. doi:doi.org/10.1212/NXI.0000000000001169 PubMed PMID: 35473886.